Structural basis of small-molecule inhibition of human multidrug transporter ABCG2

Author(s):
Jackson, Scott M.; Manolaridis, Ioannis; Kowal, Julia; Zechner, Melanie; Taylor, Nicholas M.I.; Bause, Manuel; Bauer, Stefanie; Bartholomaeus, Ruben; Bernhardt, Guenther; Koenig, Burkhard; Buschauer, Armin; Stahlberg, Henning; Altmann, Karl-Heinz; Locher, Kaspar P.

Publication date:
2018-04

Permanent link:
https://doi.org/10.3929/ethz-b-000256191

Originally published in:
Nature Structural & Molecular Biology 25, https://doi.org/10.1038/s41594-018-0049-1

Structural basis of small-molecule inhibition of human multidrug transporter ABCG2

Scott M Jackson[1*], Ioannis Manolaridis[1*], Julia Kowal[1*], Melanie Zechner[2*], Nicholas MI Taylor[3*†], Manuel Bause[4], Stefanie Bauer[4], Ruben Bartholomaeus[2], Guenther Bernhardt[4], Burkhard Koenig[4], Armin Buschauer[4‡], Henning Stahlberg[3], Karl-Heinz Altmann[2#], Kaspar P Locher[1#]

[1]Institute of Molecular Biology and Biophysics, Department of Biology, ETH Zurich, Switzerland.

[2]Institute of Pharmaceutical Sciences, Department of Chemistry and Applied Biosciences, ETH Zurich, Switzerland.

[3]Center for Cellular Imaging and NanoAnalytics (C-CINA), Biozentrum, University of Basel, Switzerland.

[4]Faculty of Chemistry and Pharmacy, University of Regensburg, Germany.

[†]Present address: Novo Nordisk Foundation Center for Protein Research, Faculty of Health and Medical Sciences, University of Copenhagen, Denmark.

[‡]Deceased July 18, 2017.

*These authors contributed equally to this work.

[#]Correspondence should be addressed to K.P.L (locher@mol.biol.ethz.ch) or K-H A (karl-heinz.altmann@pharma.ethz.ch).

ABCG2 is an ATP-binding cassette transporter that protects tissues against xenobiotics, affects the pharmacokinetics of drugs, and contributes to multidrug resistance. Although many inhibitors and modulators of ABCG2 were developed, understanding their structure-activity relationship requires high-resolution structural insight. Here we present cryo-EM structures of human ABCG2 bound to synthetic derivatives of the fumitremorgin C-related inhibitor Ko143 or the multidrug resistance modulator tariquidar. Both compounds are bound to the central, inward-facing cavity of ABCG2, blocking access for substrates and preventing conformational changes required for ATP hydrolysis. The high resolutions allowed for *de novo* building of the entire transporter and also revealed tightly bound phospholipids and cholesterol interacting with the lipid-exposed surface of the TMDs. Extensive chemical modifications of the Ko143 scaffold, combined with *in vitro* functional analyses, revealed the details of ABCG2 interactions with this compound family and provide a basis for the design of novel inhibitors and modulators.

ABCG2, also known as breast cancer resistance protein (BCRP), is a constitutively expressed ABC transporter with physiological roles in many tissues including the blood-brain and blood-testis barriers, the liver, the kidney and the mammary glands [1-4]. Dysfunction of ABCG2 is linked to hyperuricaemia, which can result in gout, kidney disease and hypertension, all of which are thought to be a consequence of the impaired transport of uric acid [5]. ABCG2, like its functional homologues ABCB1 (P-glycoprotein) and ABCC1 (MRP1), has a major protective role against xenobiotics. It affects the pharmacokinetics of many commonly used drugs, and its expression correlates with a poor prognosis and treatment outcome of certain cancers [6-10]. ABCG2 has a broad substrate specificity, with a certain preference for flat, polycyclic, hydrophobic compounds [11-15].

Because of their potential value as adjuvants in the treatment of cancer and pharmacotherapy, extensive efforts have been directed over the past decades to the development of specific inhibitors against human ABCG2 and other multidrug ABC transporters [1, 16-20]. The fungal toxin fumitremorgin C (FTC) is a selective inhibitor of ABCG2 but has undesirable neurotoxic effects [16, 21, 22]. To reduce neurotoxicity, synthetic, tetracyclic analogues of FTC were developed. Among them, Ko143 was found to be more potent and less toxic than FTC, but is not stable in mouse plasma and has been reported to have non-specific effects on the transport activities of ABCB1 and ABCC1 at concentrations above 1 μM [23]. Attempts have also been made to develop selective ABCG2 inhibitors derived from

tariquidar, a third-generation ABCB1 inhibitor reported to be a potential substrate of ABCG2 [20, 24-28].

There is at present no structure of a human multidrug transporter bound to specific inhibitors. All of the above approaches aimed at developing specific inhibitors were made in the absence of structural insight into how the small compounds may interact with, modulate, or inhibit ABCG2. Recently, the first structure of human ABCG2 revealed two cholesterol molecules bound at a central, inward-facing cavity, hinting at a potential location where substrates such as estrone-3-sulfate (E_1S) might bind [29]. However, it remained unknown where inhibitors bind ABCG2 and whether a single or multiple ligand binding sites exist, topics that are hotly debated [30-34]. To address these questions, we determined single-particle cryo-EM structures of nanodisc-reconstituted human ABCG2 bound to distinct inhibitors. The high resolution obtained not only allowed the first *de novo* building of an atomic structure of the entire human ABCG2 protein, but also provided detailed insight into inhibition of the transporter by small molecules. By synthesizing a range of Ko143-derived compounds and testing their activity *in vitro*, we also obtained crucial information into the structure-activity relationship (SAR) of the Ko143 scaffold. Finally, we demonstrate that depending on the size of the compounds, one or two inhibitor molecules are required for full inhibition of ABCG2. These results provide an essential structural basis for future development of ABCG2 modulators.

RESULTS

Synthesis of inhibitory compounds selective for ABCG2

Due to its high selectivity for ABCG2, we used Ko143 as a starting point for the synthesis of novel compounds (Fig. 1 and Supplementary Table 1). We mainly focused on modifications of the C-3 (R_1) and C-9 (R_2) positions of the Ko143 scaffold because previous studies demonstrated that the inhibitory capacities of FTC, and its derivatives, are affected by changes at these positions [16, 35]. Seventeen compounds were synthesized and screened *in vitro* for their ability to inhibit the E_1S-stimulated ATPase activity and initial E_1S transport activity of ABCG2 in proteoliposomes [29], and similar trends were observed in the ranking of their inhibitory capacities (Fig. 1a,b and Supplementary Table 2). We found that five compounds were as potent as Ko143 or slightly superior. Compound MZ29, which contained an O-cyclopentyl group added to the C-9 position, was found to be the most potent inhibitor of ATPase activity and fully abolished E_1S transport. In addition, similarly to Ko143, but unlike E_1S, it had a significant thermostabilizing

effect on ABCG2 (Supplementary Fig 1a,b and Supplementary Table 3), suggesting it caused conformational stabilization, and was therefore selected for structural studies.

For high-resolution structure determination by cryo-EM, we added the conformational antigen-binding fragment of the human-specific 5D3 antibody (Fab) to inhibitor-bound ABCG2 (Figs. 2, 3, 4 and Supplementary Figs. 2, 3, 4, 5, 6) [29, 36]. The addition of two Fabs increased the particle mass by ~100 kDa, which aided cryo-EM analysis, allowing for higher resolution reconstruction. To rule out that the Fab altered the conformation of ABCG2 and diminished the mechanistic insight, we also determined the structure of MZ29-bound ABCG2 in the absence of Fab, which was found to be indistinguishable to the Fab-bound structure (see below and Supplementary Figs. 7, 8). Furthermore, we investigated whether Fab would affect the binding of a synthetic, fluorescent Ko143 derivative (FKo143) to ABCG2. FKo143 contains a fluorescent NBD group at the C-3 position, which did not alter its inhibitory capacity (Fig. 1a,b,d), thus enabling us to measure its binding affinity by microscale thermophoresis (MST) (Fig. 1c and Supplementary Table 4). By determining dissociation constants, we found that the binding of FKo143 to ABCG2 was unaffected by Fab, providing strong support for the structural data and highlighting the functional relevance of the inhibitor-bound ABCG2-Fab structures.

Structures of the ABCG2-MZ29 complexes

The structure of nanodisc-reconstituted ABCG2 bound to MZ29 and two Fabs (ABCG2-MZ29-Fab) was determined at an overall resolution of 3.1 Å (Fig. 2, Table 1 and Supplementary Figs. 1, 2, 3, 4). The transmembrane domains (TMDs) and the ABCG2-Fab interface were very well resolved (resolution around 2.5 Å), allowing for the identification of two bound MZ29 molecules (Fig. 2a,b and Supplementary Figs. 3, 4). The density for the nucleotide-binding domains (NBDs), which previously had only been modeled due to lower resolution [29], was also of excellent quality (Supplementary Fig. 4), allowing *de novo* building and thus providing the first complete atomic structure of human ABCG2. The conformation of the TMDs in the ABCG2-MZ29-Fab structure was found to be inward-facing, similar to that of the previously determined ABCG2-cholesterol-Fab structure, with a slit-like cavity (cavity 1) accessible both from the cytoplasmic side of the membrane and from the inner leaflet of the lipid bilayer. Cavity 1 is separated from a second cavity (cavity 2) by a ‘leucine plug’ formed by L554 of opposing monomers (Fig. 2c,d) and was previously shown to be optimally suited to bind relatively flat, hydrophobic, polycyclic molecules [29], a feature which is distinct from the multidrug transporters ABCB1 and ABCC1 that form more globular

cavities [37, 38]. Access to cavity 1 from the lipid bilayer occurs via a hydrophobic 'membrane entrance' lined by residues A397, V401, L405, L539, I543 and F547 from transmembrane (TM) helices TM1b and TM5a of opposing monomers (Fig. 2e,f). The EM density clearly revealed two MZ29 molecules bound in cavity 1, each between TM1b and TM2 of one ABCG2 monomer and TM5a of the other. The binding pockets are close to the 2-fold symmetry axis of ABCG2 and the two MZ29 molecules occupy almost the entire volume of cavity 1, preventing the binding of other molecules, such as transport substrates (Fig. 2b,c,d). Cavity 2, which is fully occluded between the 'leucine plug' and the extracellular loops, does not contain any density features, indicating that no ordered inhibitors or substrates are bound at that site.

At the bottom of cavity 1 (furthest from the cytoplasmic membrane boundary), the hydrophobic residues F431, F432, M549, and L555 interact with the O-cyclopentyl group of MZ29 (Fig. 2e). In addition, the O-cyclopentyl groups of the two MZ29 molecules are 3.7 Å apart, likely forming van der Waals interactions with one another. T435 forms a hydrogen bond with the oxygen at the C-9 position and a series of residues, polar and hydrophobic, including S440, T542 and V546, form van der Waals interactions with the polycyclic core of MZ29. Furthermore, N436 forms a hydrogen bond with the nitrogen of the indole ring and F439 forms a stacking interaction with the benzene ring of the indole moiety. Residues V401, L405, I543, V546 and F547 form van der Waals interactions with the isobutyl group at the C-12 position, whereas A397, V401, L539 and I543 interact with the *tert*-butyloxycarbonyl group at the C-3 position.

Our functional analyses of synthetic Ko143 derivatives allowed us to probe the specific interactions between cavity 1 and the inhibitor in the context of *wild type* ABCG2 (Supplementary Table 5). The inhibitory capacity of the Ko143 derivatives was more affected by changes at the C-9 position than at the C-3 position (Fig. 1a,b,d). Removal of the methoxy group at the C-9 position caused a ~22-fold reduction in binding affinity as shown by differences in the dissociation constants measured for FKo143 vs FKo132 (Fig. 1c and Supplementary Table 4). This reduction in affinity and in inhibitory potency (Ko143, FKo143 and MZ15 vs Ko132 and FKo132, Fig. 1a,b) confirmed the importance of the hydrogen bond between the methoxy group of Ko143 and T435 in cavity 1 (Fig. 2e) [16, 21, 22, 35]. While small hydrophobic additions to the C-9 position (MZ25, MZ29) did not affect potency, the addition of hydrophilic groups (MZ34, MZ44) led to inactive compounds, probably because of chemical mismatch with the hydrophobic ABCG2 surface at the bottom of the cavity. Removal of the methyl group at the C-9 position (MZ21) also caused a drop in potency, which could be due to the hydrophilicity of the resulting hydroxyl group or the absence of hydrophobic

interactions with residues at the bottom of cavity 1. The exchange of the *tert*-butyloxycarbonyl end group of the substituent at the C-3 position with either a positively (as in MZ16) or a negatively charged (as in MZ35) moiety resulted in a substantial decrease in inhibitory capacity, probably due to the mismatch with the hydrophobic side chains in the vicinity of the 'membrane entrance' (Fig. 2f). Likewise, the expansion of the diketopiperazine-ring by one carbon atom (MZ92) caused a marked reduction of potency, possibly because the *tert*-butyloxycarbonyl group of the side chain was shifted, reducing the number of van der Waals interactions. Intriguingly, the inversion of the C-12 position from the *R* to the *S* configuration completely eliminated the inhibitory capability of the resulting diastereoisomer (MZ40), most likely because of an ensuing steric clash with residue N436. Finally, we can rationalize why FTC is less potent than Ko143. The E ring of FTC, as well as MZ148, cannot form favorable interactions with residues at the 'membrane entrance', which reduces the inhibitory potencies of these compounds.

We also determined the cryo-EM structure of nanodisc-reconstituted ABCG2 in complex with MZ29, but in the absence of Fab, (ABCG2-MZ29) at an overall resolution of 3.6 Å (Table 1 and Supplementary Figs. 7, 8). With the exception of the external loop EL3, which is in direct contact with Fab, the structure was indistinguishable from the Fab-bound form, and no differences in side chain conformations could be detected at this resolution (Supplementary Fig. 8f). Two MZ29 molecules were bound at exactly the same positions and in the same orientations as in the Fab-bound structure. However, the resolution was lower despite a much larger number of particles used in the 3D reconstruction, demonstrating that the use of 5D3-Fab facilitated structure determination at significantly higher resolution (Table 1 and Supplementary Figs. 2, 7), which is paramount for the detailed study of protein-ligand interactions.

Structure of the ABCG2-MB136-Fab complex

We sought to explore whether a different class of inhibitor could bind in the same pocket (cavity 1) as MZ29 or cholesterol. We synthesized and evaluated derivatives of tariquidar [28], a compound developed as a specific inhibitor of ABCB1, but whose phase III trials were discontinued mainly due to chemotherapy-related toxicity [39]. During systematic modification of tariquidar (Fig. 4a), it was observed that selectivity was drastically shifted from ABCB1 to ABCG2 by small alterations of the substitution pattern at the aromatic core [40]. To improve metabolic stability, the labile amide moiety was replaced with a triazole ring, and 'pegylation' was used to improve water solubility [24, 26]. The resulting compound,

MB136, is a novel fourth generation modulator of ABCG2, containing a triazole core and a propionyl side chain on the phenyl ring (Fig. 4a). MB136 and tariquidar inhibited E_1S transport by proteoliposome-reconstituted ABCG2, but both were less potent than either Ko143 or MZ29 (Fig. 4b and Supplementary Table 2). Indeed only at higher concentrations of MB136 and tariquidar was E_1S transport fully abolished. MB136 thermostabilized ABCG2 to a similar extent as Ko143 or MZ29 (Supplementary Fig. 1b and Supplementary Table 3).

We determined the cryo-EM structure of nanodisc-reconstituted ABCG2 in complex with MB136 and Fab (ABCG2-MB136-Fab) at an overall resolution of 3.6 Å, with the best resolved regions around 3.0 Å (Fig. 4c,d,e Table 1 and Supplementary Figs. 5, 6). The EM map revealed a strong density feature in cavity 1, overlapping in location to where MZ29 or cholesterol were previously observed (Fig. 4f). This density was distinct in shape from that observed for MZ29 and could only fit one MB136 molecule. The initial processing of the data with C2 symmetry resulted in an averaged density for MB136 that was very broad, especially close to the two-fold symmetry axis (Supplementary Fig. 6e). When the data were re-processed with C1 symmetry, asymmetric features appeared in the density that allowed the placing of MB136 and to pinpoint specific interactions (Supplementary Fig. 6f). The fact that the fit of the EM density was not as high for MB136 as that of MZ29 suggested that MB136, despite its inhibitory capability (Fig. 4b), may have multiple modes of binding by moving or sliding within cavity 1.

Cholesterol and phospholipids bound to the TMDs

The high resolution of the EM maps and the presence of a physiologically relevant mix of lipids in the nanodisc (brain polar lipid extract) allowed us to visualize and characterize ABCG2-lipid interactions. While ordered lipids were observed at similar locations in all three structures, we used the highest resolution structure (ABCG2-MZ29-Fab) for the building of the lipid molecules. Ordered membrane cholesterol and phospholipids form a belt around ABCG2, thus marking the boundary of the lipid bilayer and matching the hydrophobic protein surface (Fig. 5a). It was previously demonstrated that membrane cholesterol has an essential role for ABCG2 function, and it was proposed that ABCG2 is mainly localized in lipid rafts of the plasma membrane, where the cholesterol concentration is high [41, 42]. Thus, the ordered cholesterol molecules visualized in our structure are likely to be of functional importance. We identified five ordered cholesterol molecules per ABCG2 monomer, tightly bound in hydrophobic grooves. The best-ordered cholesterol is located between TM5b, 5c and 6b and interacts with a number of hydrophobic residues (Fig. 5). While the TMD architectures of

G-subfamily ABC transporters are likely similar, this specific pocket for cholesterol on the ABCG2 surface appears unique because the interacting residues are not conserved (Fig. 5b) and because no cholesterol-binding groove was observed in the crystal structure of the human liver cholesterol transporter ABCG5/ABCG8 (in the following abbreviated as G5G8) [43]. While studies suggested that residues L555-L558 of ABCG2 contributed to sterol binding or sensing [44], it was shown that the relevant motif was in fact not important for cholesterol binding by ABCG2 [45]. Our structure reveals that residues L555-L558 are not facing the lipid bilayer but are located in the core of ABCG2 and are some 12 Å away from the closest ordered cholesterol molecule. Therefore, these residues cannot bind membrane cholesterol directly, and the reported effects are likely to be allosteric in nature. We were also able to dock five annular phospholipids per ABCG2 monomer, which we modeled as phosphatidylethanolamine (PE), due to its abundance in the lipid extract used for nanodisc generation. Intriguingly, one of the phospholipids covers the 'membrane entrance' of ABCG2 and must therefore move if a substrate or inhibitor requires access to cavity 1 from within the lipid bilayer (Fig. 5a).

Insight into the nucleotide binding domains

The high resolution and conformational homogeneity of the inhibitor-bound ABCG2 structures allowed for a *de novo* build of the NBDs, with clear side chain density (Fig. 3 and Supplementary Fig. 4). In the absence of nucleotides, the NBDs are in a functionally 'open' conformation (apo state), with a gap between the catalytically relevant motifs. Nevertheless, the NBDs remain in contact, with approximately 680 $Å^2$ of buried surface. The contact point is formed mainly by residues preceding the NPxDF motif (289-NPADF-293 for ABCG2), which is conserved in all G-subfamily ABC transporters (Fig. 3) [44]. The overall fold of the NBDs is similar to that of G5G8, with an overall r.m.s. deviation (r.m.s.d.) of 2.3 Å and a sequence identity of 33% [43]. The distance between the Walker-A and ABC signature motifs is 16.9 Å in ABCG2 compared to the 16.5 Å for G5G8, suggesting a shared NBD spacing for all G-subfamily ABC transporters in the nucleotide-free state. The linker connecting the last α-helix of the NBDs, containing the C2 motif [46], with TM1a, is not visible in our maps, nor was it observed in the structure of G5G8, most likely due to its inherent flexibility.

The mutation Q141K is a reported single nucleotide polymorphism (SNP) of ABCG2 associated with hyperuricaemia and gout. It results in decreased expression or degradation of the protein, probably due to misfolding [47, 48]. Our structure shows that Q141 is located in the NBD on an α-helix adjacent to TM1a of the TMD, where it can form a hydrogen bond with N158, confirming the previous

in silico predictions (Supplementary Fig. 4e) [31, 34]. Given that this is a critical, non-covalent interaction between the NBD and TMD, our structures can rationalize the detrimental effect of this mutation on protein folding and function. Finally, it has also been suggested that C284, C374 and C438 form intramolecular disulfide bonds that are important for ABCG2 function [49]. Our structures reveal that these cysteines are distantly located and their functional roles are therefore unrelated to disulfide bond formation.

Stoichiometry of small-molecule inhibition

To validate our structural findings of two Ko143 derivatives (MZ29), but only one MB136 molecule bound to ABCG2, we investigated how many inhibitor molecules were required to impair the ATPase activity of ABCG2 in nanodiscs (Supplementary Table 2). We found that maximal inhibition was obtained at a ratio of one MB136 molecule for each ABCG2 homodimer. In contrast, two molecules of Ko143 were required for full inhibition (Fig. 6a). These results are in full agreement with our structural data that reveal the same stoichiometries. We observed ~50% inhibition of ATPase activity when the molar ratio of Ko143 to ABCG2 homodimer was one. This can be interpreted in two ways: A single Ko143 may be bound to every ABCG2 homodimer, reducing its activity by 50%. Alternatively, half of the ABCG2 homodimers contain two bound Ko143 molecules and are completely inhibited, while the other half contain no inhibitor and are active. While the high affinity of MZ29 did not allow a direct observation, we propose that the latter explanation is more likely because positive cooperativity can be invoked.

DISCUSSION

Our results represent the first structures of a human multidrug transporter bound to specific, small-molecule inhibitors. Both MZ29 and MB136 bind in the same cavity as the previously observed cholesterol molecules [29]. Cholesterol bound to cavity 1 either represents an analog of the *bona fide* substrate E_1S in ABCG2 or is a known substrate in other G-subfamily ABC transporters. We therefore conclude that cavity 1 in ABCG2 represents a multidrug binding site, although future substrate-bound structures are needed to validate the hypothesis that all substrates bind in this pocket. ABCG2 exhibits conformational rigidity within cavity 1, irrespective of the ligand bound, and we hypothesize that this reduces the spectrum of ligands that can bind to ABCG2. Nevertheless, binding of distinct molecules has drastically different consequences: When cholesterol was bound to

cavity 1, the ATPase rate was fully stimulated [29], whereas it was abolished when MZ29 or MB136 were bound. This demonstrates that even though the conformation of ABCG2 may be similar (inward-open), and the shape of cavity 1 conserved, the transporter readily distinguishes between substrates and inhibitors in the presence of ATP. Although cavity 1 can bind one or two inhibitors symmetrically or asymmetrically, depending on their size and shape, it remains to be demonstrated whether the same holds for substrates in a productive transport cycle, *i.e.* whether two substrates may be transported during a single cycle.

Recently, *in silico* models of human ABCG2 were reported [31, 34] that used the G5G8 crystal structure [43] as a modeling template. The G5G8 structure is different from ABCG2 in that it does not form a central, inward-facing cavity, a feature critical to the binding of small compounds in ABCG2 as revealed in this study. Based on the *in silico* models, mutagenesis experiments had been conducted. Some of the mutants showed changes in ABCG2 function in a cellular context [34]. However, none of the tested side chains are located in cavity 1 or interact with the inhibitory compounds in our structures. The observed functional effects might therefore be due to allosteric interactions or possibly direct contacts with substrates when ABCG2 adopts a different conformation from the inward-facing state reported here.

It is widely accepted that binding affinity is a key determinant of whether a molecule will be a transported substrate or an inhibitor without 'measurable' transport. Indeed many substrates for ABCG2 have affinities in the low micromolar range [29, 50, 51] whereas potent inhibitors, such as Ko143, have low nanomolar dissociation constants or IC_{50} values [24-26]. Indeed we observed a ~3000-fold difference in affinity between E_1S [29] and FKo143 (Fig. 1c, Supplementary Table 4). In order to be transported, we speculate that substrates would bind in cavity 1 before moving towards cavity 2, whereas inhibitors would remain tightly bound in cavity 1 without detectable transport. Because of the conformational coupling of the TMDs and NBDs, the movement of substrate is a prerequisite for the closing of cavity 1, the conversion of the TMDs to an inward-closed conformation, and the concomitant closure of the NBD dimer. In a productive transport cycle, NBD dimer closure is expected to result in the conversion of ABCG2 from an inward- to an outward-facing conformation, followed by hydrolysis of ATP and the release of substrate to the outside (alternating access mechanism). The effect of inhibitors binding to cavity 1, would be two-fold: Firstly, given their higher affinities, the binding of substrates is prevented by the inhibitors as they almost completely occupy the volume provided by cavity 1. In this sense, the inhibitors presented here act competitively. While less potent inhibitors, such as MB136, may move or slide within the cavity, the more potent inhibitor MZ29 showed no signs of any

motion within cavity 1. Secondly, both MZ29 and MB136 appear to lock the inward-facing state of the TMDs, which prevents closure of the NBDs due to conformational coupling and as evidenced by the inhibition of ATPase activity upon inhibitor binding (Figs. 1a and 6). Such tight conformational coupling might be due to the compact shape of ABCG2, which does not provide the same flexibility as the more elongated architectures of ABC transporters of the B- and C-subfamilies.

The inhibitor-bound structures of ABCG2 presented here should prove useful for guiding future functional experiments. They also provide a long-sought basis for rational, structure-based inhibitor development against ABCG2. To understand the specific requirements of transported substrates, novel structures of substrate-bound states in distinct conformations will be required.

METHODS

Methods, including statements of data availability and any associated accession codes and references, are available in the online version of the paper.

ACKNOWLEDGEMENTS

This research was supported by the Swiss National Science Foundation through the National Centre of Competence in Research (NCCR) TransCure, and by a Swiss Federal Institute of Technology Zurich (ETH Zurich) research grant ETH-22-14-1. J. Kowal was also supported by the TransCure Young Investigator Award. Cryo-EM data for the ABCG2-MZ29-Fab and ABCG2-MB136-Fab samples were collected at the electron microscopy facility at ETH Zurich (ScopeM), we thank P. Tittmann for technical support. Cryo-EM data for the ABCG2-MZ29 sample were collected at C-CINA, University of Basel, we thank K. Goldie, L. Kováčik and A. Fecteau-Lefebvre for technical support. We also thank J. Bloch for helpful discussions, F. Antoni, M. Scholler and D. Wifling (University of Regensburg) for technical assistance and helpful discussions and B. Sorrentino (St. Jude Children's Research Hospital) for providing the 5D3-producing hybridoma cell line.

AUTHOR CONTRIBUTIONS

I.M expressed and purified ABCG2 and 5D3-Fab. I.M and S.M.J performed MST and thermostability experiments. S.M.J reconstituted ABCG2 into liposomes and lipidic nanodiscs. J.K prepared all cryo-grids and collected cryo-EM data for

ABCG2-MZ29-Fab and ABCG2-MB136-Fab. I.M and J.K determined the structure of ABCG2-MZ29-Fab. J.K determined the structure of ABCG2-MB136-Fab. N.M.I.T and H.S collected cryo-EM data and determined the structure of ABCG2-MZ29. I.M and K.P.L refined and validated the structures with the help of J.K and N.M.I.T. M.Z synthesized Ko143 and derivatives and R.B synthesized FKo143 and FKo132, under the supervision of K-H.A. M.B synthesized MB136. M.B, S.B, G.B, B.K and A.B designed MB136 and supervised and assisted in its synthesis. S.M.J screened the compounds and performed all the ATPase and transport assays. K.P.L, K-H.A, S.M.J and I.M conceived the project. K.P.L, S.M.J and I.M planned the experiments. S.M.J, I.M and K.P.L wrote the manuscript; all authors contributed to revisions.

COMPETING FINANCIAL INTERESTS

The authors declare no competing financial interests.

1. Crowley, E., C.A. McDevitt, and R. Callaghan, *Generating inhibitors of P-glycoprotein: where to, now?* Methods Mol Biol, 2010. **596**: p. 405-32.
2. Diestra, J.E., et al., *Frequent expression of the multi-drug resistance-associated protein BCRP/MXR/ABCP/ABCG2 in human tumours detected by the BXP-21 monoclonal antibody in paraffin-embedded material.* J Pathol, 2002. **198**(2): p. 213-9.
3. Fetsch, P.A., et al., *Localization of the ABCG2 mitoxantrone resistance-associated protein in normal tissues.* Cancer Lett, 2006. **235**(1): p. 84-92.
4. Robey, R.W., et al., *ABCG2: a perspective.* Adv Drug Deliv Rev, 2009. **61**(1): p. 3-13.
5. Ishikawa, T., W. Aw, and K. Kaneko, *Metabolic Interactions of Purine Derivatives with Human ABC Transporter ABCG2: Genetic Testing to Assess Gout Risk.* Pharmaceuticals (Basel), 2013. **6**(11): p. 1347-60.
6. Gillet, J.P. and M.M. Gottesman, *Advances in the molecular detection of ABC transporters involved in multidrug resistance in cancer.* Curr Pharm Biotechnol, 2011. **12**(4): p. 686-92.
7. Gottesman, M.M., T. Fojo, and S.E. Bates, *Multidrug resistance in cancer: role of ATP-dependent transporters.* Nat Rev Cancer, 2002. **2**(1): p. 48-58.
8. Iorio, A.L., et al., *Blood-Brain Barrier and Breast Cancer Resistance Protein: A Limit to the Therapy of CNS Tumors and Neurodegenerative Diseases.* Anticancer Agents Med Chem, 2016. **16**(7): p. 810-5.
9. Sarkadi, B., et al., *Human multidrug resistance ABCB and ABCG transporters: participation in a chemoimmunity defense system.* Physiol Rev, 2006. **86**(4): p. 1179-236.
10. Sharom, F.J., *The P-glycoprotein multidrug transporter.* Essays Biochem, 2011. **50**(1): p. 161-78.

11. Bakhsheshian, J., et al., *Overlapping substrate and inhibitor specificity of human and murine ABCG2.* Drug Metab Dispos, 2013. **41**(10): p. 1805-12.
12. Imai, Y., et al., *Breast cancer resistance protein exports sulfated estrogens but not free estrogens.* Mol Pharmacol, 2003. **64**(3): p. 610-8.
13. Mao, Q. and J.D. Unadkat, *Role of the breast cancer resistance protein (BCRP/ABCG2) in drug transport--an update.* AAPS J, 2015. **17**(1): p. 65-82.
14. Mo, W. and J.T. Zhang, *Human ABCG2: structure, function, and its role in multidrug resistance.* Int J Biochem Mol Biol, 2012. **3**(1): p. 1-27.
15. Vlaming, M.L., J.S. Lagas, and A.H. Schinkel, *Physiological and pharmacological roles of ABCG2 (BCRP): recent findings in Abcg2 knockout mice.* Adv Drug Deliv Rev, 2009. **61**(1): p. 14-25.
16. Allen, J.D., et al., *Potent and specific inhibition of the breast cancer resistance protein multidrug transporter in vitro and in mouse intestine by a novel analogue of fumitremorgin C.* Mol Cancer Ther, 2002. **1**(6): p. 417-25.
17. Holland, M.L., et al., *The multidrug transporter ABCG2 (BCRP) is inhibited by plant-derived cannabinoids.* Br J Pharmacol, 2007. **152**(5): p. 815-24.
18. Kannan, P., et al., *The "specific" P-glycoprotein inhibitor Tariquidar is also a substrate and an inhibitor for breast cancer resistance protein (BCRP/ABCG2).* ACS Chem Neurosci, 2011. **2**(2): p. 82-9.
19. Peterson, B.G., et al., *High-content screening of clinically tested anticancer drugs identifies novel inhibitors of human MRP1 (ABCC1).* Pharmacol Res, 2017. **119**: p. 313-326.
20. Puentes, C.O., et al., *Solid phase synthesis of tariquidar-related modulators of ABC transporters preferring breast cancer resistance protein (ABCG2).* Bioorg Med Chem Lett, 2011. **21**(12): p. 3654-7.
21. Rabindran, S.K., et al., *Reversal of a novel multidrug resistance mechanism in human colon carcinoma cells by fumitremorgin C.* Cancer Res, 1998. **58**(24): p. 5850-8.
22. Rabindran, S.K., et al., *Fumitremorgin C reverses multidrug resistance in cells transfected with the breast cancer resistance protein.* Cancer Res, 2000. **60**(1): p. 47-50.
23. Weidner, L.D., et al., *The Inhibitor Ko143 Is Not Specific for ABCG2.* J Pharmacol Exp Ther, 2015. **354**(3): p. 384-93.
24. Bauer, S., et al., *Quinoline carboxamide-type ABCG2 modulators: indole and quinoline moieties as anilide replacements.* ChemMedChem, 2013. **8**(11): p. 1773-8.
25. Kohler, S.C. and M. Wiese, *HM30181 Derivatives as Novel Potent and Selective Inhibitors of the Breast Cancer Resistance Protein (BCRP/ABCG2).* J Med Chem, 2015. **58**(9): p. 3910-21.
26. Ochoa-Puentes, C., et al., *Benzanilide-Biphenyl Replacement: A Bioisosteric Approach to Quinoline Carboxamide-Type ABCG2 Modulators.* ACS Med Chem Lett, 2013. **4**(4): p. 393-6.
27. Pick, A., W. Klinkhammer, and M. Wiese, *Specific inhibitors of the breast cancer resistance protein (BCRP).* ChemMedChem, 2010. **5**(9): p. 1498-505.

28. Roe, M., et al., *Reversal of P-glycoprotein mediated multidrug resistance by novel anthranilamide derivatives.* Bioorg Med Chem Lett, 1999. **9**(4): p. 595-600.
29. Taylor, N.M.I., et al., *Structure of the human multidrug transporter ABCG2.* Nature, 2017. **546**(7659): p. 504-509.
30. Haider, A.J., et al., *Identification of residues in ABCG2 affecting protein trafficking and drug transport, using co-evolutionary analysis of ABCG sequences.* Biosci Rep, 2015. **35**(4).
31. Laszlo, L., B. Sarkadi, and T. Hegedus, *Jump into a New Fold-A Homology Based Model for the ABCG2/BCRP Multidrug Transporter.* PLoS One, 2016. **11**(10): p. e0164426.
32. Ni, Z., et al., *Transmembrane helices 1 and 6 of the human breast cancer resistance protein (BCRP/ABCG2): identification of polar residues important for drug transport.* Am J Physiol Cell Physiol, 2010. **299**(5): p. C1100-9.
33. Ni, Z., et al., *Identification of proline residues in or near the transmembrane helices of the human breast cancer resistance protein (BCRP/ABCG2) that are important for transport activity and substrate specificity.* Biochemistry, 2011. **50**(37): p. 8057-66.
34. Khunweeraphong, N., T. Stockner, and K. Kuchler, *The structure of the human ABC transporter ABCG2 reveals a novel mechanism for drug extrusion.* Sci Rep, 2017. **7**(1): p. 13767.
35. van Loevezijn, A., et al., *Inhibition of BCRP-mediated drug efflux by fumitremorgin-type indolyl diketopiperazines.* Bioorg Med Chem Lett, 2001. **11**(1): p. 29-32.
36. Zhou, S., et al., *The ABC transporter Bcrp1/ABCG2 is expressed in a wide variety of stem cells and is a molecular determinant of the side-population phenotype.* Nat Med, 2001. **7**(9): p. 1028-34.
37. Aller, S.G., et al., *Structure of P-glycoprotein reveals a molecular basis for poly-specific drug binding.* Science, 2009. **323**(5922): p. 1718-22.
38. Johnson, Z.L. and J. Chen, *Structural Basis of Substrate Recognition by the Multidrug Resistance Protein MRP1.* Cell, 2017. **168**(6): p. 1075-1085 e9.
39. Gergely, S., et al., *Multidrug Resistance Mediated by MDR-ABC Transporters.* Drug Resistance in Cancer Cells, 2009: p. 1-20.
40. Kuhnle, M., et al., *Potent and selective inhibitors of breast cancer resistance protein (ABCG2) derived from the p-glycoprotein (ABCB1) modulator tariquidar.* J Med Chem, 2009. **52**(4): p. 1190-7.
41. Storch, C.H., et al., *Localization of the human breast cancer resistance protein (BCRP/ABCG2) in lipid rafts/caveolae and modulation of its activity by cholesterol in vitro.* J Pharmacol Exp Ther, 2007. **323**(1): p. 257-64.
42. Szilagyi, J.T., et al., *Localization of the placental BCRP/ABCG2 transporter to lipid rafts: Role for cholesterol in mediating efflux activity.* Placenta, 2017. **55**: p. 29-36.
43. Lee, J.Y., et al., *Crystal structure of the human sterol transporter ABCG5/ABCG8.* Nature, 2016. **533**(7604): p. 561-4.

44. Telbisz, A., et al., *Regulation of the function of the human ABCG2 multidrug transporter by cholesterol and bile acids: effects of mutations in potential substrate and steroid binding sites.* Drug Metab Dispos, 2014. **42**(4): p. 575-85.
45. Velamakanni, S., et al., *A functional steroid-binding element in an ATP-binding cassette multidrug transporter.* Mol Pharmacol, 2008. **73**(1): p. 12-7.
46. Macalou, S., et al., *The linker region of breast cancer resistance protein ABCG2 is critical for coupling of ATP-dependent drug transport.* Cell Mol Life Sci, 2016. **73**(9): p. 1927-37.
47. Basseville, A. and S.E. Bates, *Gout, genetics and ABC transporters.* F1000 Biol Rep, 2011. **3**: p. 23.
48. Furukawa, T., et al., *Major SNP (Q141K) variant of human ABC transporter ABCG2 undergoes lysosomal and proteasomal degradations.* Pharm Res, 2009. **26**(2): p. 469-79.
49. Liu, Y., et al., *Effect of cysteine mutagenesis on the function and disulfide bond formation of human ABCG2.* J Pharmacol Exp Ther, 2008. **326**(1): p. 33-40.
50. Ni, Z., et al., *Structure and function of the human breast cancer resistance protein (BCRP/ABCG2).* Curr Drug Metab, 2010. **11**(7): p. 603-17.
51. Suzuki, M., et al., *ABCG2 transports sulfated conjugates of steroids and xenobiotics.* J Biol Chem, 2003. **278**(25): p. 22644-9.

Figure 1: Functional characteristics of Ko143 derivatives. a, Normalized E_1S-stimulated ATPase activity of ABCG2 in proteoliposomes. **b,** Normalized initial E_1S transport rates in proteoliposomes. In **a** and **b**, assays were performed in the presence of 50 μM E_1S and in the absence or presence of 0.5 μM competitor. Bars representing compounds with potencies equal to, or higher than, Ko143 are colored in red, whereas those with lower potencies are colored in blue. Error bars indicate the standard deviations of technical replicates (n ≥ 3). **c,** Microscale thermophoresis (MST) binding assays used to determine dissociation constants (K_D) of FKo143 and FKo132 binding to ABCG2. ABCG2 was either incubated with FKo143 only (black curve, G2+FKo143), pre-incubated with 5D3-Fab followed by addition of FKo143 (green curve, G2+Fab+FKo143), pre-incubated with FKo143 followed by addition of 5D3-Fab (purple curve, G2+FKo143+Fab) or incubated with FKo132 only (orange curve, G2+FKo132). Error bars indicate the standard deviations of technical replicates (n ≥ 4). **d,** Molecular structure of the Ko143 scaffold, with the C-3, C-9 and C-12 positions numbered, and rings A-D labeled. Changes at the C-9 (R_1) and C-3 (R_2) positions are shown.

Figure 2: Structure of the ABCG2-MZ29-Fab complex. a, Ribbon diagram of the ABCG2 homodimer, with individual G2 monomers colored pink and purple. The two Fabs were removed for clarity. Bound MZ29 molecules are shown as green sticks and labeled. **b,** EM density with bound MZ29 molecules, with the view rotated by 45° relative to **a**. The dotted line represents the two-fold symmetry axis. **c,** Vertical slice through a surface representation of ABCG2 with bound MZ29 shown as green spheres and labeled. Cavities 1 and 2 and the 'leucine plug' are indicated. **d**, Cavity 1 viewed from the cytoplasm, with NBDs of ABCG2 removed for clarity and bound MZ29 shown as green spheres and labeled. **e,** Specific interactions between MZ29 and ABCG2 residues in cavity 1. Interacting residues are shown as sticks and labeled, and hydrogen bonds are shown as dashed lines. The C-3 and C-9 positions of MZ29 are labeled in orange. **f,** Transparent surface representation of the hydrophobic 'membrane entrance' region of ABCG2 viewed from within the membrane, with one MZ29 molecule shown as green spheres, and contacting ABCG2 residues shown as sticks and labeled.

Figure 3: ABCG2 NBDs. a, The ABCG2 NBDs with the D loop, H loop, Walker A, Walker B, Signature and NPxDF motifs labeled. **b,** Surface representation of ABCG2 showing the contact point at the bottom of the two NBDs with residues indicated and a yellow ellipsoid marking the 2-fold symmetry axis.

Figure 4: Structure of MB136-bound ABCG2 revealing a central multidrug-binding site. a, Molecular structures of MB136 and tariquidar. **b,** Normalized initial E_1S transport rates of proteoliposome-reconstituted ABCG2 in the presence of 50 μM E_1S and the absence or presence of 0.5 μM competitor, except for '+MB136*' and '+Tariquidar*' where the concentration was 10 μM. Error bars represent the standard deviations of technical replicates (n ≥ 3). **c,** Vertical slice through a surface representation of ABCG2, with bound MB136 shown as yellow spheres and labeled. Cavities 1 and 2 and the 'leucine plug' are indicated. **d**, Cavity 1 viewed from the cytoplasm, with NBDs of ABCG2 removed for clarity and bound MB136 shown as yellow spheres and labeled. **e**, Extracellular view of cavity 1 showing the side chains of residues, displayed as sticks, within 4 Å of MB136 (yellow sticks). **f**, Overlay of the bound ligands in cavity 1 from the structures of ABCG2 with bound cholesterol (purple sticks, PDB ID 5NJ3), MZ29 (green sticks) and MB136 (yellow sticks) after superposition of the ABCG2 TMDs from the three structures.

Figure 5: ABCG2-lipid interactions. a, Surface representation of ABCG2 colored according to atom type. Bound cholesterol molecules are shown as pink spheres, phospholipids are shown as cyan spheres, and bound MZ29 as green spheres. Inserts: EM density with a bound cholesterol molecule indicated as pink sticks (right) and a bound phospholipid molecule, localized at the 'membrane entrance', indicated as cyan sticks (left). The numbers shown in the inserts refer to TM helices. **b,** Alignment of the G-subfamily ABC transporters showing residue conservation in the ABCG2 cholesterol 'groove'. Red asterisks highlight the residues shown in **c**. **c,** The best-resolved cholesterol 'groove' as viewed from the extracellular side. Residues interacting with the bound cholesterol are shown as sticks.

Figure 6: Proposed mechanism of inhibition. a, Normalized ATPase activity of nanodisc-reconstituted ABCG2 at varying inhibitor to ABCG2 (homodimer) ratios with Ko143 in green and MB136 in yellow. The mean from two biological replicates is plotted and error bars represent the standard deviations (n ≥ 4). **b,** Schematic of ABCG2 inhibition by small molecules. ABCG2 monomers are colored salmon and blue, disulfide bridges at EL3 are indicated by yellow, dashed lines connecting sulfur atoms, the red numbers (1 and 2) indicate cavities 1 and 2, and the 'leucine plug' is shown as a grey bar between the cavities. The binding of two MZ29

molecules (green spheres) or one MB136 molecule (yellow spheres) blocks cavity 1 and locks ABCG2 in an inward-facing open conformation. This may prevent substrate (pink trapezoid) access to cavity 1 and, simultaneously, the NBDs from closing and hydrolyzing ATP.

Cryo-EM data collection, refinement and validation statistics

	ABCG2-MZ29-Fab (EMD-3953, PDB 6ETI)	ABCG2-MB136-Fab (EMD-4246, PDB 6FEQ)	ABCG2-MZ29 (EMD-4256, PDB 6FFC)
Data collection and processing			
Magnification (nominal)	59,523 (165k)	46948 (130k)	59,523 (165k)
Voltage (kV)	300	300	300
Electron exposure (e–/Å^2)	2.0	1.6	2.0
Defocus range (μm)	-0.4 to -2.7	-0.4 to -2.5	-0.5 to -3.9
Pixel size (Å)	0.840	1.065	0.812
Symmetry imposed	C2	C1	C2
Initial particle images (no.)	587,743	529,097	2,098,186
Final particle images (no.)	284,831	306,913	402,348
Map resolution (Å)	3.10	3.60	3.56
FSC threshold	0.143	0.143	0.143
Map resolution range (Å)	3.0 to 9.0	3.0 to 9.0	3.0 to 9.0
Refinement			
Initial model used	PDB 5NJ3	PDB 6ETI	PDB 6ETI
Model resolution (Å)	3.10	3.60	3.56
FSC threshold	0.143	0.143	0.143
Model resolution range (Å)	322.5-3.1	322.5-3.1	259.7-3.6
Map sharpening *B* factor (Å^2)	-98	-163	-171
Model composition			
Nonhydrogen atoms	12,366	-	8,898
Protein residues	1582	-	1144
Ligands	76	-	76
B factors (Å^2)			

Protein	52.42	-	44.69
Ligand	49.94	-	12.47
R.m.s. deviations			
Bond lengths (Å)	0.01	-	0.007
Bond angles (°)	1.02	-	0.93
Validation			
MolProbity score	1.47	-	1.44
Clashscore	3.06	-	3.66
Poor rotamers (%)	0.30	-	0.00
Ramachandran plot			
Favored (%)	94.48	-	95.92
Allowed (%)	5.33	-	3.90
Disallowed (%)	0.19	-	0.18

Table 1: Summary of cryo-EM data for the ABCG2-MZ29-Fab, ABCG2-MB136-Fab and ABCG2-MZ29 structures. The refinement statistics for the final model of ABCG2-MZ29-Fab only include the variable domains of Fab.

ONLINE METHODS

Expression and purification of human ABCG2. Human ABCG2, containing an amino (N)-terminal Flag tag, was expressed in HEK293-EBNA (Thermo Fisher Scientific) cells [52] and purified as described previously [29]. After transfection the cells were solubilized with 1% DDM (n-dodecyl-β-d-maltopyranoside) + 0.1% CHS (cholesteryl hemisuccinate) (w/v) (Anatrace), ultracentrifuged at 100,000*g* and the supernatant was then incubated with anti-Flag M2 affinity agarose gel (Sigma). ABCG2 was eluted with Flag peptide (Sigma), loaded into a Superdex 200 10/300 column (GE Healthcare) pre-equilibrated with 40 mM HEPES pH 7.5, 150 mM NaCl, 0.026% DDM + 0.0026% CHS (w/v), and the peak fractions collected.

Size-exclusion chromatography-based thermostability assay (SEC-TS) Detergent-purified ABCG2 was incubated with or without 10 μM of inhibitor (MZ29, MB136 or Ko143) or 50 μM of transport substrate (E_1S), for 10 min at room temperature. 100 μl samples were aliquoted into thin-walled PCR tubes and heated at one temperature, ranging from 30 – 75 °C, for 10 min in a Bio-Rad Thermocycler. The samples were cooled on ice immediately, spun at 100,000*g* for

20 min at 4 °C, and then loaded onto a TSKgel G3000SWXL column (Tosoh Bioscience). Curves were plotted using the sigmoidal dose-response (variable slope) tool in GraphPad Prism 7 (GraphPad Software, La Jolla, California, USA).

Expression and purification of 5D3-Fab. 5D3 hybridoma cells, producing the 5D3 monoclonal antibody, were obtained from B. Sorrentino [36]. The cells were cultured in WHEATON CELLine Bioreactors, according to the manufacturer's protocol, and 5D3-Fab was then purified from the supernatant, as described in the Fab Preparation Kit protocol (Thermo Fisher Scientific).

ABCG2-nanodisc preparation. Membrane scaffold protein (MSP) 1D1 was expressed and purified as described previously [53]. Brain polar lipid (BPL):CHS (4:1) (w/w) was solubilized with a 3 × molar excess of sodium cholate using a ultrasonic bath. Solubilized BPL:CHS (4:1) (w/w) was mixed with MSP 1D1 and detergent-purified ABCG2 at a molar ratio of 100:5:0.2 (lipid:MSP:ABCG2). Bio-Beads were added and the sample was incubated at 4 °C overnight. Bio-Beads were removed and the sample was spun at 100,000*g* before being loaded into a Superdex 200 10/300 column (GE Healthcare) pre-equilibrated with 25 mM HEPES pH 7.5, 150 mM NaCl, and used for ATPase assays. For cryo-EM studies in the presence of Fab the sample was prepared as described above except ABCG2 was first mixed with a 3-fold molar excess of Fab, and then 10 μM inhibitor (MZ29 or MB136), before reconstitution into nanodiscs. For cryo-EM studies in the absence of Fab the sample was mixed with 10 μM MZ29 before reconstitution.

ABCG2-liposome preparation. A BPL:cholesterol (BPL:chol) (Avanti Polar Lipids) mixture was prepared at a 4:1 (w/w) ratio as described previously [54]. Briefly, the BPL:chol mixture was extruded through a 400 nm polycarbonate filter and destabilized with 0.17% (v/v) Triton X-100. Detergent-purified ABCG2 was then mixed with BPL:chol at a 100:1 (w/w) lipid:protein ratio. Detergent was removed with Bio-Beads and proteoliposomes were spun at 100,000*g*, resuspended in 25 mM HEPES pH 7.5, 150 mM NaCl at a final lipid concentration of 10 mg ml^{-1}, and the reconstitution efficiency was determined [55].

Transport assays. ABCG2 proteoliposomes were extruded through a 400 nm polycarbonate filter and diluted to 4 mg ml^{-1} lipid in 25 mM HEPES pH 7.5, 150 mM NaCl. 5mM $MgCl_2$ and 50 μM ^3H-E_1S were added, in the absence or presence of 0.5 μM of unlabeled competitor (with the exception of MB136* and tariquidar* in Fig. 4b where 10 μM was used), and incubated for 5 min at 30 °C. The transport reaction was initiated by the addition of 2 mM ATP. To stop the reaction, samples were removed, added to ice-cold stop buffer (25 mM HEPES pH 7.5, 150 mM NaCl, 100 μM unlabeled E_1S) and filtered using a Multiscreen vacuum manifold (MSFBN6B filter plate, Millipore). Radioactivity trapped on the filters was measured

using a Perkin Elmer 2450 Microbeta2 microplate scintillation counter. Curves were plotted using the nonlinear regression Michaelis–Menten analysis tool and initial transport rates from 30 s – 2 min were determined using linear regression in GraphPad Prism 7. Rates were corrected for the orientation of ABCG2 in proteoliposomes as determined and described in [29]. The normalized initial transport rates, with the uninhibited rates set to 100 %, were then plotted.

ATPase assays. ATP hydrolysis activity was measured using a technique described previously [56]. All reactions were performed at 37 °C in the presence of 2 mM ATP and 10 mM $MgCl_2$. For ATPase assays in proteoliposomes experiments were completed with 50 µM E_1S in the presence or absence of 0.5 µM competitor. For assays in ABCG2 nanodiscs, the molar ratios of Ko143 or MB136 were varied in relation to ABCG2 to determine the functional stoichiometry for both compounds. ATPase rates were determined using linear regression in GraphPad Prism 7. Rates were corrected for the orientation of ABCG2 in proteoliposomes as determined and described in [29].The normalized ATPase rates, with the uninhibited rates set to 100%, were then plotted.

Microscale thermophoresis binding assay (MST). The binding of FKo143 (G2+FKo143) or FKo132 (G2+FKo132) to ABCG2 or ABCG2-Fab was measured using microscale thermophoresis with a NanoTemper monolith NT.115 instrument [57]. A range of concentrations of detergent-purified ABCG2 (0.11 nM – 3.65 µM) were incubated with 50 nM of FKo143 or FKo132 for 10 min in assay buffer (40 mM HEPES pH 7.5, 150 mM NaCl, 0.026% DDM + 0.0026% CHS). To check the effect of 5D3-Fab on the binding of FKo143 to ABCG2, two separate samples were measured. In the first sample, ABCG2 was first pre-incubated with a 2.5 x molar excess of 5D3-Fab for 10 min prior to the addition of FKo143 (G2+Fab+FKo143). In the second sample, ABCG2 was first pre-incubated with FKo143 for 10 min prior to the addition of 5D3-Fab (G2+FKo143+Fab). The samples were then loaded into NanoTemper standard glass capillaries and microthermophoresis was carried out using 60% LED power and 40% MST. K_D values were calculated using the mass action equation via the NanoTemper software.

Sample preparation and cryo-EM data acquisition. The cryo grids were prepared using a Vitrobot Mark IV (FEI) with the environmental chamber set at 100% humidity and 4 °C. An aliquot of 4 µl purified ABCG2-MZ29-Fab, ABCG2-MB136-Fab or ABCG2-MZ29, at a protein concentration of approximately 0.4 mg ml^{-1}, was applied to glow-discharged Quantifoil (1.2/1.3) 300 mesh Cu grids. After being blotted with filter paper for 2.0 s, the grids were flash frozen in a mixture of propane and ethane, cooled with liquid nitrogen.

The final data sets were composed of 4,094, 2,468 and 9,244 micrographs for the

ABCG2-MZ29-Fab, ABCG2-MB136-Fab and ABCG2-MZ29 samples respectively. Movies were recorded semi-automatically with SerialEM on a Titan Krios operated at 300 keV and equipped with a Gatan K2 Summit and a GIF Quantum LS energy filter. Images were recorded in super-resolution counting mode with a defocus range of –0.5 to –2.5 µm.

Super-resolution pixel sizes were 0.42 Å/pixel, 0.5325 Å/pixel and 0.4058 Å/pixel for the ABCG2-MZ29-Fab, ABCG2-MB136-Fab and ABCG2-MZ29 movies respectively. For the ABCG2-MZ29-Fab sample, each stack was exposed for 10 s with an exposure time of 0.2 s per frame, resulting in 50 frames per stack and a frame dose of 2.0 $e^-/Å^2$. For ABCG2-MZ29, the data collection parameters were the same as for ABCG2-MZ29-Fab, but with the first frame removed. For the ABCG2-MB136-Fab sample, 15 s-stacks, with 0.25 s-frames and a frame dose of 1.55 $e^-/Å^2$, were recorded. All stacks were gain-normalized, motion-corrected, dose-weighted and then binned 2-fold with MotionCor2 [58]. The defocus values were estimated on the non-dose-weighted micrographs with Gctf [59].

Image processing. From the ABCG2-MZ29-Fab micrographs a total of 587,743 particles were picked with Gautomatch (http://www.mrc-lmb.cam.ac.uk/kzhang/). Image processing was performed in RELION 2.0 [60]. The picked particles were screened by 5 rounds of 2D classification. Almost all particles (543,842) were correctly assigned to 2D classes, selected and finally subjected to a global angular search 3D classification with 5 classes. A total of 284,831 particles were combined from the good 3D classes. These particles were applied for initial auto-refinement with a soft mask resulting in a 3D reconstruction with an overall resolution of 3.19 Å (for map with applied C2 symmetry) and 3.25 Å (not symmetrized map). After regrouping of the particles and adapting the soft mask in the following 3D refinement, the map resolution improved to 3.1 Å.

Image processing of the ABCG2-MB136-Fab particles was performed both in RELION 2.0 [60] and CryoSPARC [61]. A total of 529,097 ABCG2-MB136 particles were picked with Gautomatch and 2D classified in RELION 2.0. After five rounds of 2D classification and selection we obtained a final data set of 424,235 particles. These particles were used for 3D classification with 3 classes. From two good 3D classes 306,913 particles were selected for the first 3D auto-refinement with C1 and C2 symmetry. After post-processing, maps with resolutions of 3.65 Å and 3.50 Å were obtained, respectively. In parallel the same set of particles was processed in CryoSPARC. *Ab-initio* 3D reconstruction followed by homogenous 3D refinement (symmetry C1) and map sharpening resulted in map at 3.60 Å resolution. The CryoSPARC map showed much better asymmetric density inside the ABCG2 molecule, corresponding to MB136, than the map from RELION 2.0.

For ABCG2-MZ29, data were processed using RELION 2.1b. Particles (2,098,186) were picked automatically by Gautomatch, binned 4× and 2D classified in RELION. After three rounds of 2D classification, the remaining 1,087,316 particles were subjected to 3D classification into 10 classes (applying C2 symmetry). The particles from the best three classes (549,517 in total) were extracted again, this time unbinned, and subjected to 3D classification into five classes (using C2 symmetry). Four classes corresponded to “good” classes, and three of these were very similar to each other. Particles in those three classes (402,348 in total) were combined to give a final reconstruction, applying C2 symmetry, with the RELION auto-refinement procedure. After automated masking and post-processing, the resolution was estimated to be 3.56 Å.

All ABCG2-MZ29-Fab, ABCG2-MB136-Fab and ABCG2-MZ29 maps were post-processed, including soft masking, and using the automatically determined B-factor sharpening routines. The resolutions were estimated with the gold-standard Fourier shell correlation (FSC) 0.143 cut-off criterion [62]. ResMap [63] was used to calculate the local resolution maps. In the case of ABCG2-MZ29, maps filtered by local resolution were also created in RELION.

Model building and refinement. For model building, we used the post-processed map of ABCG2-MZ29-Fab at an overall resolution of 3.1 Å. The quality of the EM density was of excellent quality and allowed for the de novo building of ABCG2 and the variable domain of 5D3-Fab. The Coot program [64] was used for all model building steps and the previous ABCG2-5D3(Fab) model (PDB accession codes: 5NJ3 and 5NIV) was docked into the EM density and used as an initial reference [29]. The MZ29 coordinates and restraints were generated using eLBOW [65] and fitted into the EM density using Coot. The complete ABCG2-MZ29-Fab atomic model was refined against the working map in Phenix [66] using the program phenix.real_space_refine at a resolution limit of 3.1 Å. For the final round of model refinement, we performed global real-space refinement with standard geometry restraints as well as rotamer, Ramachandran plot, C-beta, non-crystallographic symmetry (NCS) and secondary structure restraints, coupled to reciprocal-space refinement of the B factors. The quality of the final model was analyzed by MolProbity [67] and the refinement statistics are given in Table 1. For validation of the refinement, random shifts (mean value of 0.3 Å) were introduced into the coordinates of the final refined model using the program phenix.pdbtools [66], followed by refinement with phenix.real_space_refine (using the same parameters as described before) against the first unfiltered half-map (half-map 1). The overlay between the FSC curve of the model with random displacements refined against half-map1 versus half-map 1 and the FSC curve of the same model versus half-map 2 (against which it was not refined) indicated that no over-refinement took

place.

For the ABCG2-MZ29 structure, we used the ABCG2-MZ29 sub-complex structure, obtained from the ABCG2-MZ29-Fab sample, as a starting model for rebuilding into the post-processed and RELION local resolution filtered maps. The structure was very similar, with the exception of EL3, which needed rebuilding. After manual rebuilding in Coot, the structure was refined and validated similarly to the ABCG2-MZ29-Fab structure.

For the ABCG2-MB136-Fab structure, we docked the refined ABCG2-Fab sub-complex structure, obtained from the ABCG2-MZ29-Fab sample, into the EM density using Coot. The MB136 coordinates and restraints were generated using eLBOW and fitted into the EM density using Coot.

Figure preparation. Figures were prepared using the programs PyMOL (The PyMOL Molecular Graphics System, DeLano Scientific) and GraphPad Prism 7 (GraphPad Software, La Jolla, California, USA).

Data availability. Atomic coordinates for ABCG2-MZ29-Fab (5D3-Fab variable domain only), ABCG2-MZ29 and ABCG2-MB136-Fab (5D3-Fab variable domain only) were deposited in the Protein Data Bank under accession codes 6ETI, 6FFC and 6FEQ respectively. EM data for the three structures were deposited in the Electron Microscopy Data Bank under accession codes EMD-3953 (ABCG2-MZ29-Fab), EMD-4256 (ABCG2-MZ29) and EMD-4246 (ABCG2-MB136-Fab). Source data for **Figures 1a,b,c, 4b, 6a** and **Supplementary Figure 1b** are available online. All other data are available from the corresponding author upon reasonable request. A **Life Sciences Reporting Summary** for this article is available.

52. Geisse, S., M. Jordan, and F.M. Wurm, *Large-scale transient expression of therapeutic proteins in mammalian cells.* Methods Mol Biol, 2005. **308**: p. 87-98.
53. Ritchie, T.K., et al., *Chapter 11 - Reconstitution of membrane proteins in phospholipid bilayer nanodiscs.* Methods Enzymol, 2009. **464**: p. 211-31.
54. Geertsma, E.R., et al., *Membrane reconstitution of ABC transporters and assays of translocator function.* Nat Protoc, 2008. **3**(2): p. 256-66.
55. Schaffner, W. and C. Weissmann, *A rapid, sensitive, and specific method for the determination of protein in dilute solution.* Anal Biochem, 1973. **56**(2): p. 502-14.
56. Chifflet, S., et al., *A method for the determination of inorganic phosphate in the presence of labile organic phosphate and high concentrations of protein: application to lens ATPases.* Anal Biochem, 1988. **168**(1): p. 1-4.
57. Wienken, C.J., et al., *Protein-binding assays in biological liquids using microscale thermophoresis.* Nat Commun, 2010. **1**: p. 100.

58. Zheng, S.Q., et al., *MotionCor2: anisotropic correction of beam-induced motion for improved cryo-electron microscopy.* Nat Methods, 2017. **14**(4): p. 331-332.
59. Zhang, K., *Gctf: Real-time CTF determination and correction.* J Struct Biol, 2016. **193**(1): p. 1-12.
60. Kimanius, D., et al., *Accelerated cryo-EM structure determination with parallelisation using GPUs in RELION-2.* Elife, 2016. **5**.
61. Punjani, A., et al., *cryoSPARC: algorithms for rapid unsupervised cryo-EM structure determination.* Nat Methods, 2017. **14**(3): p. 290-296.
62. Rosenthal, P.B. and R. Henderson, *Optimal determination of particle orientation, absolute hand, and contrast loss in single-particle electron cryomicroscopy.* J Mol Biol, 2003. **333**(4): p. 721-45.
63. Kucukelbir, A., F.J. Sigworth, and H.D. Tagare, *Quantifying the local resolution of cryo-EM density maps.* Nat Methods, 2014. **11**(1): p. 63-5.
64. Emsley, P., et al., *Features and development of Coot.* Acta Crystallogr D Biol Crystallogr, 2010. **66**(Pt 4): p. 486-501.
65. Moriarty, N.W., R.W. Grosse-Kunstleve, and P.D. Adams, *electronic Ligand Builder and Optimization Workbench (eLBOW): a tool for ligand coordinate and restraint generation.* Acta Crystallogr D Biol Crystallogr, 2009. **65**(Pt 10): p. 1074-80.
66. Adams, P.D., et al., *PHENIX: a comprehensive Python-based system for macromolecular structure solution.* Acta Crystallogr D Biol Crystallogr, 2010. **66**(Pt 2): p. 213-21.
67. Chen, V.B., et al., *MolProbity: all-atom structure validation for macromolecular crystallography.* Acta Crystallogr D Biol Crystallogr, 2010. **66**(Pt 1): p. 12-21.

Fig. 1

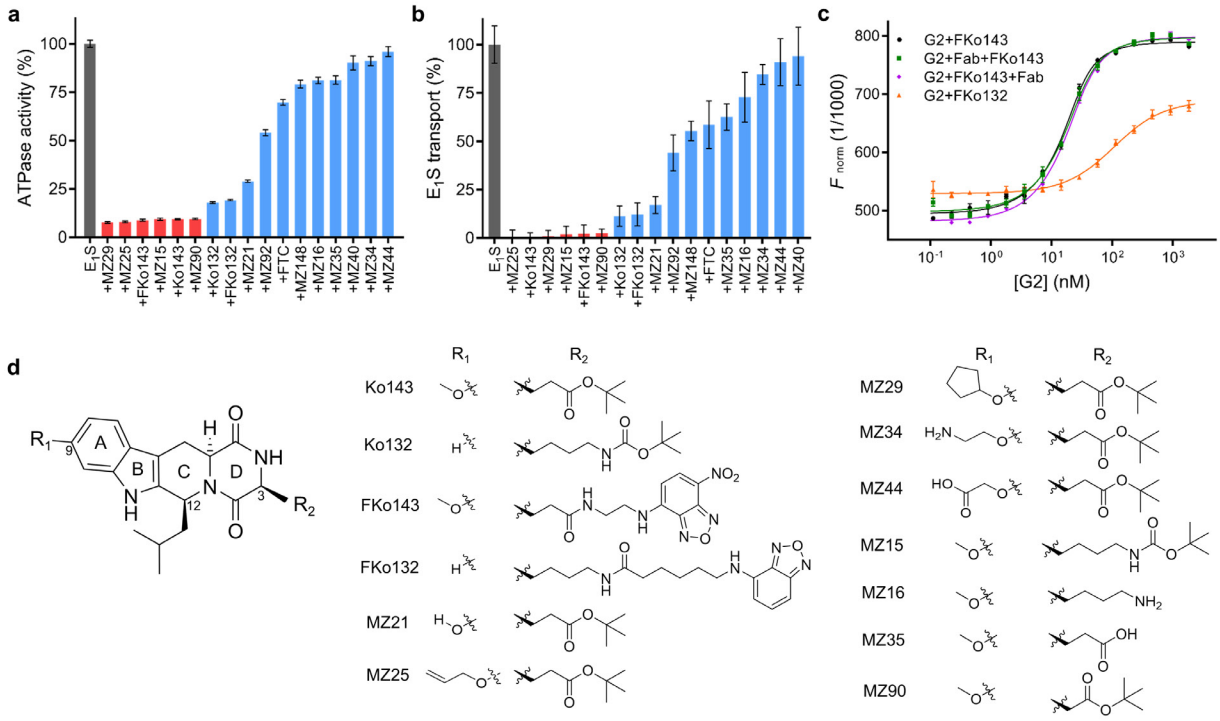
a
ATPase activity (%)
E1S
+MZ29
+MZ25
+FKo143
+MZ15
+Ko143
+MZ90
+Ko132
+FKo132
+MZ21
+MZ92
+FTC
+MZ148
+MZ16
+MZ35
+MZ40
+MZ34
+MZ44
b
E1S transport (%)
E1S
+MZ25
+Ko143
+MZ29
+MZ15
+FKo143
+MZ90
+Ko132
+FKo132
+MZ21
+MZ92
+MZ148
+FTC
+MZ35
+MZ16
+MZ34
+MZ44
+MZ40
c
G2+FKo143
G2+Fab+FKo143
G2+FKo143+Fab
G2+FKo132
Fnorm (1/1000)
[G2] (nM)
d
R1
R2
Ko143
Ko132
FKo143
FKo132
MZ21
MZ25
MZ29
MZ34
MZ44
MZ15
MZ16
MZ35
MZ90

Fig. 2

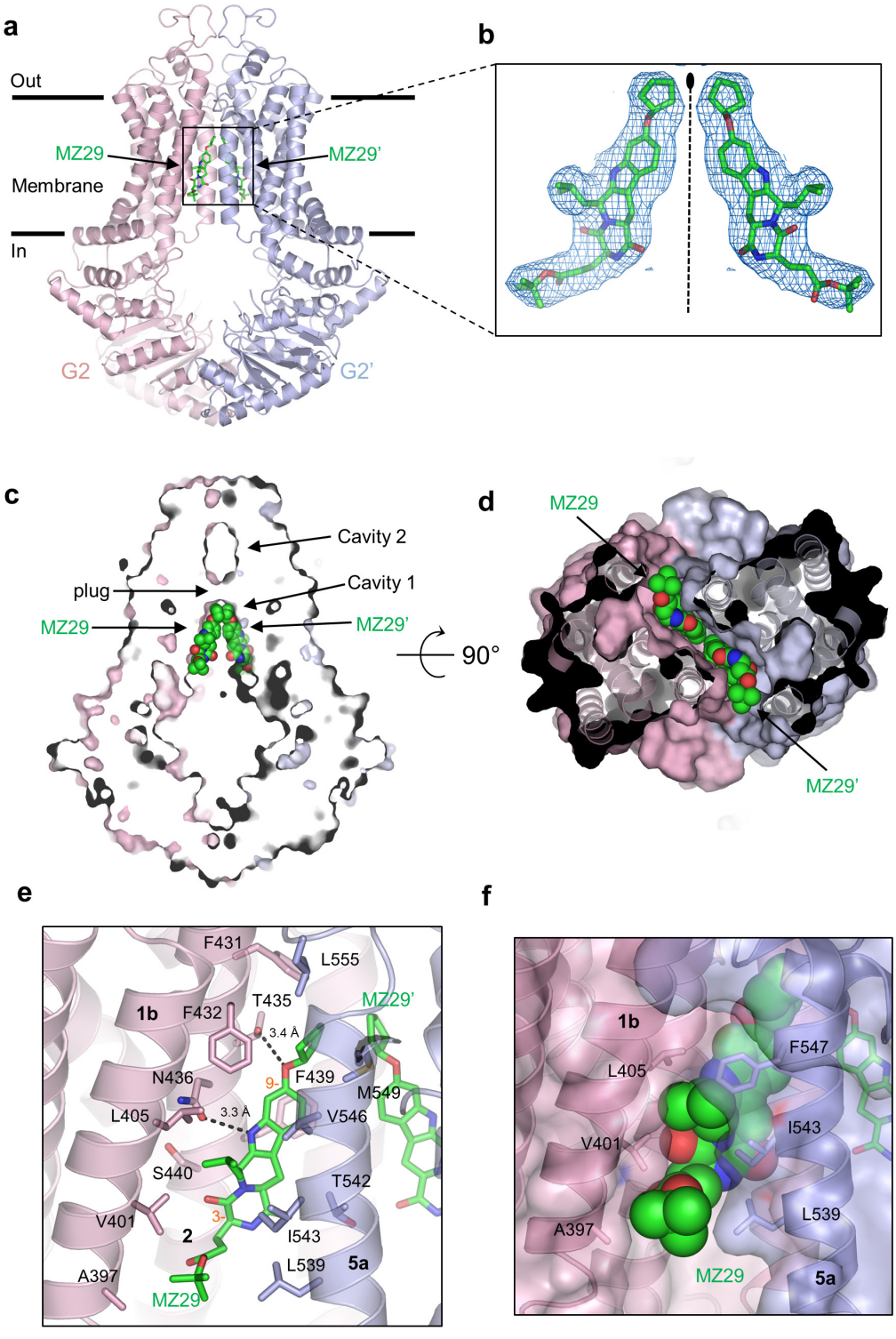
a
Out
MZ29
MZ29'
Membrane
In
G2
G2'
b
c
Cavity 2
plug
Cavity 1
MZ29
MZ29'
90°
d
MZ29
MZ29'
e
F431
L555
T435
MZ29'
1b
F432
3.4 Å
N436
9-
F439
M549
L405
3.3 Å
V546
S440
T542
3-
V401
2
I543
A397
L539
5a
MZ29
f
1b
F547
L405
V401
I543
L539
A397
MZ29
5a

Fig. 3

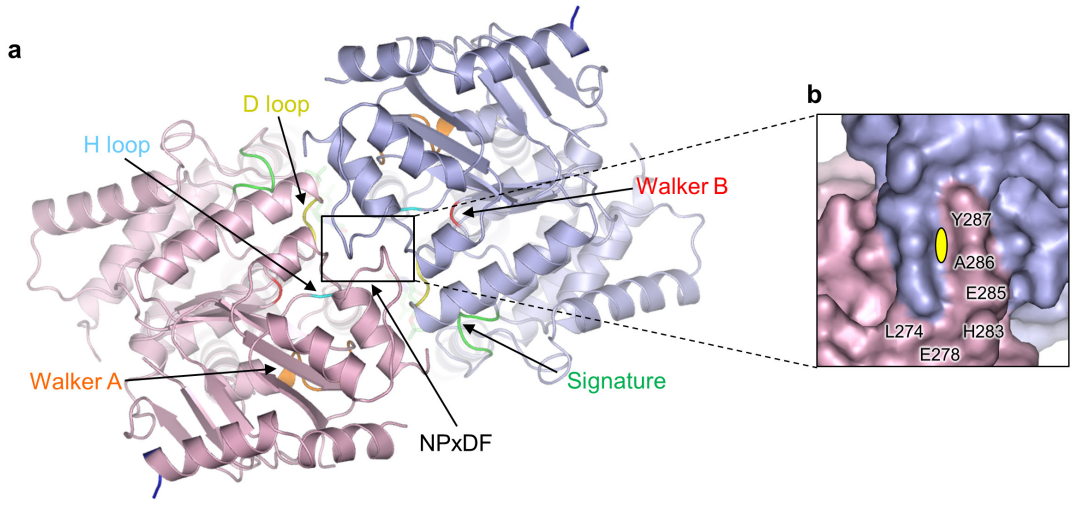
a
b
D loop
H loop
Walker B
Walker A
Signature
NPxDF
Y287
A286
E285
L274
H283
E278

Fig. 4

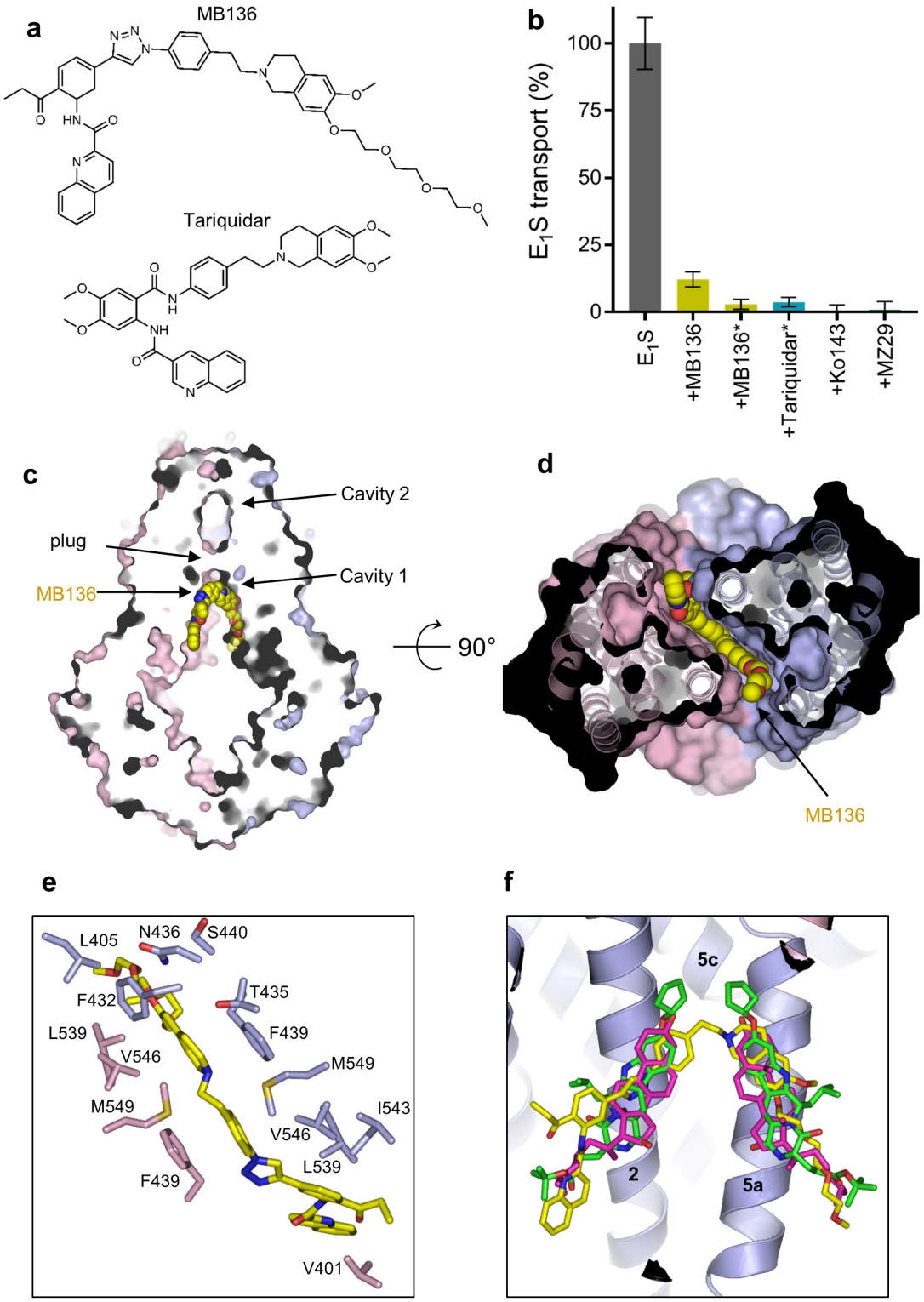
a
MB136
Tariquidar
b
E1S transport (%)
100
75
50
25
0
E1S
+MB136
+MB136*
+Tariquidar*
+Ko143
+MZ29
c
Cavity 2
plug
Cavity 1
MB136
90°
d
MB136
e
L405
N436
S440
F432
T435
L539
F439
V546
M549
M549
I543
V546
L539
F439
V401
f
5c
2
5a

Fig. 5

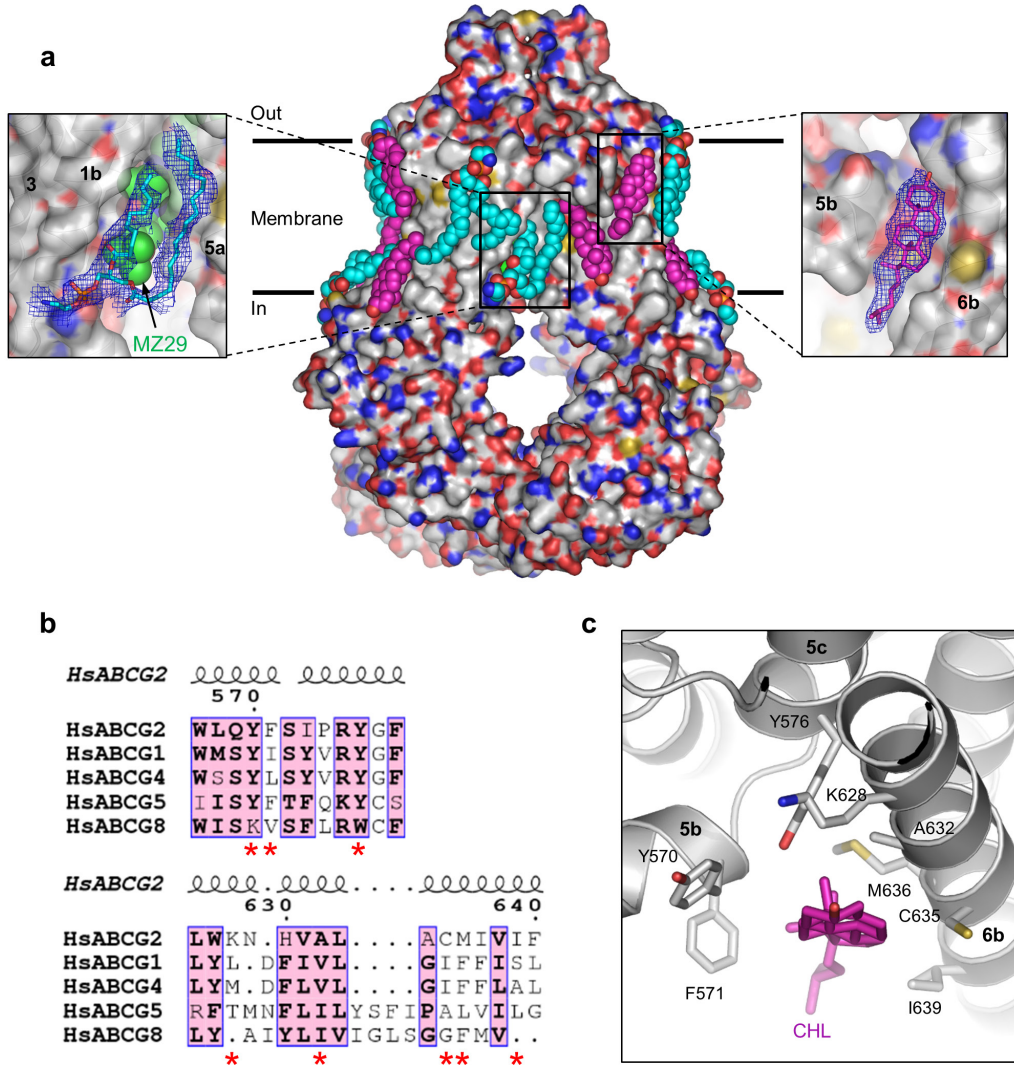
a
Out
Membrane
In
3
1b
5a
MZ29
5b
6b
b
HsABCG2
570
HsABCG2 WLQYFSIPRYGF
HsABCG1 WMSYISYVRYGF
HsABCG4 WSSYLSYVRYGF
HsABCG5 IISYFTFQKYCS
HsABCG8 WISKVSFLRWCF
HsABCG2
630
640
HsABCG2 LWKN.HVAL....ACMIVIF
HsABCG1 LYL.DFIVL....GIFFISL
HsABCG4 LYM.DFLVL....GIFFLAL
HsABCG5 RFTMNFLILYSFIPALVILG
HsABCG8 LY.AIYLIVIGLSGGFMV..
c
5c
Y576
K628
A632
5b
Y570
M636
C635
6b
F571
I639
CHL

Fig. 6

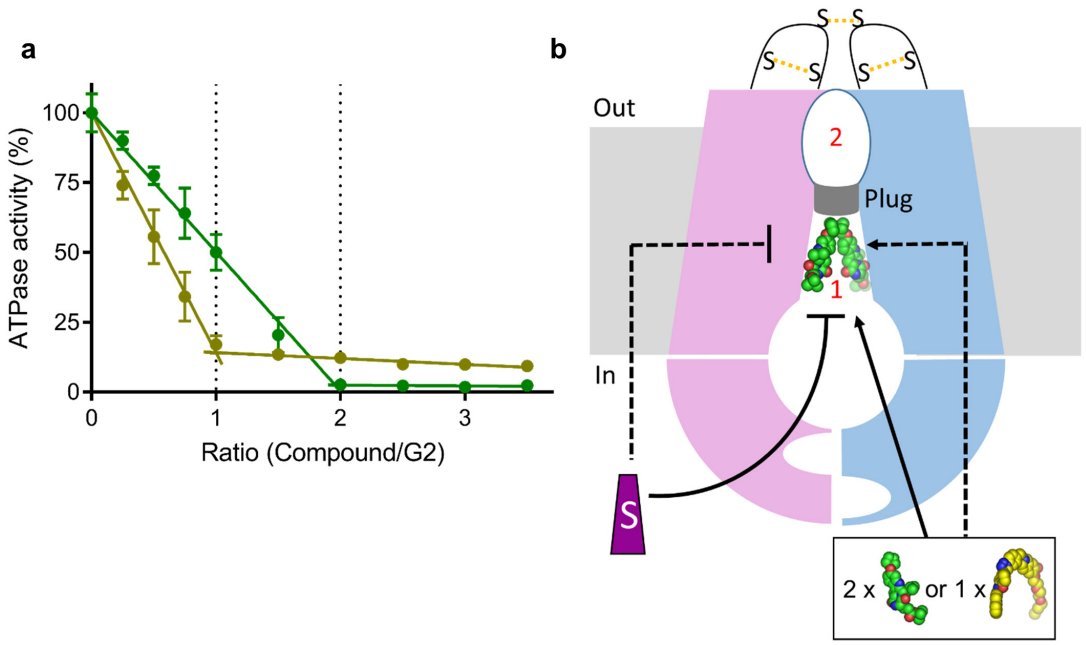
a
ATPase activity (%)
100
75
50
25
0
0
1
2
3
Ratio (Compound/G2)
b
S
S
S
S
S
S
Out
2
Plug
1
In
S
2 x
or 1 x

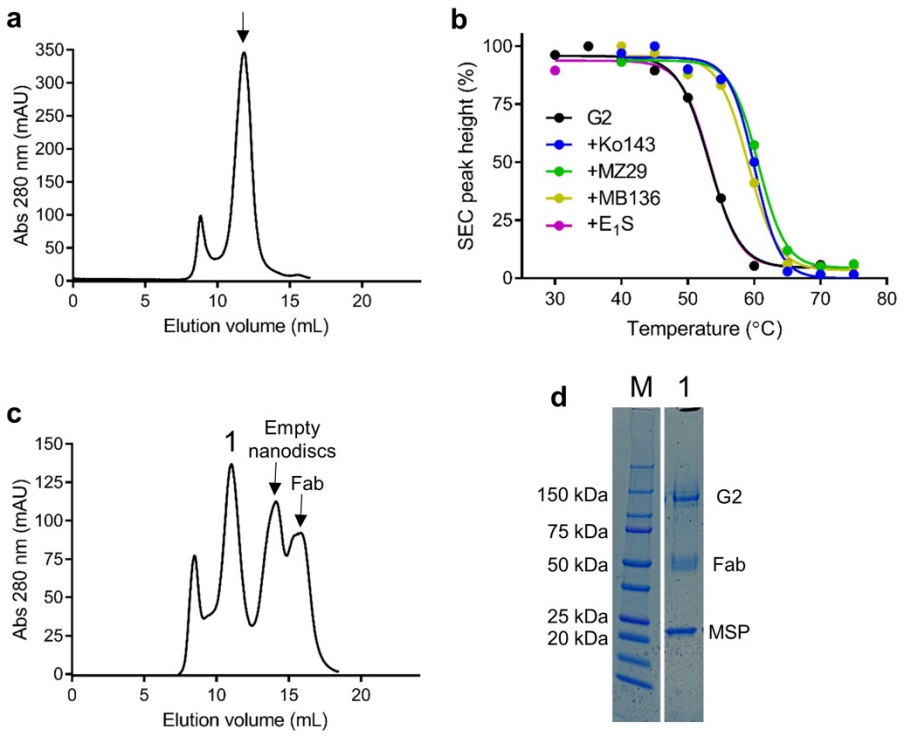

Supplementary Figure 1

Purification of ABCG2, SEC-TS and reconstitution of ABCG2-MZ29-Fab into nanodiscs.

a, Preparative SEC profile of detergent-purified ABCG2. The fraction used for SEC-TS and nanodisc preparation is indicated with an arrow. **b,** SEC-TS of ABCG2 before or after the addition of specified inhibitors at 10 μM concentration and E_1S at 50 μM concentration. **c,** Preparative SEC profile of the nanodisc-reconstituted ABCG2-MZ29-Fab complex. The fraction used for cryo-EM grid preparation and SDS-PAGE analysis is indicated by '1'. **d,** Non-reducing SDS-PAGE of the nanodisc-reconstituted ABCG2-MZ29-Fab complex shown in **c**.

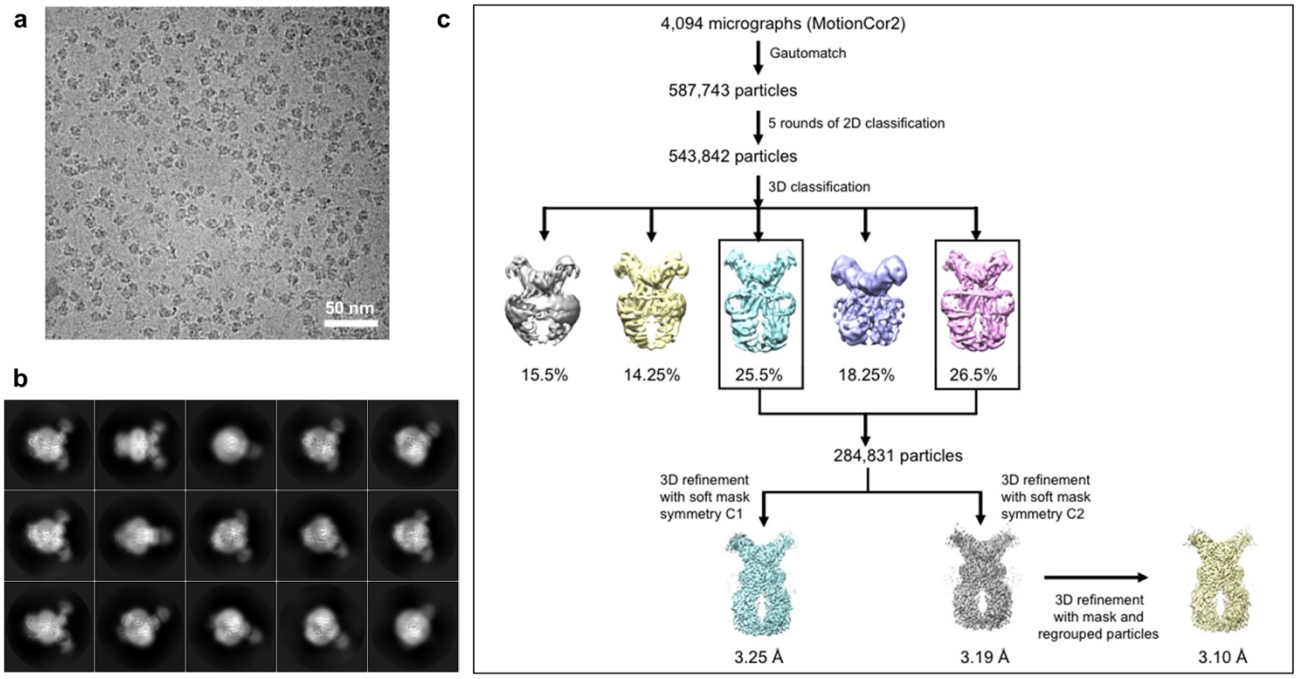

Supplementary Figure 2

Cryo-EM map generation and data processing flow chart of the ABCG2-MZ29-Fab complex.

a, An example micrograph (drift-corrected, dose-weighted, and low-pass filtered to 20 Å) of the nanodisc-reconstituted ABCG2–MZ29-Fab data set. White scale bar, 50 nm. **b**, Averages of 15 representative two-dimensional class averages of the final round of two-dimensional classification, sorted in decreasing order by the number of particles assigned to each class. **c**, The flow chart for the cryo-EM data processing and structure determination of the ABCG2-MZ29-Fab complex.

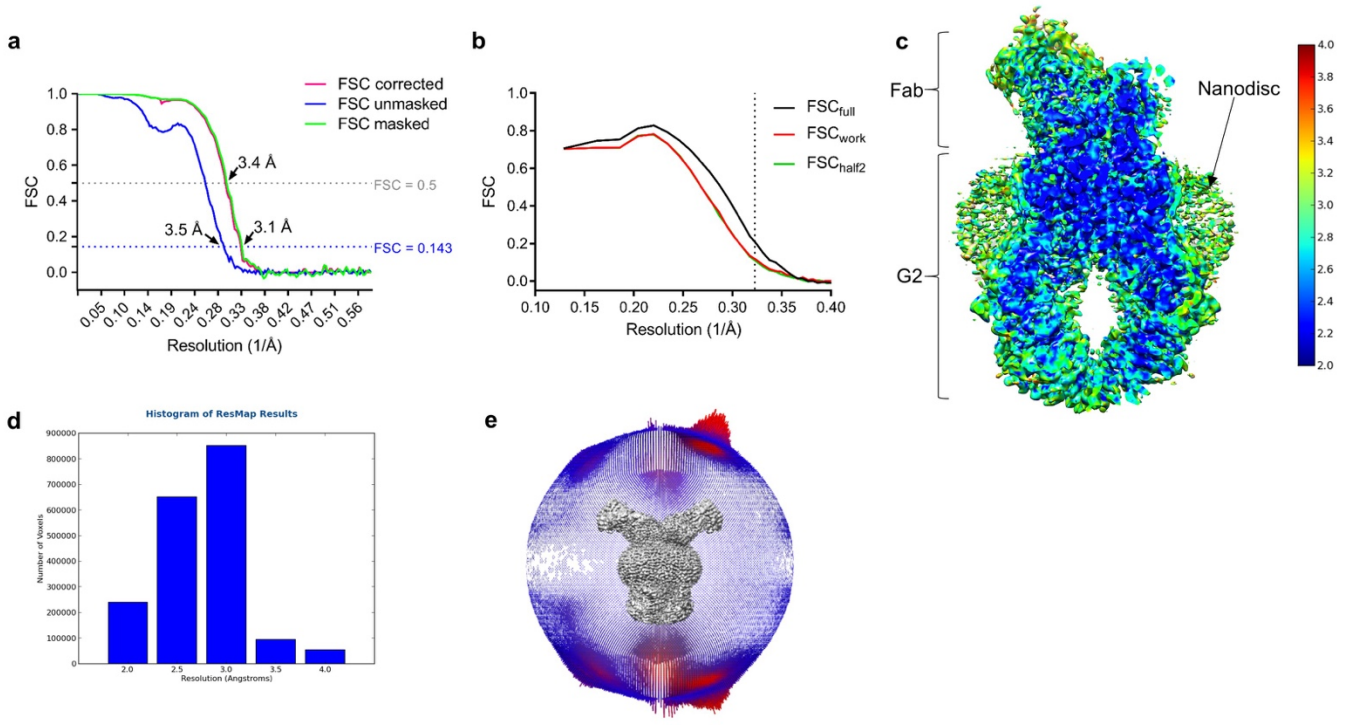

Supplementary Figure 3

Atomic model refinement and local resolution of the ABCG2-MZ29-Fab complex.

a, FSC from the RELION auto-refine procedure of the unmasked half-maps (blue), the random-phase corrected half-maps (brown), the half-maps after masking (cyan), and the half-maps after masking and correction for the influence of the mask (pink). A horizontal line (blue) is drawn for the FSC = 0.143 criterion. For both the unmasked and the corrected FSC curves, their intersection with the FSC = 0.143 line is indicated by an arrow, and the resolution at this point is indicated. **b**, FSC curve of the final 3.1 Å refined model versus the map it was refined against (FSC_{full}, black line). FSC curve of the final model with introduced shifts (mean value of 0.3 Å) refined against the first of two independent half-maps (half-map 1) (to which it was refined against; FSC_{work} red line) or the same refined model versus the second independent half-map (to which is was not refined; FSC_{half2}, green line). **c**, Full view of the RELION local-resolution-filtered map of ABCG2-MZ29-Fab colored by local resolution as calculated by ResMap with the clipping plane in the middle of the molecule. ABCG2, Fab and nanodiscs are labeled. **d,** Resolution distribution histogram generated in ResMap. **e**, Angular distribution plot for the final reconstruction.

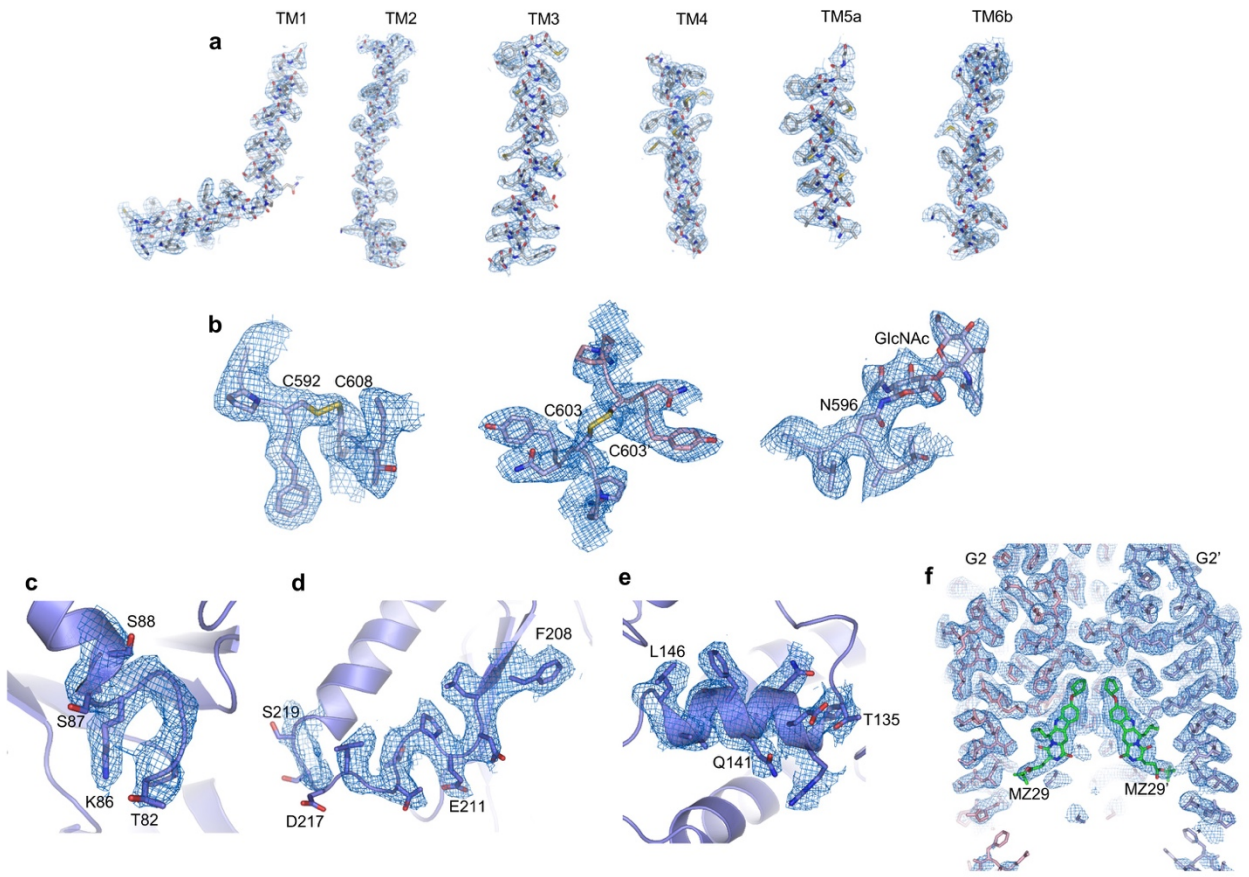

Supplementary Figure 4

Fit of the model to the density of the ABCG2-MZ29-Fab complex.

a, Fit of the TM helices of the final model of the ABCG2 TMD to the post-processed and masked map from RELION. A region of up to 2 Å around the atoms is shown. **b**, Same as **a** but showing the intramolecular disulfide (C592-C608), the intermolecular disulfide (C603-C603') and N596 decorated with two GlcNAcs. **c**, Same as **a** but showing the Walker A motif with selected residues numbered. **d,** Same as **a** but showing the Walker B motif and the D loop. **e**, Same as **a** but showing the α-helix containing Q141 with selected residues numbered. **f**, Same as **a** but showing the fit of MZ29 and surrounding residues.

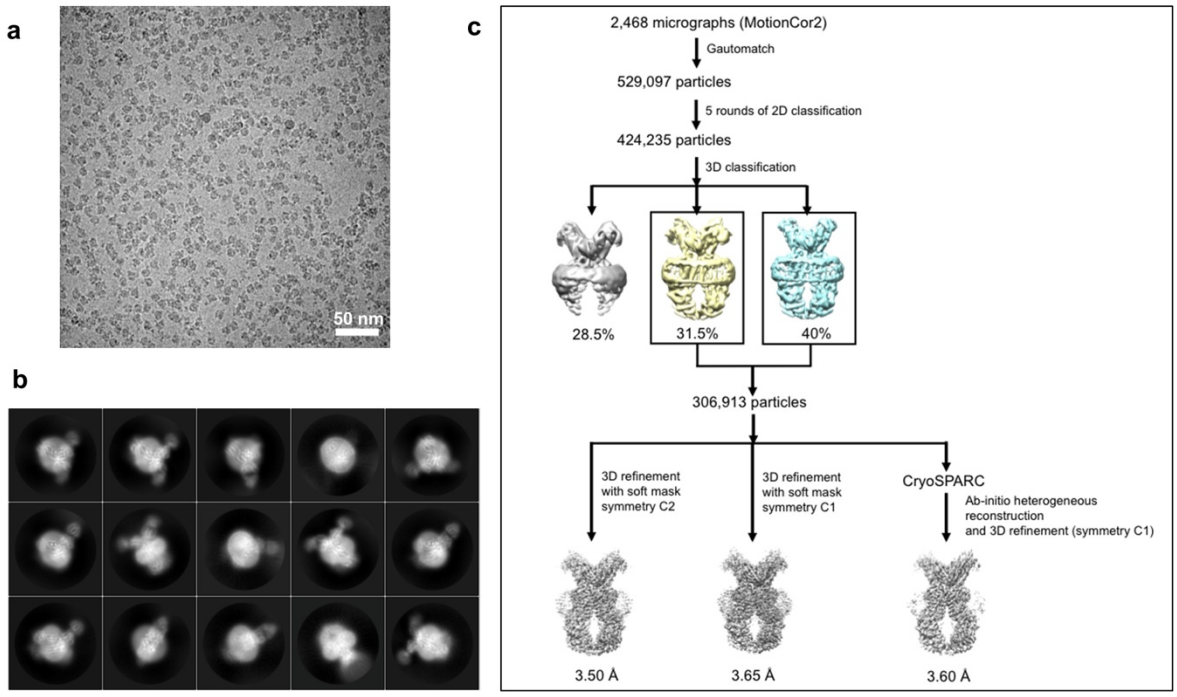

Supplementary Figure 5

Cryo-EM map generation and data processing flow chart of the ABCG2-MB136-Fab complex.

a, An example micrograph (drift-corrected, dose-weighted, and low-pass filtered to 20 Å) of the nanodisc-reconstituted ABCG2–MB136-Fab data set. White scale bar, 50 nm. **b**, Averages of 15 representative two-dimensional class averages of the final round of two-dimensional classification, sorted in decreasing order by the number of particles assigned to each class. **c**, The flow chart for the cryo-EM data processing and structure determination of the ABCG2-MB136-Fab complex.

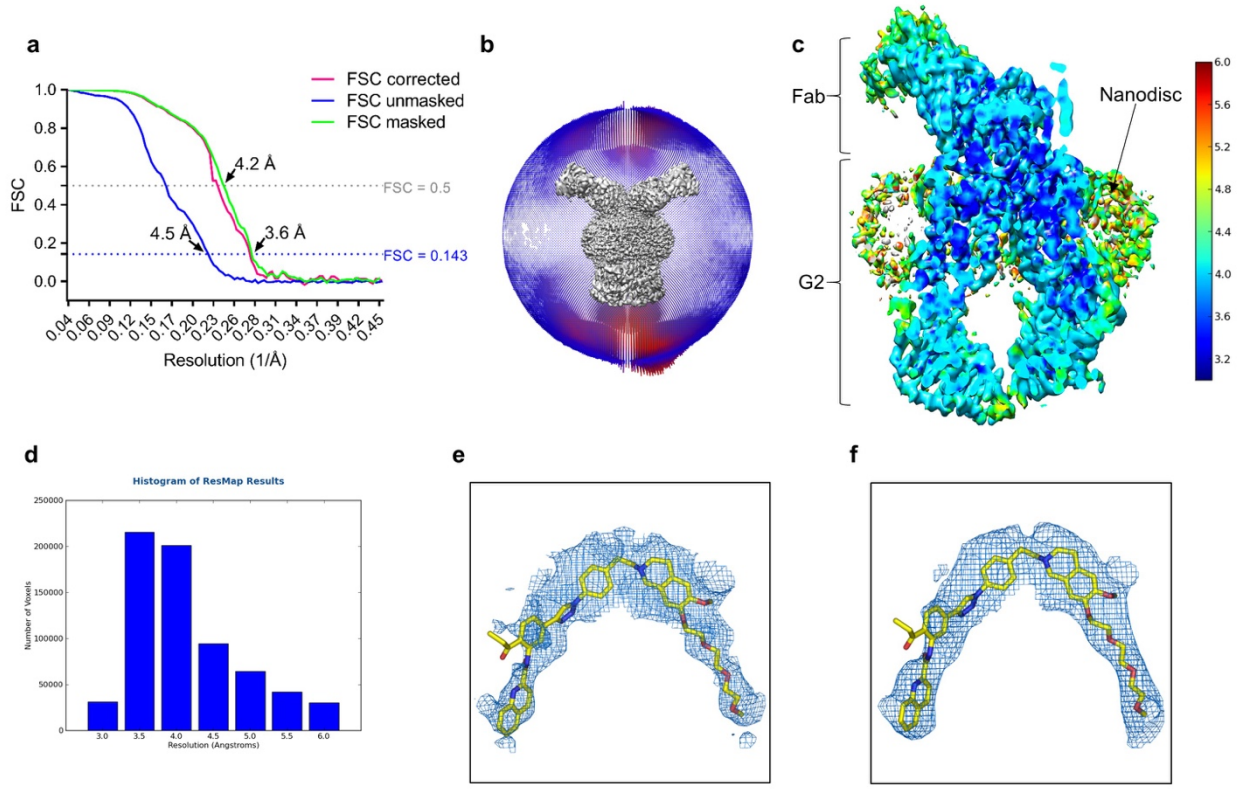

Supplementary Figure 6

Atomic model refinement and local resolution of the ABCG2-MB136-Fab complex.

a, FSC from the RELION auto-refine procedure of the unmasked half-maps (blue), the random-phase corrected half-maps (brown), the half-maps after masking (cyan), and the half-maps after masking and correction for the influence of the mask (pink). A horizontal line (blue) is drawn for the FSC = 0.143 criterion. For both the unmasked and the corrected FSC curves, their intersection with the FSC = 0.143 line is indicated by an arrow, and the resolution at this point is indicated. **b**, Angular distribution plot for the final reconstruction. **c**, Full view of the RELION local-resolution-filtered map of ABCG2-MB136-Fab colored by local resolution as calculated by ResMap with the clipping plane in the middle of the molecule. ABCG2, Fab and nanodiscs are labeled. **d,** Resolution distribution histogram generated in ResMap. **e,** Fit of one MB136 molecule into the EM density of the ABCG2-MB136-Fab structure processed with C2 symmetry. **f,** Fit of one MB136 molecule into the EM density of the ABCG2-MB136-Fab structure processed with C1 symmetry.

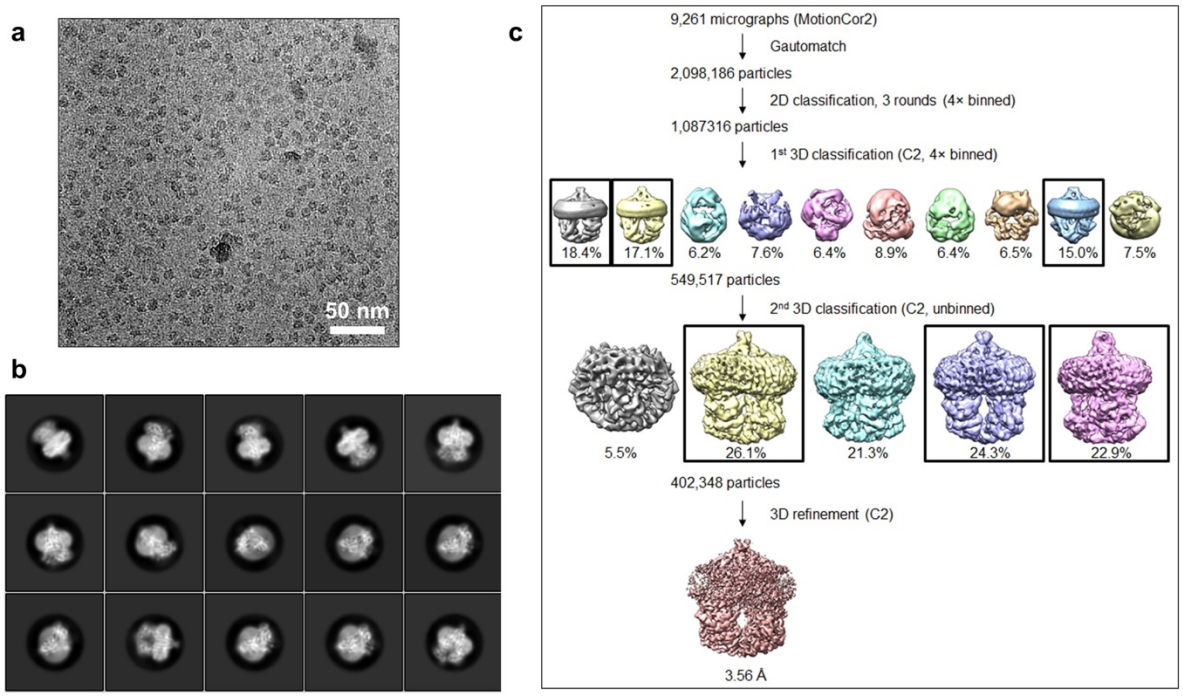

Supplementary Figure 7

Cryo-EM map generation and data processing flow chart of the ABCG2-MZ29 complex.

a, An example micrograph (drift-corrected, dose-weighted, and low-pass filtered to 20 Å) of the nanodisc-reconstituted ABCG2–MZ29 data set. White scale bar, 50 nm. **b**, Averages of 15 representative two-dimensional class averages of the final round of two-dimensional classification, sorted in decreasing order by the number of particles assigned to each class. **c**, The flow chart for the cryo-EM data processing and structure determination of the ABCG2-MZ29 complex.

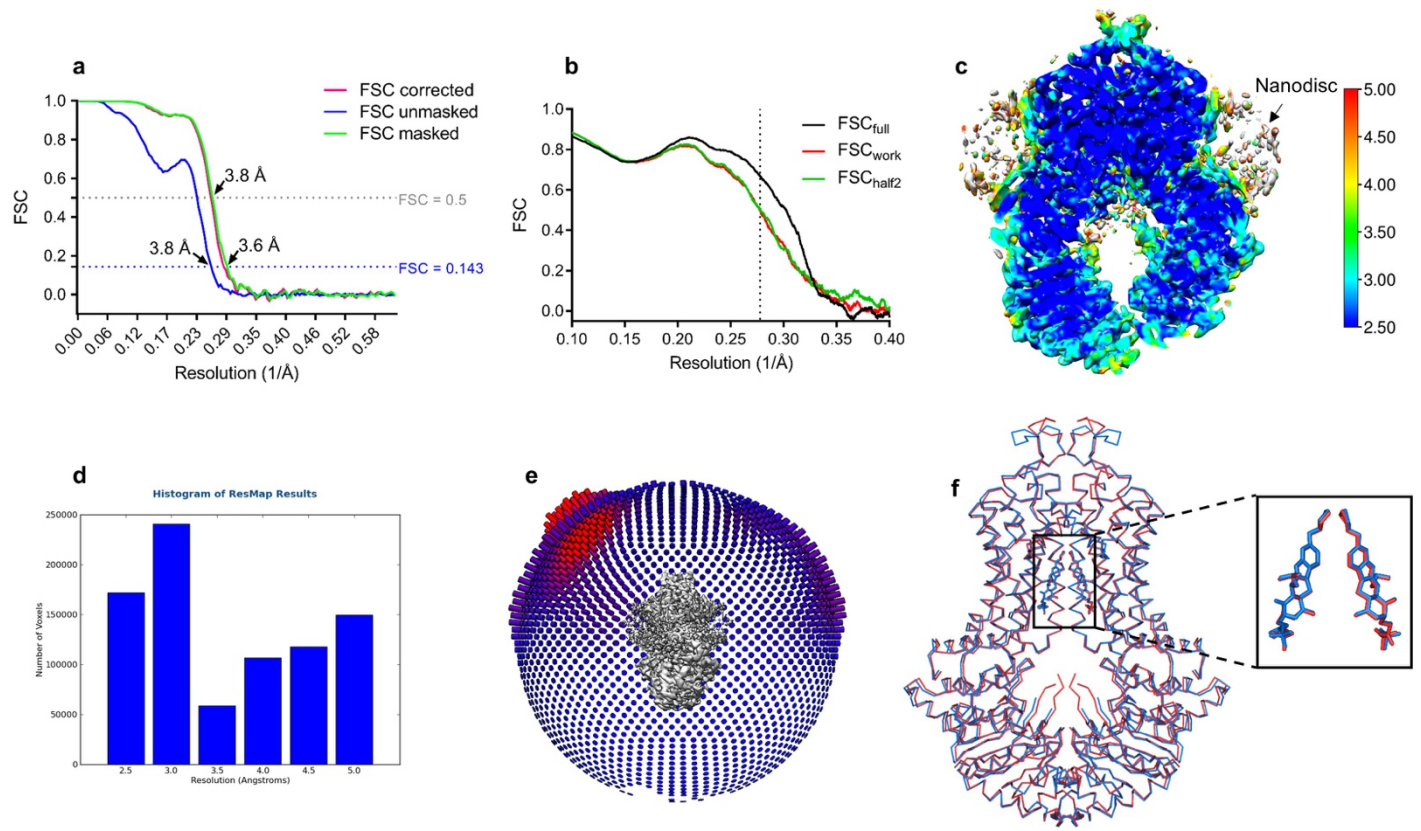

Supplementary Figure 8

Atomic model refinement and local resolution of the ABCG2-MZ29 complex.

a, FSC from the RELION auto-refine procedure of the unmasked half-maps (blue), the random-phase corrected half-maps (brown), the half-maps after masking (cyan), and the half-maps after masking and correction for the influence of the mask (pink). A horizontal line (blue) is drawn for the FSC = 0.143 criterion. For both the unmasked and the corrected FSC curves, their intersection with the FSC = 0.143 line is indicated by an arrow, and the resolution at this point is indicated. **b**, FSC curve of the final 3.56 Å refined model versus the map it was refined against (FSC_{full}, black line). FSC curve of the final model with introduced shifts (mean value of 0.3 Å) refined against the first of two independent half-maps (half-map1) (to which it was refined against; FSC_{work} red line) or the same refined model versus the second independent half-map (to which is was not refined; FSC_{half2}, green line). **c**, Full view of the RELION local resolution filtered map of ABCG2-MZ29 colored by local resolution as calculated by ResMap with the clipping plane in the middle of the molecule. **d**, Resolution distribution histogram generated in ResMap. **e**, Angular distribution plot for the final reconstruction. **f**, Superposition of the ABCG2-MZ29-Fab structure with the Fabs removed (blue) and the ABCG2-MZ29 structure (red). The insert shows the superposition of the bound MZ29 molecules.

Molecular structures of FTC and Ko143 derivatives

FTC	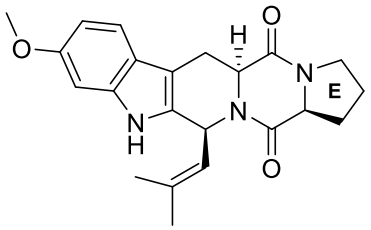
MZ148	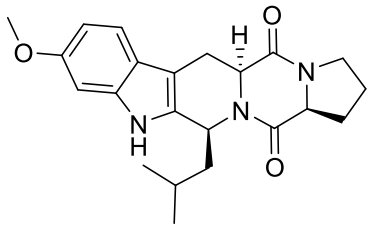
MZ40	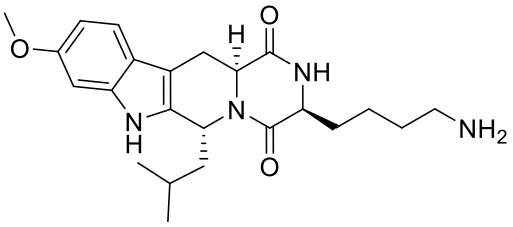
MZ92	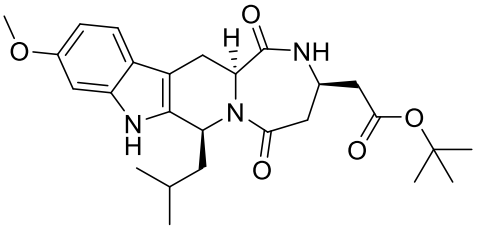

Supplementary Table 1: Molecular structure of FTC, with the E-ring labeled, and compounds with modifications at positions other than C-9 (R^1) and C-3 (R^2).

ATPase rates and the initial E_1S transport rate

Sample	ATPase rate (nmol Pi/min/mg)	Initial E_1S transport rate (nmol/min/mg)
G2 proteolipoosomes (+E_1S)	780 ± 15	20 ± 2
G2 nanodiscs	750 ± 51	-

Supplementary Table 2: The ATPase rate in proteoliposomes from the 100% value shown in Figure 1a, the initial E_1S transport rate from the 100% value shown in Figures 1b and 4b, and the ATPase rate in nanodiscs from the 100% value shown in Figure 6a. Error denotes the standard deviation of technical replicates (n ≥ 7).

Thermostability values determined using SEC-TS

Sample	TS (°C)
G2	53.2 ± 0.3
G2+Ko143	60.1 ± 0.4
G2+MZ29	60.6 ± 0.4
G2+MB136	59.1 ± 0.5
G2+E_1S	53.4 ± 0.4

Supplementary Table 3: Size exclusion chromatography thermostability (SEC-TS) values determined from the plots shown in Supplementary Figure 1b. Error denotes standard deviation of the fit.

***K_D* values determined using microscale thermophoresis (MST)**

Sample	K_D (nM)
G2+FKo143	4.4 ± 0.2
G2+Fab+FKo143	6.4 ± 0.2
G2+FKo143+Fab	6.7 ± 0.2
G2+FKo132	94.4 ± 4.1

Supplementary Table 4: K_D values for the binding of FKo143, in the presence or absence of 5D3-Fab, or FKo132 to ABCG2 from the data shown in Figure 1d. Error denotes the standard deviation of technical replicates (n ≥ 4).

ABCG2 residues that interact with MZ29 in the ABCG2-MZ29-Fab structure

TM α-helix	Residue
1b	A397
	V401
	L405
2	F431
	F432
	T435
	N436
	F439
	S440
5a	L539
	T542
	I543
	V546
	F547
	M549
	L555

Supplementary Table 5: Residues within 4 Å that interact with MZ29 in the ABCG2-MZ29-Fab structure.

SUPPLEMENTARY NOTES

Synthesis of Ko143 derivatives

General Information. All solvents used for reactions were purchased as anhydrous grade from Acros (puriss. dried over molecular sieves; H_2O <0.005%) and used without purification. Solvents for extractions, flash column chromatography and thin layer chromatography were purchased as commercial grade and distilled prior to use. All non-aqueous reactions were performed under an argon atmosphere using flame-dried glassware and standard syringe/septa techniques. All other commercially available reagents were used without further purification, unless otherwise noted. In general, reactions were magnetically stirred and monitored by thin-layer chromatography (TLC) performed on Merck TLC aluminum sheets (silica gel 60 F254). Spots were visualized with UV light (λ = 254 nm) or through staining with $Ce_2(SO_4)_3$/phosphomolybdic acid/H_2SO_4 (CPS) or $KMnO_4/K_2CO_3$. Purification of products by flash column chromatography (FC) was performed using Fluka silica gel 60 (particle size 40–63 μm). **Melting points** were obtained in open capillary tubes using a Büchi melting point apparatus B-540 and are uncorrected. **^{1}H- and ^{13}C-NMR spectra** were recorded in $CDCl_3$, DMSO-*d*$_6$ or CD_3OD-*d*$_4$ on a Bruker AV-400 400 MHz or on a Bruker AV-500 500 MHz spectrometer at room temperature. Chemical shifts (δ) are reported in ppm and are referenced to chloroform (δ 7.26 ppm for ^{1}H, δ 77.16 ppm for ^{13}C), methanol (δ 3.31 ppm for ^{1}H, δ 49.00 ppm for ^{13}C) or dimethylsulfoxide (δ 2.50 ppm for ^{1}H, δ 39.52 ppm for ^{13}C), respectively. All ^{13}C-NMR spectra were measured with complete proton decoupling. Data for NMR spectra are reported as follows: s = singlet, d = doublet, t = triplet, q = quartet, quint. = quintet, sext. = sextet, m = multiplet, br = broad signal, J = coupling constant in Hz. **Infrared spectra (IR)** were recorded on a Jasco FT/IR-6200 instrument. Resonance frequencies are given as wavenumbers in cm^{-1}. **Optical rotations** were measured on a Jasco P-1020 polarimeter and are reported as follows: $[\alpha]_D^{20}$, concentration (g/100 ml) and solvent. **High resolution mass spectra** were recorded by the ETH Zürich MS service; HRMS (ESI) spectra were obtained on a Varian IonSpec spectrometer.
HPLC analyses were carried out on a Gilson apparatus (pump: 331, UV/VIS: 156, fraction collector: 204). Conditions, columns, wavelengths and retention times (R_t) are indicated for the specific case.

General procedure for amide bond formation with carbolines MZ7 and MZ17: GP1 [1]. To a solution of the N□-Fmoc-protected amino acid 1.5 eq.) in CH_2Cl_2 (0.076 M) was added trichloroacetonitrile (3.7 eq). Then a solution of PPh_3 (3.0 eq.) in CH_2Cl_2 (0.18 M) was added slowly at r.t. and the reaction mixture was stirred

for 40 min. Then a solution of carboline **MZ7** or **MZ17** (1.0 eq.) in CH_2Cl_2 (0.040 M) was added. The resulting precipitate was redissolved by addition of Et_3N (2.3 eq.) in CH_2Cl_2 (0.74 M) and the mixture was stirred at room temperature for 1.5 h. The reaction was quenched with water and the solution extracted with CH_2Cl_2 (3 x). The combined organic layers were dried over $MgSO_4$ and the mixture was concentrated under reduced pressure. The residue was purified by FC.

General procedure for Fmoc deprotection: GP2 [2]. To a solution of the Fmoc-protected amine (1.0 eq.) in CH_2Cl_2 (0.11 M) was added piperidine (15.9 eq.) and the reaction mixture was stirred for 1h at room temperature. The solution was concentrated and the residue was purified by flash FC.

General procedure for C9-O alkylation: GP3 [3]. To a solution of **MZ21** (1.0 eq.) in acetone (0.30 M) were added Cs_2CO_3 (1.5 eq.) and the required halide (10.1 mg, 0.0439 mmol, 2.0 eq.) and the reaction mixture was stirred at r.t. Conversion of starting material was monitiored by TLC. The reaction was quenched with water and the solution extracted with CH_2Cl_2. The combined organic layers were dried over $MgSO_4$ and the solvent was removed under reduced pressure. The crude product was purified by FC and HPLC.

(S)-1-Benzyl 2-methyl aziridine-1,2-dicarboxylate (**MZ5**) [4].

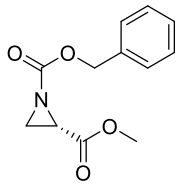

MZ5

Trifluoroacetic acid (9.47 ml, 0.124 mmol, 17.0 eq.) was added over a period of 10 min to a solution of (S)-methyl 1-trityl aziridine-2-carboxylate (2.50 g, 7.28 mmol, 1.0 eq.) in a mixture of chloroform (9.0 ml) and methanol (9.0 ml). The mixture was cooled to 0 °C and stirred for 4 h. The solvents were removed under reduced pressure at 0 °C; the last traces of trifluoroacetic acid were removed by azeotroping the residue with diethyl ether (3 x). The residue was partitioned between diethyl ether (10 ml) and water (10 ml). The organic layer was extracted with water (3 x) and the combined aqueous layers basified using $NaHCO_3$ (3.80 g). Ethyl acetate (95 ml) was added to the aqueous solution and the mixture was cooled to 0 °C. Benzyl chloroformate (1.06 ml, 7.50 mmol, 1.1 eq.) was added and the mixture was stirred vigorously under argon at room temperature for 20 h. The layers were separated and the aqueous layer was extracted with ethyl acetate (3 x). The combined organic layers were washed with brine (2 x) and dried over

$MgSO_4$. The solvent was concentrated under reduced pressure affording aziridine **MZ5** (1.64 g, 96%) as a light yellow oil that was used without further purification.

TLC: R_f = 0.77 (hexane/EtOAc 1/1). **$[\alpha]_D^{20}$: -**36.40 (c 0.7 in $CHCl_3$) **^{1}H-NMR** (400 MHz, $CDCl_3$): δ 7.36 (m, 5H), 5.15 (s, 2H), 3.71 (s, 3H), 3.11 (dd, *J* = 5.4, 3.2 Hz, 1H), 2.60 (dd, *J* = 3.2, 1.3 Hz, 1H), 2.48 (dd, *J* = 5.4, 1.3 Hz, 1H). **^{13}C-NMR** (400 MHz, $CDCl_3$): δ 168.5, 160.6, 135.3, 128.5, 128.4, 128.3, 68.5, 52.5, 34.7, 31.3. **IR** (film): $\tilde{\nu}$ = 3030, 2954, 1743, 1729, 1441, 1397, 1323, 1297, 1224, 1191, 1024, 752, 698. **HRMS** (ESI): *m*/*z* calcd for $C_{12}H_{14}NO_4$ $[M+H]^+$: 236.0917, found: 236.0921.

(1S,3S)-Methyl 1-*iso*-butyl-7-methoxy-2,3,4,9-tetrahydro-1H-pyrido[3,4-b]indole-3-carboxylate (**MZ4**) [5].

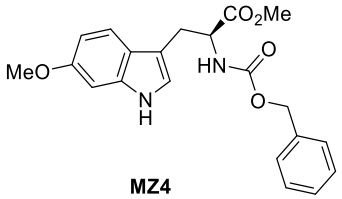

MZ4

(*S*)-1-Benzyl 2-methyl aziridine-1,2-dicarboxylate (**MZ5**) (7.10 g, 30.2 mmol 1.0 eq.) and 6-methoxyindole (8.88 g, 60.4 mmol, 2.0 eq) were dissolved in CH_2Cl_2 (100 ml) under argon and $Yb(OTf)_3$ (18.7 g, 30.2 mmol, 1.0 eq.) was added. The mixture was stirred at r.t. for 17 h. The reaction was quenched with water and mixture extracted with CH_2Cl_2 (3 x). The combined organic layers were dried over $MgSO_4$ and the solution was concentrated under vacuum. The crude product was purified by FC (hexane/EtOAc 9:1 to 4:1 to 2:1to 1:1) to provide tryptophan derivative **MZ4** (7.50 g, 65%) as a sticky, yellow oil.

TLC: R_f = 0.40 (hexane/EtOAc 1/1). **$[\alpha]_D^{20}$:** 38.40 (c 0.9 in $CHCl_3$). **^{1}H-NMR** (400 MHz, $CDCl_3$): δ 7.95 (bs, 1H); 7.34 (m, 5H), 6.84 (d, *J* = 2.3 Hz, 1H), 6.82 (d, *J* = 2.1 Hz, 1H), 6.75 (dd, *J* = 8.7, 2.2 Hz, 1H), 5.31 (d, *J* = 8.0 Hz, 1H), 5.10 (m, 2H), 4.70 (dt, *J* = 8.1, 5.4 Hz, 1H), 3.83 (s, 3H), 3.68 (s, 3H), 3.27 (d, *J* = 5.3 Hz, 2H). **^{13}C-NMR** (101 MHz, $CDCl_3$) δ 172.5, 156.6, 155.8, 137.9, 136.9, 136.3, 129.1, 128.5, 128.3, 128.2, 125.3, 121.6, 119.3, 109.8, 94.7, 66.9, 55.7, 54.5, 52.4, 28.0, 21.5. **IR** (film): $\tilde{\nu}$ = 3340, 2974, 2927, 2893, 1704, 1631, 1455, 1416, 1381, 1328, 1271, 1087, 879. **HRMS** (ESI): *m*/*z* calcd for $C_{21}H_{23}N_2O_5$ $[M+H]^+$: 383.1601, found: 383.1601.

(S)-Methyl 2-amino-3-(6-methoxy-1H-indol-3-yl)propanoate (**MZ6**) [5].

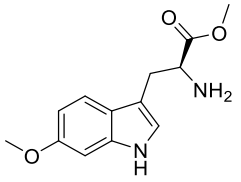

MZ6

Tryptophan **MZ4** (1.20 g, 3.14 mmol, 1.0 eq.) was dissolved in MeOH (65.0 ml) and Pd/C (10% w/w, 290 mg) was added under argon. The flask was flushed with hydrogen and stirred at r.t. for 3 h. After complete conversion of the starting material the hydrogen was replaced by argon and the mixture was filtered over celite. The solvent was removed under reduced pressure. FC (CH_2Cl_2 to CH_2Cl_2/MeOH 20/1) gave the free amine **MZ6** (554 mg, 71%) as a brown oil.
TLC: R_f = 0.17 (CH_2Cl_2/MeOH 20/1). **$[\alpha]_D^{20}$:** 18.20 (c 1.0 in $CHCl_3$). **^{1}H-NMR** (400 MHz, $CDCl_3$): δ 7.93 (bs, 1H); 7.48 (d, *J* = 8.7 Hz, 1H), 6.96 (d, *J* = 2.2 Hz, 1H), 6.85 (d, *J* = 2.2 Hz, 1H), 6.80 (dd, *J* = 8.7, 2.3, 1H), 3.84 (s, 3H), 3.81 (dd, *J* = 7.6, 4.9 Hz, 1H), 3.71 (s, 3H), 3.24 (ddd, *J* = 14.4, 4.8, 0.7 Hz, 1H), 3.02 (dd, *J* = 14.4, 7.3 Hz, 1H). **^{13}C-NMR** (400 MHz, $CDCl_3$): δ 175.9, 156.8, 137.2, 122.0, 121.8, 119.6, 111.3, 109.7, 94.8, 55.8, 55.1, 52.2, 30.9. **IR** (film): $\tilde{\nu}$ = 3383, 3015, 2954, 1730, 1628, 1453, 1300, 1263, 1209, 1160, 1027, 749, 666. **HRMS** (ESI): *m*/*z* calcd for $C_{13}H_{17}N_2O_3$ $[M+H]^+$: 249.1234, found: 249.1234.

(1S,3S)-Methyl 1-*iso*-butyl-7-methoxy-2,3,4,9-tetrahydro-1H-pyrido[3,4-b]indole-3-carboxylate (**MZ7-*cis* and MZ7-*trans***) [5].

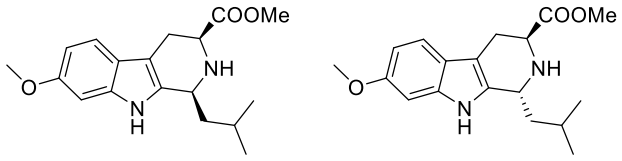

MZ7-*cis* **MZ7-*trans***

Amine **MZ6** (0.544 g, 2.19 mmol, 1.0 eq.) was dissolved in CH_2Cl_2 (13.6 ml) and isovaleraldehyde (0.236 ml, 2.19 mmol, 1.0 eq.) and trimethylorthoformate (0.885 ml, 8.09 mmol, 3.7 eq.) were added. The reaction mixture was stirred at room temperature for 20 h. The volatiles were then removed under reduced pressure and the residue was suspended in CH_2Cl_2 (13.6 ml) and cooled to -78 °C. TFA (0.228 ml, 2.96 mmol, 1.4 eq.) was added and the reaction mixture was allowed to warm to 0 °C over a period of 1.5 h. The mixture was carefully added to an ice-cold solution of $NaHCO_3$ (1.0 M, 23.0 ml), the phases were separated, and the aqueous layer was extracted with CH_2Cl_2 (3 x). The combined organic layers were dried over $MgSO_4$ and the solution was concentrated under reduced pressure. FC (hexane/EtOAc 9:1 to 4:1 to 2:1) afforded **MZ7-*cis*** (208 mg, 30%) **and MZ7-*trans*** (339 mg, 49%) as yellow foams.

MZ7-*cis*

TLC: R_f = 0.28 (hexane/EtOAc 2/1**). M.p:** 150.5-152.5 °C**. [α]$_D^{20}$:** -100.8 (c 1.1 in $CHCl_3$). **^{1}H-NMR** (400 MHz, $CDCl_3$): δ 7.65 (bs, 1H); 7.34 (d, *J* = 8.6 Hz, 1H), 6.84 (d, *J* = 2.1 Hz, 1H), 6.77 (dd, *J* = 8.6, 2.2 Hz, 1H), 4.19 (m, 1H), 3.83 (s, 3H), 3.82 (s, 3H), 3.08 (ddd, *J* = 15.1, 4.2, 1.9 Hz, 1H), 2.78 (ddd, *J* = 15.0, 11.2, 2.7 Hz, 1H), 2.02 (m, 2H), 1.64 (m, 2H), 1.03 (d, *J* = 6.5 Hz, 3H), 1.00 (d, *J* = 6.6 Hz, 3H). **^{13}C-NMR** (400 MHz, $CDCl_3$): δ 174.0, 156.4, 136.8, 135.0, 121.9, 118.6, 109.1, 107.8, 95.2, 56.6, 55.9, 52.3, 50.7, 44.7, 26.2, 24.5, 24.0, 22.0. **IR** (film): $\tilde{\nu}$ = 2958, 1734, 1433, 1214, 750, 669. **HRMS** (ESI): *m*/*z* calcd for $C_{18}H_{25}N_2O_3$ $[M+H]^+$: 317.1860, found: 317.1864.

MZ7-*trans*

TLC: R_f = 0.17 (hexane/EtOAc 2/1)**. M.p:** 149.0-150.9 °C**. [α]$_D^{20}$:** 14 (c 1.0 in $CHCl_3$). **^{1}H-NMR** (400 MHz, $CDCl_3$) δ 7.79 (s, 1H), 7.36 (d, *J* = 8.5 Hz, 1H), 6.82 (d, *J* = 1.9 Hz, 1H), 6.79 (dd, *J* = 8.5, 2.2 Hz, 1H), 4.27 (dd, *J* = 9.9, 4.0 Hz, 1H), 3.98 (dd, *J* = 7.5, 5.2 Hz, 1H), 3.83 (s, 3H), 3.78 (s, 3H), 3.10 (ddd, *J* = 15.3, 5.2, 0.9 Hz, 1H), 2.96 (ddd, *J* = 15.3, 7.5, 1.4 Hz, 1H), 2.18 (s, 1H), 2.08 – 1.88 (m, 1H), 1.72 (ddd, *J* = 14.6, 9.9, 4.8 Hz, 1H), 1.52 (ddd, *J* = 13.7, 9.4, 4.2 Hz, 1H), 1.04 (d, *J* = 6.6 Hz, 3H), 1.02 (d, *J* = 6.6 Hz, 3H). **^{13}C-NMR** (101 MHz, $CDCl_3$) δ 174.4, 156.3, 136.7, 134.9, 121.8, 118.6, 109.0, 108.8, 106.7, 95.2, 55.9, 52.5, 52.2, 48.3, 44.6, 25.2, 24.8, 23.8, 21.8. **IR** (film): $\tilde{\nu}$ = 3376, 2954, 2921, 2869, 2837, 1731, 1631, 1499, 1466, 1437, 1366, 1340, 1289, 1263, 1199, 1153, 1033, 908, 807, 793, 729, 668, 647. **HRMS** (ESI): *m*/*z* calcd for $C_{18}H_{25}N_2O_3$ $[M+H]^+$: 317.1860, found: 317.1863.

(1S,3S)-Methyl 2-((R)-2-((((9H-fluoren-9-yl)methoxy)carbonyl)amino)-6-((*tert*-butoxycarbonyl)amino)hexanoyl)-1-*iso*-butyl-7-methoxy-2,3,4,9-tetrahydro-1H-pyrido[3,4-b]indole-3-carboxylate (**MZ1**).

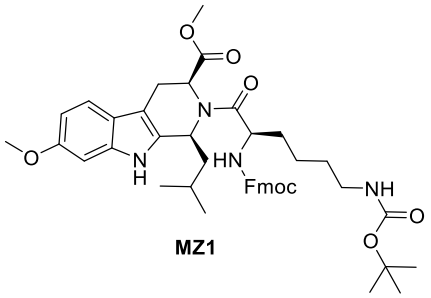

MZ1

Following the general procedure GP1 **MZ7-*cis*** was reacted with Fmoc-Lys(Boc)-OH. Amide **MZ1** was isolated after purification by FC (hexane/EtOAc 9/1 to 4/1 to 2/1 to 1/1) as a light yellow solid (86 mg, 89%). Due to the presence of rotational isomers the NMR-spectra of **MZ1** were highly complex and no efforts were spent on the detailed interpretation of the spectral data obtained for this intermediate.

TLC: R_f = 0.20 (hexane/EtOAc 2/1). **HRMS** (ESI): *m*/*z* calcd for $C_{44}H_{55}N_4O_8$ $[M+H]^+$: 767.4014, found: 767.4008.

***Tert*-butyl (4-((3S,6S,12aS)-6-*iso*-butyl-9-methoxy-1,4-dioxo-1,2,3,4,6,7,12,12a-octahydropyrazino[1',2':1,6]pyrido[3,4-b]indol-3-yl)butyl)carbamate** (**MZ15**).

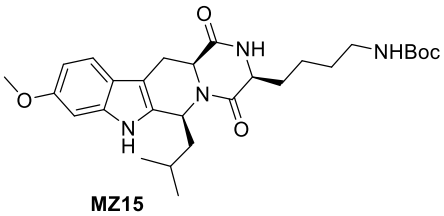

MZ15

Following the general procedure GP2, compound **MZ15** was isolated after purification by FC (hexane/EtOAc 1/5) as a white solid (26 mg, 86%).

TLC: R_f = 0.19 (hexane/EtOAc 1/4). **$[\alpha]_D^{20}$:** -38.00 (c 0.40 in MeOH). **^{1}H-NMR** (400 MHz, $CDCl_3$): δ 7.89 (bs, 1H); 7.43 (d, *J* = 8.6 Hz, 1H), 6.89 (d, *J* = 2.1 Hz, 1H), 6.83 (dd, *J* = 8.6, 2.2 Hz, 1H), 6.53 (bs, 1H), 5.45 (dd, *J* = 9.2, 4.1 Hz, 1H), 4.68 (bs, 1H), 4.04 (dd, *J* = 11.5, 4.7 Hz, 1H), 3.95 (m, 1H), 3.85 (s, 3H), 3.53 (dd, *J* = 15.8, 4.9 Hz, 1H), 3.19 (d, *J* = 4.2 Hz, 1H), 3.03 (dd, *J* = 15.7, 11.7 Hz, 1H), 2.13 (m, 1H), 1.95 (m, 1H), 1.74 (ddd, *J* = 14.4, 10.1, 4.4 Hz, 1H), 1.56 (m, 5H), 1.47 (s, 9H), 1.05 (d, *J* = 6.5 Hz, 3H), 0.83 (d, *J* = 6.3 Hz, 3H). **^{13}C-NMR** (101 MHz, $CDCl_3$) δ 169.9, 168.9, 156.6, 136.7, 133.2, 120.8, 118.9, 109.8, 106.9, 95.3, 56.1, 55.9, 54.2, 51.2, 46.1, 39.4, 30.1, 29.3, 28.6, 25.0, 24.0, 22.0, 21.8, 21.4.
IR (film): $\tilde{\nu}$ = 3293, 2955 2931, 2867, 1687, 1632, 1506, 1449, 1392, 1366, 1329, 1298, 1276, 1250, 1198, 1158, 907, 731. **HRMS** (ESI): *m*/*z* calcd for $C_{28}H_{41}N_4O_5$ $[M+H]^+$: 513.3071, found: 513.3067.

(3S,6S,12aS)-3-(4-aminobutyl)-6-*iso*-butyl-9-methoxy-2,3,12,12a-tetrahydropyrazino[1',2':1,6]pyrido[3,4-b]indole-1,4(6H,7H)-dione (**MZ16**) [6].

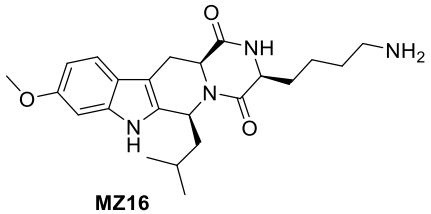

MZ16

To a solution of **MZ15** (17.5 mg, 0.0341 mmol, 1.0 eq.) in CH_2Cl_2 (900 µl) was added TFA (86.8 µl) and the reaction mixture was stirred for 1.5 h at room temperature. The mixture was carefully added to an aqueous Na_2CO_3 (1M, 1 ml) solution and extracted with CH_2Cl_2 (3 x). The combined organic layers were dried over $MgSO_4$ and the solvent was removed under reduced pressure. The crude was purified by HPLC obtaining **MZ16** (4.60 mg, 33%) as a light yellow sticky solid.

TLC: R_f = 0.45 ($CHCl_3$/MeOH/H_2O 65/44/12). **$[\alpha]_D^{20}$:** -24.00 (c 0.25 in MeOH). **^{1}H-NMR** (400 MHz, DMSO-d_6): δ 10.91 (bs, 1H); 8.29 (s, 1H), 7.78 (bs, 2H), 7.40 (d, *J* = 8.6 Hz, 1H), 6.87 (d, *J* = 2.2 Hz, 1H), 6.66 (dd, *J* = 8.6, 2.3 Hz, 1H), 5.33 (dd, *J* = 8.1, 4.5 Hz, 1H), 4.14 (dd, *J* = 11.6, 4.7 Hz, 1H), 4.01 (t, *J* = 4.8 Hz, 1H), 3.76 (s, 3H), 3.31 (dd, 15.8, 5.1 Hz, 1H), 2.79 (dd, *J* = 15.1, 5.9 Hz, 3H), 1.83 (m, 1H), 1.75 (m, 1H), 1.56 (m, 4H), 1.42 (m, 3H), 0.90 (d, *J* = 6.5 Hz, 3H), 0.76 (d, *J* = 6.6 Hz, 3H). **^{13}C-NMR** (500 MHz, DMSO-d_6): δ 169.8, 169.0, 155.4, 136.6, 133.5, 120.3, 118.4, 108.7, 105.2, 94.8, 55.2, 53.1, 50.1, 45.7, 38.6, 28.8, 26.9, 24.1, 23.9, 22.1, 21.5, 21.1. **IR** (film): $\tilde{\nu}$ = 3319, 2943, 2829, 2361, 1407, 1019, 647. **HRMS** (ESI): *m*/*z* calcd for $C_{23}H_{33}N_4O_3$ $[M+H]^+$: 413.2547, found: 413.2545. **RP-HPLC:** column: SymmetryPrep^{TM} C18, 5µm, 19 x 100 mm, gradient: ACN + 0.1% TFA/H_2O 20/80 to 30/70, 1 ml/min, 254 nm, R_t = 11.65 min.

(1S,3S)-Methyl 2-((R)-2-((((9H-fluoren-9-yl)methoxy)carbonyl)amino)-5-(*tert*-butoxy)-5-oxopentanoyl)-1-*iso*-butyl-7-methoxy-2,3,4,9-tetrahydro-1H-pyrido[3,4-b]indole-3-carboxylate (**MZ10**).

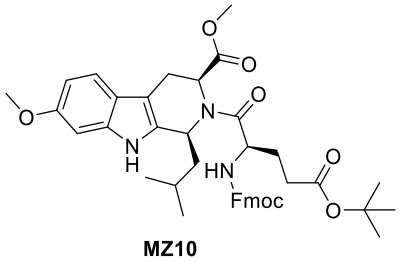

MZ10

Following the general procedure GP1 **M7-*cis*** was reacted with Fmoc-Glu(O*t*-Bu)-OH. Amide **MZ10** was isolated after purification by FC (toluene/EtOAc 15/1) as a light yellow solid (771 mg, 28%). Due to the presence of rotational isomers the NMR-spectra of **MZ10** were highly complex and no efforts were spent on the detailed interpretation of the spectral data obtained for this intermediate.
TLC: R_f = 0.36 (hexane/EtOAc 2/1).

***Tert*-butyl 3-((3S,6S,12aS)-6-*iso*-butyl-9-methoxy-1,4-dioxo-1,2,3,4,6,7,12,12a-octahydropyrazino[1',2':1,6]pyrido[3,4-b]indol-3-yl)propanoate** (**MZ30**).

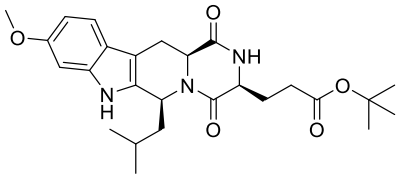

MZ30
(Ko143)

Following the general procedure GP2, compound **MZ30** (**Ko143**) was isolated after purification by FC (hexane/EtOAc 1/1) as a white solid (399 mg, 85%).
TLC: R_f = 0.60 (hexane/EtOAc 1/4). **M.p**: 124.5-131.2 °C. **$[\alpha]_D^{20}$:** -114.99 (c 0.2 in $CHCl_3$). **^{1}H-NMR** (400 MHz, $CDCl_3$): δ 7.88 (bs, 1H), 7.43 (d, *J* = 8.6 Hz, 1H), 6.89 (d, 2.1 Hz, 1H), 6.83 (dd, 8.6, 2.2 Hz, 1H), 6.79 (bs, 1H), 5.45 (dd, *J* = 9.2, 4.1 Hz, 1H), 4.02 (dt, *J* = 9.5, 4.7 Hz, 2H), 3.85 (s, 3H), 3.53 (dd, *J* = 15.8, 4.9 Hz, 1H), 3.03 (dd, *J* = 15.8, 11.7 Hz, 1H), 2.50 (t, *J* = 6.5 Hz, 2H), 2.37 (m, 1H), 2.21 (m, 1H), 1.75 (ddd, *J* = 14.5, 10.1, 4.6 Hz, 1H), 1.56 (m, 2H), 1.47 (s, 9H), 1.05 (d, *J* = 6.5 Hz, 3H), 0.84 (d, *J* = 6.4 Hz, 3H). **^{13}C-NMR** (101 MHz, $CDCl_3$) δ 173.4, 169.9, 168.5, 156.6, 136.7, 133.2, 120.8, 118.9, 109.8, 106.8, 95.3, 81.5, 56.0, 55.9, 54.3, 51.3, 46.0, 31.5, 28.2, 21.98, 21.8. **IR** (film): $\tilde{\nu}$= 3296, 2939, 2357, 1688, 1445, 1388, 1327, 1251, 1156, 768, 666. **HRMS** (ESI): *m*/*z* calcd for $C_{26}H_{35}N_3NaO_5$ $[M+Na]^+$ 492.2469, found: 492.2462.

3-((3S,6S,12aS)-6-*iso*-butyl-9-methoxy-1,4-dioxo-1,2,3,4,6,7,12,12a-octahydropyrazino[1',2':1,6]pyrido[3,4-b]indol-3-yl)propanoic acid (**MZ35**) [7].

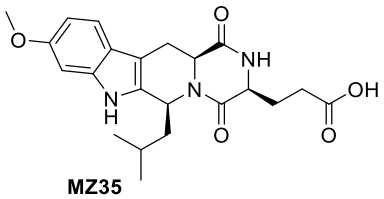

MZ35

To a solution of **MZ30** (30.0 mg, 0.0639 mmol, 1.0 eq.) in CH_2Cl_2 (1.7 ml) was added TFA (160 µl) and the reaction was stirred for 6 h at room temperature. The reaction was quenched with water (2 ml) and the mixture extracted with CH_2Cl_2 (3 x). The combined organic layers were dried over $MgSO_4$ and the solvent removed under reduced pressure. Purification by FC (CH_2Cl_2/MeOH 5 to 20%) afforded the desired product **MZ35** (23.0 mg, 87%) as a colorless oil.

TLC: R_f = 0.47 ($CHCl_3$/MeOH/H_2O 85/13/1.5). **$[\alpha]_D^{20}$:** -29.31 (c 0.58 in MeOH). **^{1}H-NMR** (400 MHz, DMSO-d_6): δ 10.96 (s, 1H), 8.82 (bs, 1H), 7.39 (d, *J* = 8.6 Hz, 1H), 6.86 (d, *J* = 2.2 Hz, 1H), 6.65 (dd, *J* = 8.6, 2.2 Hz, 1H), 5.32 (dd, *J* = 7.9, 4.8 Hz, 1H), 4.10 (dd, *J* = 11.4, 4.9 Hz, 1H), 4.01 (m, 1H), 3.75 (s, 3H), 3.29 (d, *J* = 4.8 Hz, 1H), 2.78 (dd, *J* = 15.6, 11.6 Hz, 1H), 2.18 (m, 3H), 1.90 (m, 1H), 1.55 (m, 1H), 1.44 (m, 1H), 0.91 (d, *J* = 6.4 Hz, 3H), 0.76 (d, *J* = 6.5 Hz, 3H). **^{13}C-NMR** (400 MHz, DMSO-d_6): δ 169.6, 169.3, 155.3, 136.5, 133.6, 120.3, 118.3, 108.7, 105.1, 94.8, 55.2, 55.1, 53.8, 50.0, 45.8, 25.3, 24.2, 23.8, 22.2, 21.4. **IR** (film): $\tilde{\nu}$ = 3323, 2947, 2829, 1650, 1407, 1015. **HRMS** (ESI): *m*/*z* calcd for $C_{22}H_{28}N_3O_5$ $[M+H]^+$: 414.2023, found: 414.2020.

3-((3S,6S,12aS)-6-*iso*-butyl-9-methoxy-1,4-dioxo-1,2,3,4,6,7,12,12a-octahydropyrazino[1',2':1,6]pyrido[3,4-b]indol-3-yl)-N-(2-((7-nitrobenzo[c][1,2,5]oxadiazol-4-yl)amino)ethyl)propanamide (FKo143) [8].

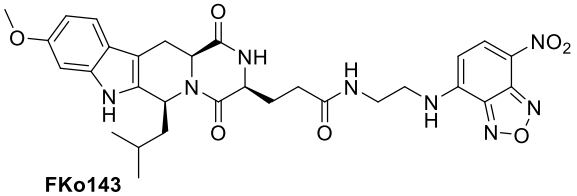

FKo143

Ko143 (6.5 mg, 0.0138 mmol, 1eq.) was dissolved in CH_2Cl_2 (1 ml) and TFA (0.05 ml, 0.653 mmol, 47 eq.) was added. The mixture was stirred at r.t. for 3.5 h. The volatiles were removed under reduced pressure. The crude carboxylic acid was obtained as a pale brown solid and was used in the next step without further purification. The crude carboxylic acid was dissolved in dry DMF (1 ml) and EDC (2.58 mg, 0.0166 mmol, 1.2 eq.) and HOBt (10.0 mg, 0.0653 mmol, 4.7 eq.) were added. After 5 min the amine (9.00 mg, 0.040 mmol, 2.9 eq) was added followed by addition of Et_3N (0.0400 ml, 0.287 mmol, 20 eq.). The mixture was stirred at r.t. for 16 h. The solvent was removed under reduced pressure. The crude material was purified by FC (CH_2Cl_2/MeOH 40:1 to 20:1 to 9:1) obtaining amide **FKo143** (2.90 mg, 34%) as an orange solid.

TLC: Rf = 0.23 (CH_2Cl_2/MeOH 19:1). **$[\alpha]_D^{20}$:** -21.9 (*c* = 0.33 in MeOH). **^{1}H-NMR** (500 MHz, DMSO-*d*$_6$): δ 10.89 (s, 1H), 9.43 (bs, 1H), 8.52 (d, *J* = 8.8 Hz, 1H), 8.33 (s, 1H), 8.09 (t, *J* = 5.7 Hz, 1H), 7.40 (d, *J* = 8.6 Hz, 1H), 6.86 (d, *J* = 2.2 Hz, 1H), 6.66 (dd, *J* = 8.6, 2.2 Hz, 1H), 6.43 (d, *J* = 9.0 Hz, 1H), 5.31 (dd, *J* = 8.4, 4.4 Hz, 1H), 4.13 (dd, *J* = 11.6, 4.8 Hz, 1H), 4.02 (t, *J* = 5.0 Hz, 1H), 3.75 (s, 3H), 3.55 (bs, 2H), 3.42 – 3.43 (m, 2H), 3.30 (dd, *J* = 15.6, 5.0 Hz, 1H), 2.77 (dd, *J* = 15.5, 11.7 Hz, 1H), 2.34 – 2.18 (m, 2H), 2.11 – 2.01 (m, 1H), 2.01 – 1.91 (m, 1H), 1.60 – 1.47 (m, 2H), 1.46 – 1.40 (m, 1H), 0.91 (d, *J* = 6.5 Hz, 3H), 0.74 (d, *J* = 6.5 Hz, 3H). **^{13}C-NMR** (126 MHz, DMSO-*d*$_6$): δ 172.5, 169.8, 168.9, 155.4, 145.4, 144.5, 144.1, 138.0, 136.5, 133.5, 120.9, 120.3, 118.4, 108.7, 105.2, 99.2, 94.8, 55.2, 55.1, 52.8, 50.1, 45.7, 43.1, 37.4, 30.8, 25.2, 24.2, 23.8, 22.1, 21.4. **IR** (film): = 3373, 3262, 2954, 2924, 1653, 1582, 1296, 1261, 1234, 1024, 998 cm^{-1}. **HRMS** (ESI): *m*/*z* calcd for $C_{30}H_{35}N_8O_7$ $[M+H]^+$: 619.2623, found: 619.2612.

(3S,6R,12aS)-3-(4-aminobutyl)-6-*iso*-butyl-9-methoxy-2,3,12,12a-tetrahydropyrazino[1',2':1,6]pyrido[3,4-b]indole-1,4(6H,7H)-dione (**MZ40**) [6].

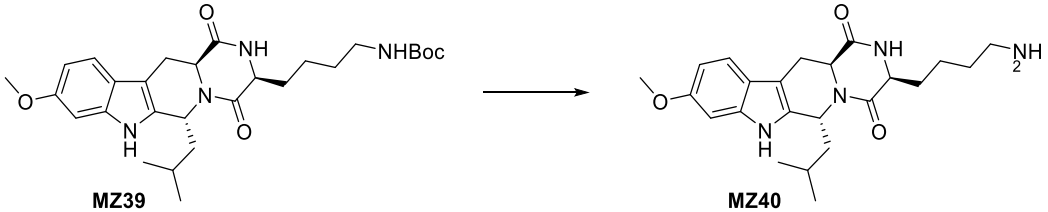

MZ39 MZ40

Following the general procedure GP1 **MZ7-*trans*** was reacted with Fmoc-Lys(Boc)-OH obtaining the amide which was directly used without further purification
Following the general procedure GP2, this intermediate was converted into **MZ39**; however, the latter could not be obtained in pure form (even after FC) and was used as such in next step.
To a solution of **MZ39** (18.0 mg, 0.0351 mmol, 1.0 eq.) in CH_2Cl_2 (1.0 ml) was added TFA (89.3 µl) and the reaction was stirred for 1.5 h at room temperature. The mixture was carefully added to an aqueous Na_2CO_3 (1M, 1 ml) solution and extracted with CH_2Cl_2. (3 x). The combined organic layers were dried over $MgSO_4$ and the mixture was concentrated under reduced pressure. The crude material was purified by HPLC obtaining **MZ40** (3.00 mg, 21%) as a light yellow oil.

TLC: R_f = 0.45 ($CHCl_3$/MeOH/H_2O 65/44/12). **$[\alpha]_D^{20}$:** +6.25 (c 0.8 in MeOH). **^{1}H-NMR** (400 MHz, DMSO-d_6) δ 10.82 (s, 1H), 8.49 (s, 1H), 7.57 (s, 3H), 7.29 (d, *J* = 8.6 Hz, 1H), 6.82 (d, *J* = 2.2 Hz, 1H), 6.64 (dd, *J* = 8.6, 2.3 Hz, 1H), 5.70 (d, *J* = 9.1 Hz, 1H), 4.34 – 4.25 (m, 1H), 4.00 (s, 1H), 3.75 (s, 3H), 3.21 – 3.13 (m, 1H), 2.72 (s, 3H), 2.67 (s, 1H), 1.81 (d, *J* = 10.5 Hz, 1H), 1.69 (d, *J* = 6.2 Hz, 2H), 1.60 (d, *J* = 10.1 Hz, 2H), 1.53 – 1.44 (m, 2H), 1.04 (d, *J* = 5.9 Hz, 3H), 0.91 (d, *J* = 6.2 Hz, 4H). **^{13}C-NMR**: too little material. **IR** (film): $\tilde{\nu}$ = 3315, 2943, 2829, 2357, 1407, 1019, 647. **HRMS** (ESI): *m*/*z* calcd for $C_{23}H_{33}N_4O_3$ $[M+H]^+$: 413.2547, found: 413.2546. **RP-HPLC:** column: SymmetryPrep™ C18, 5µm, 19 x 100 mm, gradient: ACN + 0.1% TFA/H_2O 20/80 to 30/70, 1 ml/min, 254 nm, R_t = 8.55 min.

(1S,3S)-Methyl 2-((R)-2-((((9H-fluoren-9-yl)methoxy)carbonyl)amino)-4-(*tert*-butoxy)-4-oxobutanoyl)-1-*iso*-butyl-7-methoxy-2,3,4,9-tetrahydro-1H-pyrido[3,4-b]indole-3-carboxylate (**MZ84**).

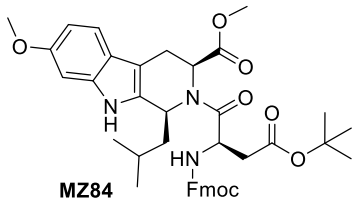

MZ84

Following the general procedure GP1, **MZ7-*cis*** was reacted with Fmoc-Asp(O*t*Bu)-OH. Amide **MZ84** was isolated after purification by FC (hexane/EtOAc 4/1) as light yellow oil (21.6 mg, 63%). Due to the presence of rotational isomers the NMR-spectra of **MZ84** were highly complex and no efforts were spent on the detailed interpretation of the spectral data obtained for this intermediate.
TLC: R_f = 0.75 (hexane/EtOAc 1/1). **HRMS** (ESI): *m*/*z* calcd for $C_{26}H_{35}N_3NaO_5$ $[M+H]^+$: 710.3436, found: 710.3428

***Tert*-butyl 2-((3S,6S,12aS)-6-*iso*-butyl-9-methoxy-1,4-dioxo-1,2,3,4,6,7,12,12a-octahydropyrazino[1',2':1,6]pyrido[3,4-b]indol-3-yl)acetate** (**MZ90**).

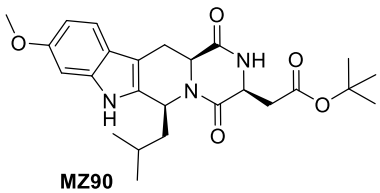

MZ90

Following the general procedure GP2, compound **MZ90** was isolated after purification by FC (hexane/EtOAc 1/1) as a light yellow solid (8.8 mg, 64%).
TLC: R_f = 0.19 (hexane/EtOAc 1/1). **M.p**: not enough material. **$[\alpha]_D^{20}$**: -99.06 (c 1.08 in $CHCl_3$). **^{1}H-NMR** (400 MHz, $CDCl_3$) δ 7.80 (s, 1H), 7.36 (d, *J* = 8.6 Hz, 1H), 6.82 (d, *J* = 2.1 Hz, 1H), 6.76 (dd, *J* = 8.6, 2.2 Hz, 1H), 6.57 (s, 1H), 5.36 (dd, *J* = 9.1, 4.0 Hz, 1H), 4.23 (dd, *J* = 9.9, 2.9 Hz, 1H), 4.00 (dd, *J* = 11.6, 4.5 Hz, 1H), 3.78 (s, 3H), 3.50 (dd, *J* = 15.8, 4.7 Hz, 1H), 3.19 (dd, *J* = 17.2, 3.5 Hz, 1H), 2.93 (dd, *J* = 15.7, 11.7 Hz, 1H), 2.55 (dd, *J* = 17.2, 10.0 Hz, 1H), 1.74 – 1.65 (m, 1H), 1.51 – 1.46 (m, 2H), 1.42 (s, 9H), 0.97 (d, *J* = 6.5 Hz, 3H), 0.75 (d, *J* = 6.4 Hz, 3H). **^{13}C-NMR** (101 MHz, $CDCl_3$) δ 170.4, 169.1, 167.4, 156.6, 136.5, 132.8, 120.6, 118.8, 109.8, 106.9, 95.2, 82.3, 56.0, 55.8, 51.4, 45.7, 37.2, 28.1, 24.8, 23.9, 22.2, 21.7. **IR** (film): $\tilde{\nu}$= 3319, 2956, 2930, 1730, 1688, 1660, 1630, 1469, 1446, 1391, 1367, 1295, 1259, 1199, 1154, 1040, 1024, 810, 736. **HRMS** (ESI): *m*/*z* calcd for $C_{25}H_{33}N_3NaO_5$ $[M+Na]^+$: 478.2312, found: 478.2306.

Methyl (1S,3S)-2-((((9H-fluoren-9-yl)methoxy)carbonyl)-D-prolyl)-1-*iso*-butyl-7-methoxy-2,3,4,9-tetrahydro-1H-pyrido[3,4-b]indole-3-carboxylate (**MZ147**).

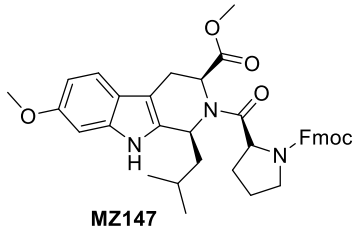

MZ147

Following the general procedure GP1 **MZ7-*cis*** was reacted with Fmoc-Pro-OH. Amide **MZ147** was isolated after purification by FC (hexane/EtOAc 2/1) as light yellow oil (12.0 mg, 41%). Due to the presence of rotational isomers the NMR-spectra of **MZ147** were highly complex and no efforts were spent on the detailed interpretation of the spectral data obtained for this intermediate.

TLC: R_f = 0.16 (hexane/EtOAc 1/1). **HRMS** (ESI): *m*/*z* calcd for $C_{38}H_{42}N_3O_6$ $[M+H]^+$: 636.3068, found: 636.3062.

(5aS,12S,14aS)-12-*iso*-butyl-9-methoxy-1,2,3,5a,6,11,12,14a-octahydro-5H,14H-pyrrolo[1'',2'':4',5']pyrazino[1',2':1,6]pyrido[3,4-b]indole-5,14-dione (**MZ148**).

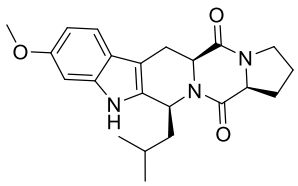

MZ148

Following the general procedure GP2, compound **MZ148** was isolated after purification by FC (hexane/EtOAc 1/2) as a light yellow oil (4.68 mg, 65%).
TLC: R_f = 0.16 (hexane/EtOAc 1/2**). [α]$_D^{20}$:** -32.97 (c 0.94 in MeOH). **^{1}H-NMR** (400 MHz, $CDCl_3$): δ 7.65 (bs, 1H); 7.34 (d, *J* = 8.6 Hz, 1H), 6.84 (d, *J* = 2.1 Hz, 1H), 6.77 (dd, *J* = 8.6, 2.2 Hz, 1H), 4.19 (m, 1H), 3.83 (s, 3H), 3.82 (s, 3H), 3.08 (ddd, *J* = 15.1, 4.2, 1.9 Hz, 1H), 2.78 (ddd, *J* = 15.0, 11.2, 2.7 Hz, 1H), 2.02 (m, 2H), 1.64 (m, 2H), 1.03 (d, *J* = 6.5 Hz, 3H), 1.00 (d, *J* = 6.6 Hz, 3H). **^{13}C-NMR** too little material. **IR** (film): $\tilde{\nu}$ = 3312, 2944, 2832, 1473, 1456, 1417, 1406, 1220, 1022, 772, 670. **HRMS** (ESI): *m*/*z* calcd for $C_{22}H_{28}N_3O_3$ $[M+H]^+$: 382.2125, found: 382.2126.

6-((*Tert*-butyldimethylsilyl)oxy)-1H-indole (**MZ8**) [9].

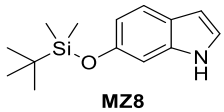

MZ8

To a solution of commercially available 6-hydroxy indole (4.00 g, 30.0 mmol, 1.0 eq.) in DMF (17.0 ml) were added TBSCl (5.43 g, 36.1 mmol, 1.2 eq.) and imidazole (5.11 g, 75.1 mmol, 2.5 eq.). The reaction mixture was stirred for 20 h. The reaction mixture was diluted with EtOAc (30 ml) and water (20 ml). The two phases were separated and the organic phase was washed with water (4 x). The organic layer was dried over $MgSO_4$ and the solvent was removed under reduced pressure. The crude product was purified with FC (hexane/EtOAc 12/1) affording the desired product **MZ8** (4.64 g, 62%) as a light brown solid.

TLC: R_f = 0.56 (hexane/EtOAc 4/1). **M.p**: 56.5-58.1 °C. **^{1}H-NMR** (400 MHz, $CDCl_3$): δ 7.95 (bs, 1H), 7.46 (d, *J* = 8.5 Hz, 1H), 7.09 (dd, *J* = 3.2, 2.4 Hz, 1H), 6.85 (dd, *J* = 1.3, 0.7 Hz, 1H), 6.70 (dd, *J* = 8.5, 2.1 Hz, 1H), 6.48 (ddd, *J* = 3.1, 2.0, 0.9 Hz, 1H), 1.01 (s, 9H), 0.21 (s, 6H).**^{13}C-NMR** (400 MHz, $CDCl_3$): δ 151.9, 123.3, 122.8, 121.0, 120.1, 114.6, 102.6, 101.7, 25.9, 18.4, -4.2. **IR** (film): $\tilde{\nu}$ = 3413, 2930, 2857, 1623, 1509, 1496, 1462, 1394, 1339, 1298, 1250, 1214, 1164, 1088, 965, 876,

839, 803, 779. **HRMS** (ESI): *m*/*z* calcd for $C_{14}H_{22}NOSi$ $[M+H]^+$: 248.1465, found: 248.1465.

(S)-Methyl 2-(((benzyloxy)carbonyl)amino)-3-(6-((*tert*-butyldimethylsilyl)oxy)-1H-indol-3-yl)propanoate (**MZ11**) [5].

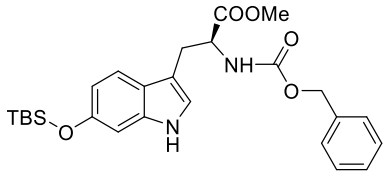

MZ11

(*S*)-1-Benzyl 2-methyl aziridine-1,2-dicarboxylate (**MZ5**) (3.85 g, 16.4 mmol 1.0 eq.) and indole **MZ8** (8.10 g, 32.7 mmol, 2.0 eq) were dissolved in CH_2Cl_2 (63 ml) and $Yb(OTf)_3$ (10.2 g, 16.4 mmol, 1.0 eq.) was added. The mixture was stirred at r.t. for 17 h. The reaction was quenched with water and the mixture extracted with CH_2Cl_2 (3 x). The combined organic layers were dried over $MgSO_4$ and the solvent was removed under reduces pressure. The mixture was purified by FC (hexane/EtOAc 9:1 to 4:1 to 2:1) obtain **MZ11** (3.87 g, 49%) as a sticky yellow oil.

TLC: R_f = 0.49 (hexane/EtOAc 2/1). **$[\alpha]_D^{20}$**: +29.50 (c 1.0 in $CHCl_3$). **^{1}H-NMR** (400 MHz, $CDCl_3$): δ 7.91 (bs, 1H); 7.33 (m, 5H), 7.31 (d, *J* = 1.1 Hz, 1H), 6.84 (d, *J* = 2.3 Hz, 1H), 6.79 (d, *J* = 2.0 Hz, 1H), 6.66 (dd, *J* = 8.5, 2.1 Hz, 1H), 5.33 (d, *J* = 8.1 Hz, 1H), 5.12 (m, 2H), 4.70 (dt, *J* = 8.1, 5.4 Hz, 1H), 3.67 (s, 3H), 3.26 (d, *J* = 5.3 Hz, 1H), 1.01 (s, 9H), 0.20 (s, 6H). **^{13}C-NMR** (101 MHz, $CDCl_3$) δ 172.6, 155.9, 152.1, 137.1, 136.5, 128.7, 128.3, 122.6, 121.9, 120.1, 119.0, 114.4, 109.9, 101.9, 77.5, 77.2, 76.8, 67.0, 54.6, 52.5, 28.1, 25.9, 18.4, -4.3, -4.3. **HRMS** (ESI): *m*/*z* calcd for $C_{26}H_{35}N_2O_5Si$ $[M+H]^+$: 483.2310, found: 483.2306.

(S)-Methyl 2-amino-3-(6-((*tert*-butyldimethylsilyl)oxy)-1H-indol-3-yl)propanoate (**MZ14**) [5].

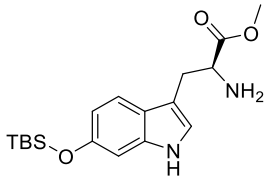

MZ14

Tryptophan **MZ11** (4.56 g, 9.45 mmol, 1.0 eq) was dissolved in MeOH (180 ml) and Pd/C (10% w/w, 872 mg) was added under argon. The flask was flushed with hydrogen and stirred at r.t. for 6 h. After complete conversion of the starting material the hydrogen was replaced by argon and the mixture was filtered over

celite. The solvent was removed under reduced pressure and the crude product was purified by FC (CH_2Cl_2/MeOH 20/1) affording the pure amine **MZ14** (2.80 g, 85%) as a brown oil.

TLC: R_f = 0.42 (CH_2Cl_2/MeOH 20/1). **[α]$_D^{20}$**: +6.8 (c 1.0 in $CHCl_3$). **^{1}H-NMR** (400 MHz, $CDCl_3$): δ 7.94 (bs, 1H); 7.41 (d, *J* = 8.5 Hz, 1H), 6.94 (s, 1H), 6.80 (d, *J* = 2.1 Hz, 1H), 6.69 (dd, *J* = 8.5, 2.1, 1H), 3.81 (m, 1H), 3.70 (s, 3H), 3.23 (ddd, *J* = 14.4, 4.8, 0.7 Hz, 1H), 3.01 (dd, *J* = 14.4, 7.7 Hz, 1H), 1.00 (s, 9H), 0.20 (s, 6H). **^{13}C-NMR** (400 MHz, $CDCl_3$): δ 175.8, 152.0, 137.1, 122.5, 121.8, 119.1, 114.1, 111.2, 101.8, 55.0, 52.0, 30.9, 25.8, 18.3, -4.4. **IR** (film): $\tilde{\nu}$ = 2947, 2354, 1738, 1255, 1214, 749, 668. **HRMS** (ESI): *m*/*z* calcd for $C_{18}H_{29}N_2O_3Si$ $[M+H]^+$: 349.1942, found: 349.1940.

(1S,3S)-Methyl 7-((*tert*-butyldimethylsilyl)oxy)-1-*iso*-butyl-2,3,4,9-tetrahydro-1H-pyrido[3,4-b]indole-3-carboxylate (**MZ17 cis**) [5].

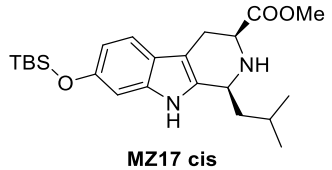

MZ17 cis

The free amine **MZ14** (2.87 g, 8.24 mmol, 1.0 eq.) was dissolved in CH_2Cl_2 (50 ml) and isovaleraldehyde (887 µl, 8.24 mmol, 1.0 eq.) and trimethylorthoformate (3.32 ml, 30.4 mmol, 3.7 eq.) were added. The reaction mixture was stirred at room temperature for 20 h. The volatiles were removed under reduced pressure. The residue was suspended in CH_2Cl_2 (50 ml) and cooled to -78 °C. TFA (1.71 ml, 22.2 mmol, 2.7 eq.) was added and the reaction mixture was allowed to warm to 0 °C over a period of 1.5 h. The mixture was carefully added to an ice-cold solution of $NaHCO_3$ (1.0 M, 90 ml) and then extracted with CH_2Cl_2 (3 x). The combined organic layers were dried over $MgSO_4$ and the solvent was removed under reduced pressure. The mixture was purified by FC twice (hexane/EtOAc 9/1 to 4/1) affording the desired diastereoisomer **MZ17-*cis*** (1.51 g, 44%) as a light yellow solid and the other diastereoisomer **MZ17-*trans*** (960 mg, 28%) also as a light yellow solid.

MZ17-*cis*

TLC: R_f = 0.48 (hexane/EtOAc 2/1). **M.p**: 60-63.5 °C. **[α]$_D^{20}$**: -77.13 (c 1.0 in $CHCl_3$). **^{1}H-NMR** (400 MHz, $CDCl_3$): δ 7.58 (bs, 1H); 7.28 (d, *J* = 8.4 Hz, 1H), 6.79 (d, *J* = 1.9 Hz, 1H), 6.67 (dd, *J* = 8.4, 2.1 Hz, 1H), 4.18 (m, 1H), 3.81 (s, 3H), 3.76 (dd, *J* = 11.2, 4.2 Hz, 1H), 3.07 (ddd, *J* = 15.1, 4.2, 1.9 Hz, 1H), 2.77 (ddd, *J* = 15.0, 11.2, 2.6 Hz, 1H), 2.02 (m, 2H), 1.64 (m, 2H), 1.03 (d, *J* = 6.5 Hz, 3H), 1.00

(d, *J* = 6.5 Hz, 3H), 1.00 (s, 9H), 0.19 (s, 6H). **^{13}C-NMR** (400 MHz, $CDCl_3$): δ 174.0, 151.7, 136.8, 135.2, 122.4, 118.3, 114.0, 107.8, 102.0, 56.6, 52.3, 50.7, 44.7, 26.2, 25.9, 24.5, 23.9, 22.0, 18.4, -4.3. **IR** (film): $\tilde{\nu}$ = 2954, 2927, 2855, 1733, 1628, 1471, 1261, 1215, 1169, 968, 841, 754. **HRMS** (ESI): *m*/*z* calcd for $C_{23}H_{37}N_2O_3Si$ $[M+H]^+$: 417.2568, found: 417.2565.

(1S,3S)-methyl 2-((R)-2-((((9H-fluoren-9-yl)methoxy)carbonyl)amino)-5-(*tert*-butoxy)-5-oxopentanoyl)-7-((*tert*-butyldimethylsilyl)oxy)-1-*iso*-butyl-2,3,4,9-tetrahydro-1H-pyrido[3,4-b]indole-3-carboxylate (**MZ19**).

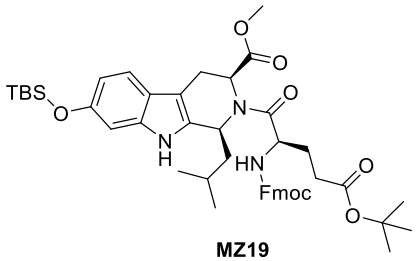

MZ19

Following the general procedure GP1 **MZ17-*cis*** was reacted with Fmoc-Glu(O*t*Bu)-OH. Amide **MZ19** was isolated after purification by FC (toluene/EtOAc 15:1) as a yellow solid (542 mg, 42%). Due to the presence of rotational isomers the NMR-spectra of **MZ19** were highly complex and no efforts were spent on the detailed interpretation of the spectral data obtained for this intermediate.

TLC: R_f = 0.65 (hexane/EtOAc 2/1). **HRMS** (ESI): *m*/*z* calcd for $C_{47}H_{62}N_3O_8Si$ $[M+H]^+$: 8244301, found: 824.4288.

***Tert*-butyl 3-((3S,6S,12aS)-9-((*tert*-butyldimethylsilyl)oxy)-6-*iso*-butyl-1,4-dioxo-1,2,3,4,6,7,12,12a-octahydropyrazino[1',2':1,6]pyrido[3,4-b]indol-3-yl)propanoate** (**MZ20**).

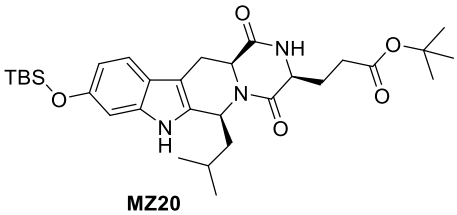

MZ20

Following the general procedure GP2, compound **MZ20** was isolated after purification by FC (hexane/EtOAc 2/1) as a light yellow solid (263 mg, 84%).
TLC: R_f = 0.13 (hexane/EtOAc 2/1). **M.p**: 174.8-178.0 °C. **$[\alpha]_D^{20}$**: -65.38 (c 0.78 in $CHCl_3$). **^{1}H-NMR** (400 MHz, $CDCl_3$): δ 7.76 (s, 1H), 7.38 (d, *J* = 8.5 Hz, 1H), 6.84 (d, *J* = 1.8 Hz, 1H), 6.73 (dd, *J* = 8.5, 2.1 Hz, 1H), 5.44 (dd, *J* = 9.2, 4.1 Hz, 1H), 4.02 (m, 2H), 3.52 (dd, *J* = 15.8, 4.9 Hz, 1H), 3.02 (dd, 15.7, 11.7 Hz, 1H), 2.50 (t, 6.6 Hz, 2H), 2.37 (m, 1H), 2.20 (m, 1H), 1.75 (ddd, 14.7, 10.2, 4.4 Hz, 1H), 1.60 (m, 1H), 1.53 (m, 1H), 1.47 (s, 9H), 1.06 (d, *J* = 6.5 Hz, 3H), 1.00 (s, 9H), 0.85 (d,

6.3 Hz, 3H), 0.20 (s, 6H).**^{13}C-NMR** (400 MHz, $CDCl_3$): δ 173.5, 169.9, 168.5, 152.0, 136.7, 133.4, 121.3, 118.5, 114.6, 106.8, 102.2, 81.6, 56.0, 54.4, 51.3, 46.0, 31.6, 28.2, 25.9, 25.2, 25.0, 24.0, 21.9, 21.8, 18.4, -4.2. **IR** (film): $\tilde{\nu}$ = 3017, 2956, 2932, 2858, 1687, 1214, 1158, 753, 668. **HRMS** (ESI): *m*/*z* calcd for $C_{31}H_{48}N_3O_5Si$ $[M+H]^+$: 570.3358, found: 570.3355.

***Tert*-butyl 3-((3S,6S,12aS)-9-hydroxy-6-*iso*-butyl-1,4-dioxo-1,2,3,4,6,7,12,12a-octahydropyrazino[1',2':1,6]pyrido[3,4-b]indol-3-yl)propanoate** (**MZ21**) [10].

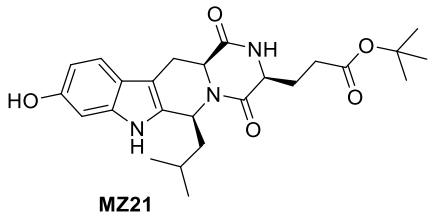

MZ21

To a solution of **MZ20** (0.600 g, 1.05 mmol, 1.0 eq.) in THF (14 ml) was added TBAF (1M in THF, 0.413 g, 1.58 mmol, 1.5 eq.) and the reaction was stirred at room temperature for 20 min. The reaction was quenched with water and the mixture was extracted with EtOAc (3 x). The combined organic layers were dried over $MgSO_4$ and the solvent removed under reduced pressure. The crude product was purified by FC (hexane/EtOAc 1/2) obtaining the desired product **MZ21** (427 mg, 89%) as a white solid.

TLC: R_f = 0.26 (hexane/EtOAc 1/2). **M.p**: 126.5-128.2 °C. **$[\alpha]_D^{20}$**: -3.33 (c 0.30 in MeOH). **^{1}H-NMR** (400 MHz, $CDCl_3$): δ 10.67 (s, 1H), 8.87 (s, 1H), 8.30 (s, 1H), 7.28 (d, *J* = 8.4 Hz, 1H), 6.71 (d, 2.0 Hz, 1H), 6.52 (dd, *J* = 8.5, 2.1 Hz, 1H), 5.27 (dd, *J* = 7.9, 4.6 Hz, 1H), 4.11 (dd, *J* = 11.5, 4.7 Hz, 1H), 4.03 (t, *J* = 5.0 Hz, 1H), 3.26 (dd, *J* = 15.6, 5.0 Hz, 1H), 2.74 (dd, *J* = 15.5, 11.8 Hz, 1H), 2.36 (m, 2H), 2.05 (m, 1H), 1.95 (m, 1H), 1.54 (m, 2H), 1.41 (s, 9H), 0.91 (d, *J* = 6.4 Hz, 3H), 0.76 (d, *J* = 6.5 Hz, 3H). **^{13}C-NMR** (400 MHz, $CDCl_3$): δ 171.8, 169.8, 152.9, 136.9, 132.7, 119.5, 118.0, 109.1, 105.1, 96.7, 79.7, 55.1, 52.5, 50.1, 45.7, 30.4, 27.8, 24.9, 24.1, 23.8, 22.1, 21.5. **IR** (film): $\tilde{\nu}$ = 3292, 2927, 1684, 1392, 1368, 1327, 1215, 1154, 754. **HRMS** (ESI): *m*/*z* calcd for $C_{25}H_{34}N_3O_5$ $[M+H]^+$: 456.2493, found: 456.2494.

***Tert*-butyl 3-((3S,6S,12aS)-9-(allyloxy)-6-*iso*-butyl-1,4-dioxo-1,2,3,4,6,7,12,12a-octahydropyrazino[1',2':1,6]pyrido[3,4-b]indol-3-yl)propanoate** (**MZ25**) [11].

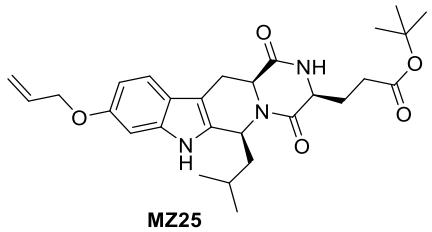

MZ25

To a suspension of NaH (60% in mineral oil, 2.6 mg, 0.0659 mmol, 1.0 eq.) in DMF (0.02 ml) was added a solution of **MZ21** (0.03 g, 0.0659 mmol, 1.0 eq.) in DMF (0.2 ml) and the mixture was stirred for 30 min. Then allyl iodide (6.6 µl, 0.0724 mmol, 1.1 eq.) was added and the reaction was stirred for 17 h. The reaction was quenched with ice-cold water and the mixture extracted with Et_2O (5 x). The combined organic layers were dried over $MgSO_4$ and the solvent removed under reduced pressure. Compound **MZ25** was isolated after purification by FC (CH_2Cl_2 to CH_2Cl_2/MeOH 80/1) and HPLC as a light yellow solid (5.88 mg, 18%)

TLC: R_f = 0.26 (hexane/EtOAc 1/2). **M.p**: 103-105.5 °C. **$[\alpha]_D^{20}$:** -82.47 (c 0.85 in $CHCl_3$). **^{1}H-NMR** (400 MHz, $CDCl_3$): δ 7.93 (bs, 1H), 7.43 (d, *J* = 8.6 Hz, 1H), 6.90 (d, *J* = 2.2 Hz, 1H), 6.85 (dd, *J* = 8.6, 2.2 Hz, 1H), 6.09 (ddt, *J* = 17.1, 10.5, 5.3 Hz, 1H), 5.43 (m, 2H), 5.29 (dd, *J* = 10.5, 1.4 Hz, 1H), 4.58 (dt, *J* = 5.3, 1.4 Hz, 2H), 4.02 (dt, *J* = 8.9, 4.5 Hz, 2H), 3.52 (dd, *J* = 15.8, 4.9 Hz, 1H), 3.02 (dd, *J* = 15.7, 11.7 Hz, 1H), 2.50 (t, *J* = 6.7 Hz, 2H), 2.37 (ddd, *J* =17.5, 10.9, 6.4 Hz, 1H), 2.21 (dt, *J* = 20.8, 6.3 Hz, 1H), 1.75 (ddd, *J* = 14.3, 10.0, 4.5 Hz, 1H), 1.56 (m, 2H), 1.46 (s, 9H), 1.05 (d, *J* = 6.5 Hz, 3H), 0.83 (d, *J* = 6.4 Hz, 3H).**^{13}C-NMR** (500 MHz, $CDCl_3$): δ 173.3, 169.8, 168.3, 155.4, 136.5, 133.7, 133.1, 120.8, 120.0, 118.7, 117.6, 110.4, 106.7, 96.5, 81.5, 69.6, 55.9, 54.3, 51.2, 45.9, 31.4, 28.1, 25.1, 24.9, 23.9, 21.8, 21.7. **IR** (film): $\tilde{\nu}$ =. 3019, 2357, 1688, 1214, 751, 668. **HRMS** (ESI): *m*/*z* calcd for $C_{28}H_{38}N_3O_5$ $[M+H]^+$: 469.2806, found: 469.2798. **RP-HPLC:** column: SymmetryPrep™ C18, 5µm, 19 x 100 mm, gradient: ACN + 0.1% TFA/H_2O 45/55 to 65/35, 1 ml/min, 254 nm, R_t = 9.03 min.

***Tert*-butyl 3-((3S,6S,12aS)-9-(cyclopentyloxy)-6-*iso*-butyl-1,4-dioxo-1,2,3,4,6,7,12,12a-octahydropyrazino[1',2':1,6]pyrido[3,4-b]indol-3-yl)propanoate** (**MZ29**).

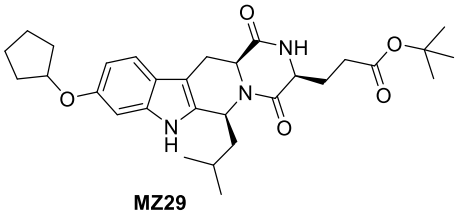

MZ29

Following the general procedure GP3 **MZ21** was reacted with bromocyclopentane. Derivative **MZ29** was isolated after purification by FC (CH_2Cl_2/MeOH 5%) and HPLC as a colorless oil (4.50 mg, 13%)

TLC: R_f = 0.23 (CH_2Cl_2/MeOH 80/1). **$[\alpha]_D^{20}$:** -84.08 (c 0.44 in $CHCl_3$). **^{1}H-NMR** (400 MHz, $CDCl_3$): δ 7.83 (bs, 1H), 7.41 (d, *J* = 8-6 Hz, 1H), 6.86 (d, *J* = 2.0 Hz, 1H), 6.81 (d, *J* = 1.9 Hz, 1H), 5.44 (dd, *J* = 9.2, 4.1 Hz, 1H), 4.78 (p, *J* = 4.3 Hz, 1H), 4.02 (dt, 9.2, 4.6 Hz, 2H), 3.52 (dd, *J* = 15.8, 4.9 Hz, 1H), 3.02 (dd, *J* = 15.7, 11.7 Hz, 1H), 2.50 (t, *J* = 6.50 Hz, 2H), 2.37 (ddd, *J* = 17.4, 10.8, 6.4 Hz, 1H), 2.21 (dt, *J* = 12.9, 6.2 Hz, 1H), 1.90 (m, 4H), 1.78 (m, 4H), 1.58 (m, 4H), 9.18 (s, 9H), 3.04 (d, *J* = 6.5 Hz, 3H), 3.04 (d, *J* = 6.4 Hz, 3H). **^{13}C-NMR** (500 MHz, $CDCl_3$): δ 137.3, 170.0, 168.4, 154.7, 136.6, 133.0, 120.5, 118.6, 111.2 106.6, 97.5, 81.4, 79.9, 55.9, 54.2, 51.2, 45.9, 32.9, 32.9, 31.3, 28.1, 25.1, 24.8, 24.0, 23.9, 21.9, 21.7. **IR** (film): $\tilde{\nu}$ = 2958, 2359, 1684, 1653, 1558, 1399, 1221, 1160, 1038, 771, 666. **HRMS** (ESI): *m*/*z* calcd for $C_{30}H_{41}N_3NaO_5$ $[M+Na]^+$ 546.2938, found: 546.2930. **RP-HPLC:** column: SymmetryPrep™ C18, 5µm, 19 x 100 mm, gradient: ACN + 0.1% TFA/H_2O 50/50 to 70/30, 1 ml/min, 254 nm, R_t = 9.79 min.

***Tert*-butyl 3-((3S,6S,12aS)-9-(2-aminoethoxy)-6-*iso*-butyl-1,4-dioxo-1,2,3,4,6,7,12,12a-octahydropyrazino[1',2':1,6]pyrido[3,4-b]indol-3-yl)propanoate** (**MZ34**) [5].

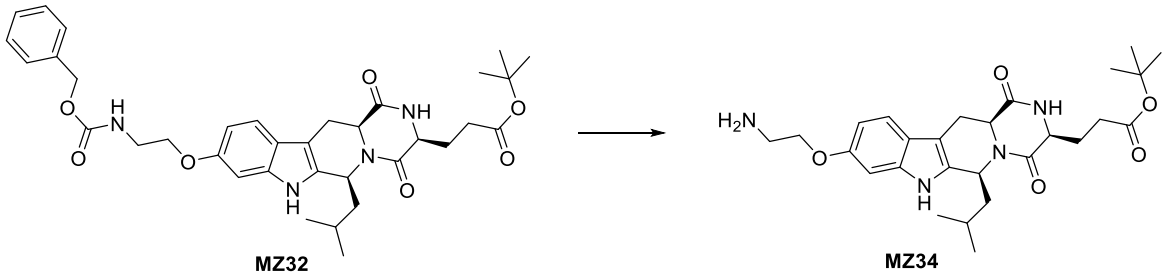

MZ32 MZ34

Following the general procedure GP3 **MZ21** was reacted with 2-(((benzyloxy)carbonyl)amino)ethyl 4-methylbenzenesulfonate obtaining **MZ32** which was directly used for the last step without further purification.

To a solution of **MZ32** (30.0 mg, 0.0474 mmol, 1.0 eq.) in MeOH (1.0 ml) was added Pd/C 10% (4.4 mg) under argon. Then the flask was flushed with hydrogen at r.t. for 8 h. After complete conversion of the starting material the hydrogen was

replaced by argon and the mixture was filtered over celite. The solvent was removed under reduced pressure. The crude product was purified by FC (CH_2Cl_2/MeOH 20%) and by HPLC affording the desired product **MZ34** (5.67 mg, 24%) as sticky white solid.

TLC: R_f = 0.23 (CH_2Cl_2/MeOH 80/1). **$[\alpha]_D^{20}$:** -32.05(c 0.78 in $CHCl_3$). **^{1}H-NMR** (400 MHz, DMSO-d_6): δ 10.87 (bs, 1H), 8.31 (s, 1H), 7.98 (bs, 2H), 7.33 (d, *J* = 8.6 Hz, 1H), 6.89 (d, *J* = 2.2 Hz, 1H), 6.71 (dd, *J* = 8.6, 2.2 Hz, 1H), 5.76 (d, *J* = 8.8 Hz, 1H), 4.26 (dd, *J* = 11.8, 4.2 Hz, 1H), 4.22 (t, *J* = 4.4 Hz, 1H), 4.14 (m, 2H), 3.24 (bs, 2H), 3.07 (dd, *J* = 15.2, 4.2 Hz, 1H), 2.84 (m, 1H), 2.31 (ddd, *J* = 15.9, 9.8, 6.0 Hz, 1H), 2.16 (ddd, *J* = 15.7, 10.5, 5.1 Hz, 1H), 2.05 (m, 2H), 1.84 (t, *J* = 10.6 Hz, 1H), 1.59 (m, 2H), 1.40 (s, 9H), 1.03 (d, *J* = 5.7 Hz, 3H), 0.92 (d, *J* = 5.9 Hz, 3H). **^{13}C-NMR** (500 MHz, DMSO-d_6): δ 171.7, 167.3, 165.7, 153.9, 136.4, 133.4, 121.2, 118.4, 108.8, 104.8, 96.3, 79.8, 64.9, 52.8, 52.3, 47.0, 42.1, 38.6, 29.8, 27.8, 27.5, 26.4, 24.8, 23.4, 21.7. **IR** (film): $\tilde{\nu}$ = 3403, 29565, 2930, 2921, 2871, 2362, 2356, 1675, 1451, 1369, 1328, 1247, 1202, 1173, 1155, 1136, 1019, 952, 837, 800, 722, 681, 669. **HRMS** (ESI): *m*/*z* calcd for $C_{27}H_{39}N_4O_5$ $[M+H]^+$: 499.2915, found: 499.2915. **RP-HPLC:** column: SymmetryPrep™ C18, 5µm, 19 x 100 mm, gradient: ACN + 0.1% TFA/H_2O 25/75 to 35/65, 1 ml/min, 254 nm, R_t = 10.27 min.

Benzyl 2-bromoacetate (**MZ41**) [12].

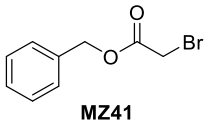

MZ41

To a solution of bromo aceticacid (300 mg, 2.16 mmol, 1.0 eq.) and benzyl alcohol (0.229 ml, 2.20 mmol, 1.02 eq.) in CH_2Cl_2 (14 ml) were added DCC (459 mg, 2.22 mmol, 1.03 eq.) and a catalytic amount of DMAP (21.0 mg, 0.172 mmol, 8 mol%). The reaction was stirred for 17 h at room temperature. The solvent was removed under reduced pressure and the crude product was purified by FC (CH_2Cl_2) affording **MZ41** (430 mg, 87%) as a colorless oil.

TLC: R_f = 0.9 (hexane/EtOAc 1/2). **^{1}H-NMR** (400 MHz, $CDCl_3$): δ 7.38 (m, 5H), 5.21 (s, 2H), 3.88 (s, 2H). **HRMS** (ESI): *m*/*z* calcd for $C_9H_9BrO_2$ $[M+H]^+$: 227.9786, found: 227.9781.

***Tert*-butyl 3-((3S,6S,12aS)-9-(2-(benzyloxy)-2-oxoethoxy)-6-*iso*-butyl-1,4-dioxo-1,2,3,4,6,7,12,12a-octahydropyrazino[1',2':1,6]pyrido[3,4-b]indol-3-yl)propanoate** (**MZ42**).

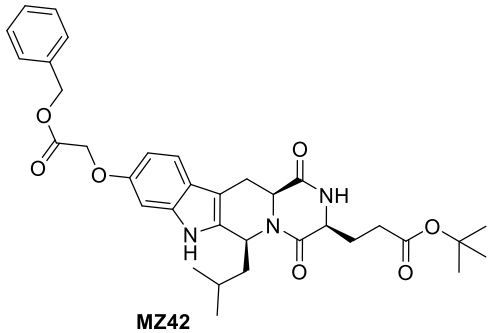

MZ42

Following the general procedure GP3 **MZ21** was reacted with **MZ41**. Derivative **MZ42** was isolated after purification by FC (hexane/EtOAc 1/1) as a white solid (39.2 mg, 74%).

TLC: R_f = 0.18 (hexane/EtOAc 1/1). M.p.: 89-91.5 °C. **$[\alpha]_D^{20}$**: -23.63 (c 0.55 in $CHCl_3$). **^{1}H-NMR** (400 MHz, $CDCl_3$) δ 7.95 (s, 1H), 7.43 (d, *J* = 8.3 Hz, 1H), 7.34 (s, 5H), 6.84 (d, *J* = 8.3 Hz, 3H), 5.44 (dd, *J* = 9.1, 4.1 Hz, 1H), 5.24 (s, 2H), 4.70 (s, 2H), 4.01 (dd, *J* = 11.0, 5.1 Hz, 2H), 3.52 (dd, *J* = 15.8, 4.8 Hz, 1H), 3.02 (dd, *J* = 15.7, 11.8 Hz, 1H), 2.50 (t, *J* = 6.6 Hz, 2H), 2.37 (ddd, *J* = 17.1, 10.7, 6.2 Hz, 1H), 2.21 (td, *J* = 12.7, 6.3 Hz, 1H), 1.80 – 1.70 (m, 1H), 1.61 – 1.50 (m, 2H), 1.46 (s, 9H), 1.05 (d, *J* = 6.5 Hz, 3H), 0.84 (d, *J* = 6.4 Hz, 3H). **^{13}C-NMR** (101 MHz, $CDCl_3$) δ 173.5, 169.7, 169.4, 168.5, 154.8, 136.4, 135.4, 133.8, 128.8, 128.6, 121.7, 119.0, 110.1, 106.9, 97.2, 81.6, 67.1, 66.6, 56.0, 54.4, 51.2, 46.0, 31.6, 28.2, 25.2, 24.0, 24.0, 21.9, 21.8. **IR** (film): $\tilde{\nu}$ = 3296, 2978, 2360, 1729, 1686, 1635, 1368, 1157. **HRMS** (ESI): *m*/*z* calcd for $C_{34}H_{41}N_3NaO_7$ $[M+Na]^+$ 626.2837, found: 626.2831.

2-(((3S,6S,12aS)-3-(3-(*tert*-butoxy)-3-oxopropyl)-6-*iso*-butyl-1,4-dioxo-1,2,3,4,6,7,12,12a-octahydropyrazino[1',2':1,6]pyrido[3,4-b]indol-9-yl)oxy)acetic acid (**MZ44**) [5].

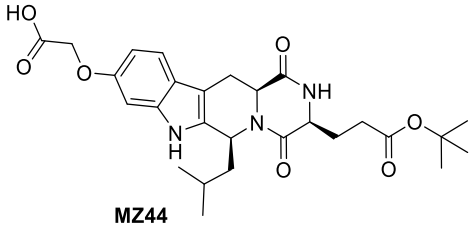

MZ44

To a solution of **MZ42** (36.0 mg, 0.0596 mmol, 1.0 eq.) in MeOH (1.3 ml) was Pd/C 10% (5.5 mg) under argon. Then the flask was flushed with hydrogen at r.t. for 3 h. After complete conversion of the starting material the hydrogen was replaced by argon and the mixture was filtered over celite. The solvent was removed under reduced pressure. The crude product was purified by FC (CH_2Cl_2/MeOH 20%) obtaining the desired derivative **MZ44** (17.5 mg, 57%) as a grey solid.

TLC: R_f = 0.15 (CH_2Cl_2/MeOH 20%). M.p.: 88-90.5 °C. **$[\alpha]_D^{20}$**: -79.99 (c 0.20 in $CHCl_3$). **^{1}H-NMR** (400 MHz, DMSO-d_6) δ 10.88 (s, 1H), 8.30 (s, 1H), 7.33 (d, *J* = 8.6 Hz, 1H), 6.79 (d, *J* = 2.1 Hz, 1H), 6.62 (dd, *J* = 8.5, 2.3 Hz, 1H), 5.30 (d, *J* = 6.9 Hz, 1H), 4.21 (s, 2H), 4.11 (dd, *J* = 11.7, 4.8 Hz, 1H), 4.05 (t, *J* = 4.4 Hz, 1H), 2.87 – 2.68 (m, 1H), 2.41 – 2.30 (m, 2H), 2.15 – 2.02 (m, 1H), 2.02 – 1.88 (m, 1H), 1.75 (s, 1H), 1.62 – 1.51 (m, 2H), 1.41 (s, 9H), 1.28 – 1.19 (m, 1H), 0.89 (d, *J* = 6.4 Hz, 3H), 0.75 (d, *J* = 6.5 Hz, 3H). **^{13}C-NMR** (400 MHz, DMSO-d_6) δ 173.3, 171.8, 169.8, 168.8, 154.7, 136.5, 133.2, 120.0, 117.9, 109.2, 105.0, 95.9, 79.7, 67.9, 55.1, 52.5, 50.2, 45.5, 30.4, 27.8, 24.9, 24.1, 23.8, 22.1, 21.5. **IR** (film): $\tilde{\nu}$ = 3373, 2368, 1652, 1634, 1417, 1332, 1159, 1014. **HRMS** (ESI): *m*/*z* calcd for $C_{27}H_{35}N_3NaO_7$ $[M+Na]^+$ 536.2367, found: 536.2366.

Fumitremorgin C (FTC).

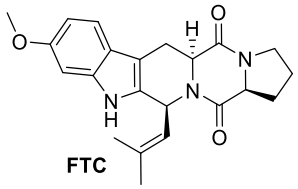

FTC

Details of the synthesis of fumitregmorgin C will be published elsewhere.

TLC: R_f = 0.20 (hexane/EtOAc 1/4). **$[\alpha]_D^{20}$:** -13.16 (c 0.76 in $CHCl_3$). **^{1}H-NMR** (400 MHz, $CDCl_3$) δ 7.77 (s, 1H), 7.43 (d, *J* = 8.6 Hz, 1H), 6.86 (d, *J* = 2.2 Hz, 1H), 6.81 (dd, *J* = 8.6, 2.3 Hz, 1H), 5.98 (d, *J* = 9.8 Hz, 1H), 4.99 – 4.81 (m, 1H), 4.18 (ddd, *J* = 11.6, 5.1, 1.3 Hz, 1H), 4.12 (d, *J* = 7.2 Hz, 1H), 3.83 (s, 3H), 3.64 (ddd, *J* = 8.4, 5.3, 3.0 Hz, 2H), 3.52 (dd, *J* = 16.0, 5.0 Hz, 1H), 3.10 (ddd, *J* = 16.0, 11.6, 1.2 Hz, 1H), 2.41 (dtd, *J* = 12.8, 6.9, 3.1 Hz, 2H), 2.24 (dddd, *J* = 12.9, 10.9, 9.2, 7.2 Hz, 1H), 1.99 (d, *J* = 1.3 Hz, 3H), 1.93 (dddd, *J* = 10.9, 6.8, 4.0, 2.1 Hz, 1H), 1.65 (d, *J* = 1.3 Hz, 3H). **^{13}C-NMR** (101 MHz, $CDCl_3$) δ 169.7, 165.9, 156.7, 137.2, 134.1, 132.3, 124.3, 120.9, 119.0, 109.7, 106.5, 95.4, 59.4, 56.9, 55.9, 51.2, 45.6, 28.7, 25.9, 23.2, 22.1, 18.2. **IR** (film): $\tilde{\nu}$ = 2981, 2901, 1683, 1669, 1654, 1636, 1540, 1507, 1473, 1395, 1220, 1065, 1046, 772, 669. **HRMS** (ESI): *m*/*z* calcd for $C_{22}H_{26}N_3O_3$ $[M+H]^+$: 380.1969, found: 380,1971.

(1*S*,3*S*)-Methyl 1-*iso*-butyl-2,3,4,9-tetrahydro-1*H*-pyrido[3,4-b]indole-3-carboxylate and (1*R*,3*S*)-methyl 1-*iso*-butyl-2,3,4,9-tetrahydro-1*H*-pyrido[3,4-b]indole-3-carboxylate (**RX1 and RX1b**) [13].

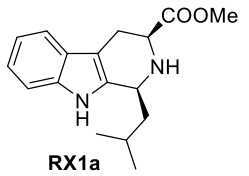

RX1a

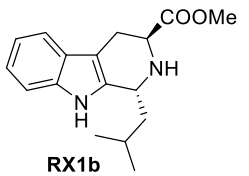

RX1b

L-Tryptophan methyl ester hydrochloride (1.50 g, 5.89 mmol, 1.0 eq.) was dissolved in CH_2Cl_2 (100 ml) and aq. Na_2CO_3 (1.0 M, 50 ml) was added. The mixture was stirred until a clear solution was obtained. The organic layer was separated and the aqueous phase was extracted with CH_2Cl_2 (3 x). The combined organic layers were dried over anhydrous $MgSO_4$. The solvent was removed under reduced pressure and the free base was obtained as a pale yellow gum. This material was dissolved in CH_2Cl_2 (50 ml) and isovaleraldehyde (0.70 ml, 6.49 mmol, 1.1 eq.) was added. This mixture was stirred for 30 min followed by addition of trimethyl orthoformate (6.64 ml, 24.1 mmol, 4.1 eq.). After stirring overnight (16 h), the solution was concentrated and dried under vacuum to afford the crude imine as a pale yellow gum. This material was dissolved in dry CH_2Cl_2 and TFA (0.72 ml, 9.42 mmol, 1.6 eq.) was added at 0 °C. The mixture was stirred for 30 min at 0 °C and for further 4 h at r.t. Saturated aqueous $NaHCO_3$ (30 ml) was added carefully and the mixture was extracted with CH_2Cl_2 (3 x). The combined organic layers were dried over $MgSO_4$ and the solvent was removed under reduced pressure. FC (hexane/EtOAc 9:1 to 4:1 to 2:1) gave both the *cis*-carboline **RX1a** (894 mg, 53%) the *trans*-carboline **RX1b** (489 mg, 29%) as colourless foams.

RX1a

TLC: R_f = 0.29 (hexane/EtOAc 4:1). **^{1}H-NMR** (400 MHz, $CDCl_3$) δ 7.80 (s, 1H), 7.48 (d, *J* = 7.6 Hz, 1H), 7.31 (d, *J* = 7.9 Hz, 1H), 7.19 – 7.14 (m, 1H), 7.11 (m, 1H), 4.27 – 4.19 (m, 1H), 3.83 (s, 3H), 3.79 (dd, *J* = 11.2, 4.2 Hz, 1H), 3.14 (ddd, *J* = 15.0, 4.2, 1.8 Hz, 1H), 2.88 – 2.78 (m, 1H), 2.11 – 1.96 (m, 2H), 1.75 – 1.59 (m, 2H), 1.05 (d, *J* = 6.5 Hz, 3H), 1.01 (d, *J* = 6.6 Hz, 3H). **^{13}C-NMR** (101 MHz, $CDCl_3$) δ 174.4, 136.1, 136.0, 127.3, 121.8, 119.6, 118.1, 110.8, 107.0, 52.5, 52.2, 48.2, 44.6, 95 25.2, 24.8, 23.8, 21.8. **IR** (film): = 3394, 2953, 2925, 1731, 1465, 1450, 1437, 1366, 1346, 1315, 1267, 1214, 1171, 1010. 997, 735, 701 cm^{-1}. **HRMS** (ESI): *m*/*z* calcd for $C_{17}H_{23}N_2O_2$ $[M+H]^+$: 287.1754, found: 287.1758.

RX1b

TLC: R_f = 0.19 (hexane/EtOAc 4:1). **^{1}H-NMR** (400 MHz, $CDCl_3$) δ 7.77 (brs, 1H), 7.49 (d, *J* = 7.6 Hz, 1H), 7.32 – 7.27 (m, 1H), 7.18 – 7.13 (m, 1H), 7.13 – 7.08 (m, 1H), 4.30 (dd, *J* = 10.0, 4.1 Hz, 1H), 3.98 (dd, *J* = 7.4, 5.3 Hz, 1H), 3.76 (s, 3H), 3.12 (ddd, *J* = 15.3, 5.2, 1.0 Hz, 1H), 2.99 (ddd, *J* = 15.3, 7.5, 1.4 Hz, 1H), 2.37 (brs, 1H), 2.02 – 1.89 (m, 1H), 1.72 (ddd, *J* = 14.7, 10.0, 4.8 Hz, 1H), 1.52 (ddd, *J* = 13.7, 9.5, 4.2 Hz, 1H), 1.04 (d, *J* = 6.6 Hz, 3H), 1.01 (d, *J* = 6.6 Hz, 3H). **^{13}C-NMR** (101 MHz, $CDCl_3$) δ 173.9, 136.1, 136.0, 127.3, 121.7, 119.6, 118.0, 110.9, 107.8, 56.6, 52.3, 50.6, 44.4, 26.1, 24.4, 23.9, 21.8. **IR** (film): = 3392, 2952, 2925, 2868, 1731, 1465, 1452, 1436, 1329, 1272, 1217, 1199, 1172, 1158, 1025, 1009,

737, 700 cm^{-1}. **HRMS** (ESI): *m*/*z* calcd for $C_{17}H_{23}N_2O_2$ $[M+H]^+$: 287.1754, found: 287.1754.

(1*S*,3*S*)-Methyl2-((*S*)-2-((((9*H*-fluoren-9-yl)methoxy)carbonyl)amino)-6-((*tert*-butoxycarbonyl) amino)hexanoyl)-1-*iso*-butyl-2,3,4,9-tetrahydro-1*H*-pyrido[3,4-*b*]indole-3- carboxylate (**RX2**).

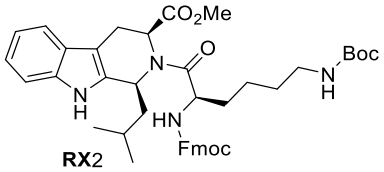

RX2

Following the general procedure GP1 **RX1a** was reacted with Fmoc-Lys(Boc)-OH. Amide **RX2** was isolated after purification by FC (hexane/EtOAc 9/1 to 4/1 to 2/1 to 1/1) as a pale brown foam (259 mg, 67%). Due to the presence of rotational isomers the NMR-spectra of **RX2** were highly complex and no efforts were spent on the detailed interpretation of the spectral data obtained for this intermediate.

TLC: Rf = 0.38 (hexane/EtOAc 2:1). **HRMS** (ESI): *m*/*z* calcd for $C_{43}H_{53}N_4O_7$ $[M+H]^+$: 737.3909, found: 737.3897.

***Tert*-butyl(4-((3*S*,6*S*,12a*S*)-6-*iso*-butyl-1,4-dioxo-1,2,3,4,6,7,12,12a-octahydropyrazino[1',2':1,6] pyrido[3,4-b]indol-3-yl)butyl)carbamate** (**RX3**).

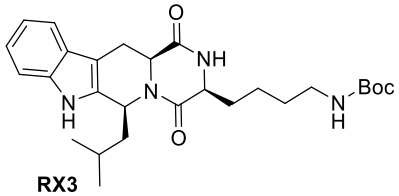

RX3

Following the general procedure GP2, compound **RX3** was isolated after purification by FC (hexane/EtOAc 2/1 to 1/1 to 1/2 to EtOAc) as a colorless solid (138 mg, 90%)

TLC: R_f = 0.22 (hexane/EtOAc 1:2). **M.p.**: 235-240 °C ($CHCl_3$, decomposition). **$[\alpha]_D^{20}$**: -30.0 (*c* = 0.10 in $CHCl_3$). **^{1}H-NMR** (400 MHz, DMSO-d_6) δ 11.08 (s, 1H), 8.28 (s, 1H), 7.53 (d, *J* = 7.7 Hz, 1H), 7.35 (d, *J* = 7.9 Hz, 1H), 7.10 – 7.03 (m, 1H), 7.03 – 6.98 (m, 1H), 6.76 (t, *J* = 5.6 Hz, 1H), 5.37 (dd, *J* = 7.8, 4.9 Hz, 1H), 4.14 (dd, *J* = 11.7, 4.7 Hz, 1H), 4.00 (t, *J* = 4.6 Hz, 1H), 3.38 (dd, 1H, covered by water peak), 2.92 (dd, *J* = 11.2, 5.5 Hz, 2H), 2.81 (dd, *J* = 15.5, 11.8 Hz, 1H), 1.87 – 1.68 (m, 2H), 1.62 – 1.52 (m, 2H), 1.48 –1.42 (m, 1H), 1.44 – 1.35 (m, 2H), 1.41 – 1.32 (m, 2H), 1.38 (s, 9H), 0.91 (d, *J* = 6.5 Hz, 3H), 0.76 (d, *J* = 6.5 Hz, 3H). **^{13}C-NMR** (101 MHz, DMSO-d_6) δ 169.7, 169.1, 155.6, 135.8, 135.0, 125.8, 120.8, 118.8, 117.8, 111.4, 105.4, 77.3, 55.2, 53.2, 50.0, 45.7, 39.5, 29.5, 29.0, 28.3, 24.1, 23.8, 22.1, 21.5, 21.4. **IR** (film): = 3288, 2954, 2925, 2359, 1682, 1651, 1526, 1456,

1393, 1367, 1323, 1304, 1273, 1255, 1165, 1143, 1056, 992, 935, 866, 747, 718, 676, 635 cm^{-1}. **HRMS** (ESI): *m*/*z* calcd for $C_{27}H_{38}N_4NaO_4$ $[M+Na]^+$: 505.2785, found: 505.2782.

(3*S*,6*S*,12a*S*)-3-(4-aminobutyl)-6-*iso*-butyl-2,3,12,12a-tetrahydropyrazino[1',2':1,6]pyrido[3,4-b]indole-1,4(6*H*,7*H*)-dione (**RX4**) [7].

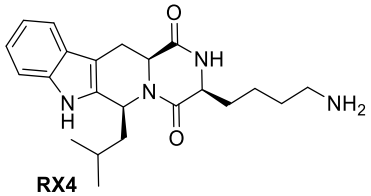

RX4

Carbamate **RX3** (37.0 mg, 0.0770 mmol, 1.0 eq.) was suspended in CH_2Cl_2 (2 ml). Addition of TFA (1 ml) resulted in a clear yellow solution. After the mixture had been stirred for 1 h, it was carefully added to aqueous Na_2CO_3 (1.0 M, 5 ml). The mixture was extracted with $CHCl_3$ (3 x) and dried over $MgSO_4$. Removal of the solvent under reduced pressure gave crude amine **RX4** (41 mg, 140%) as a pale yellow gum. This material was used in the next step without further purification.

TLC: R_f = 0.05 (CH_2Cl_2/MeOH 9:1). **$[\alpha]_D^{20}$**: -62.1 (*c* = 0.33 in MeOH). **^{1}H-NMR** (400 MHz, MeOD-d_4) δ 7.87 (s, 1H), 7.48 (d, *J* = 7.7 Hz, 1H), 7.34 (d, *J* = 8.0 Hz, 1H), 7.12 – 7.05 (m, 1H), 7.02 (dd, *J* = 10.9, 4.0 Hz, 1H), 5.47 (dd, *J* = 8.2, 4.5 Hz, 1H), 4.09 (dd, *J* = 11.5, 4.6 Hz, 1H), 4.02 (t, *J* = 4.2 Hz, 1H), 3.47 (dd, *J* = 15.6, 4.8 Hz, 1H), 2.93 (dd, *J* = 15.4, 11.8 Hz, 1H), 2.68 (t, *J* = 6.8 Hz, 2H), 1.97 – 1.89 (m, 2H), 1.73 – 1.60 (m, 2H), 1.58 – 1.42 (m, 5H), 0.96 (d, *J* = 6.5 Hz, 3H), 0.80 (d, *J* = 6.6 Hz, 3H). **^{13}C-NMR** (126 MHz, DMSO-d_6) δ 169.8, 169.1, 135.8, 135.0, 125.9, 120.9, 118.8, 117.8, 111.4, 105.4, 55.3, 53.2, 50.1, 45.8, 38.6, 28.8, 27.0, 24.2, 23.8, 22.1, 21.5, 21.1. **IR** (film): = 3228, 2958, 2926, 1673, 1453, 1436, 1404, 1328, 1203, 1182, 1135 cm^{-1}. **HRMS** (ESI): *m*/*z* calcd for $C_{22}H_{31}N_4O_2$ $[M+H]^+$: 383.2442, found: 383.2443.

***N*-(4-((3*S*,6*S*,12a*S*)-6-*iso*-butyl-1,4-dioxo-1,2,3,4,6,7,12,12a-octahydropyrazino[1',2':1,6]pyrido [3,4-*b*] indol-3-yl)butyl)-6-((7-nitrobenzo[*c*][1,2,5]oxadiazol- 4-yl)amino)hexanamide** (**RX5**) [8].

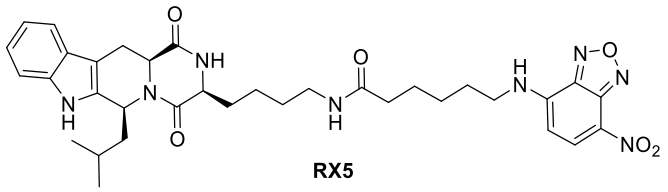

RX5

6-(*N*-(7-nitrobenz-2-oxa-1,3-diazol-4-yl)amino)hexanoic acid (90.0 µmol, 1.2 eq.) was dissolved in DMF (3 ml) under argon. EDC hydrochloride (28 mg, 0.15 mmol, 2 eq.), HOBt (20 mg, 0.15 mmol, 2.0 eq.) and Et_3N (0.14 m, 1.05 mmol, 14 eq.)

were added and the mixture was stirred for 5 min. A solution of amine **RX4** (40 mg crude material, 75.0 µmol based on quantitative Boc-cleavage, 1.0 eq.) was added and the mixture was stirred at r.t. for 16 h. The solvent was removed under reduced pressure. FC (CH_2Cl_2/MeOH 9:1) gave the amide **RX5** (42.0 mg, 84%) as an orange-brown solid.
TLC: R_f = 0.28 (CH_2Cl_2/MeOH 19:1). **$[\alpha]_D^{20}$**: -23.3 (*c* = 0.37 in MeOH). **^{1}H-NMR** (500 MHz, DMSO-d_6) δ 11.08 (s, 1H), 9.52 (s, 1H), 8.46 (d, *J* = 8.9 Hz, 1H), 8.28 (s, 1H), 7.77 (t, *J* = 5.6 Hz, 1H), 7.51 (d, *J* = 7.8 Hz, 1H), 7.34 (d, *J* = 8.0 Hz, 1H), 7.09 – 7.02 (m, 1H), 6.98 (m, 1H), 6.35 (d, *J* = 8.9 Hz, 1H), 5.36 (dd, *J* = 8.0, 4.7 Hz, 1H), 4.14 (dd, *J* = 11.7, 4.7 Hz, 1H), 4.00 (t, *J* = 4.7 Hz, 1H), 3.47 – 3.41 (m, 2H), 3.35 (dd, *J* = 10.7, 4.8 Hz, 1H), 3.10 – 2.96 (m, 2H), 2.81 (dd, *J* = 15.5, 11.8 Hz, 1H), 2.07 (t, *J* = 7.4 Hz, 2H), 1.87 – 1.79 (m, 1H), 1.78 – 1.71 (m, 1H), 1.67 (dt, *J* = 14.9, 7.5 Hz, 2H), 1.61 – 1.51 (m, 4H), 1.49 – 1.30 (m, 7H), 0.90 (d, *J* = 6.5 Hz, 3H), 0.74 (d, *J* = 6.6 Hz, 3H). **^{13}C-NMR** (126 MHz, DMSO-d_6) δ 171.9, 169.8, 169.2, 145.1, 144.4, 144.1, 137.9, 135.8, 135.0, 125.9, 120.8, 120.5, 118.8, 117.8, 111.4, 105.4, 99.1, 55.2, 53.3, 50.1, 45.8, 43.3, 38.3, 35.4, 29.3, 29.1, 27.5, 26.2, 25.0, 24.1, 23.8, 22.2, 21.7, 21.5. **IR** (film): = 3217, 2925, 2856, 1656, 1586, 1529, 1444, 1396, 1297, 1273, 1049, 1025, 1007, 822 cm-1. **HRMS** (ESI): *m*/*z* calcd for $C_{34}H_{43}N_8O_6$ $[M+H]^+$: 659.3300, found: 659.3294.

Synthesis of *N*-(5-(1-(4-(2-(6-methoxy-7-(2-(2-(2-methoxyethoxy)ethoxy)ethoxy)-3,4-dihydroisoquinolin-2(1*H*)-yl)ethyl)phenyl)-1*H*-1,2,3-triazol-4-yl)-2-propionyl-phenyl)quinoline-2-carboxamide (MB136)

General Information.

Chemicals and solvents were purchased from commercial suppliers and used without further purification.

Thin layer chromatography was performed on aluminium sheets pre-coated with silica gel 60 with fluorescent indicator UV_{254} (Macherey-Nagel). Detection was carried out by UV irradiation at wavelengths of 254 nm and 366 nm.

Automated Flash chromatography was performed with a Biotage Isolera Spektra One device. Silica gel 60 M (40 - 63 µM, Merck) was used.

The melting point was determined in open capillaries on a Stanford Research Systems OptiMelt MPA 100 and is uncorrected.

NMR spectra were recorded at room temperature on a Bruker Avance 600 (^{1}H: 600.1 MHz, ^{13}C: 150.9 MHz) instrument equipped with a cryogenic probe. Calibration was performed according to the residual solvent method with chloroform-d_1 ($CDCl_3$, ^{1}H: 7.26 ppm, ^{13}C: 77.16 ppm). The chemical shifts δ are given in ppm, coupling constants *J* in Hertz [Hz]. Splitting patterns of the signals

are abbreviated as s (singlet), d (doublet), t (triplet), m (multiplet), dd (doublet of doublets), q (quartet). The relative number of protons was determined by integration.

High resolution mass spectra were recorded with an Agilent Tech 6540 UHD Accurate Mass Q-TOF LC/MS spectrometer (Agilent Technologies) using an ESI source.

The purity of the compound (dissolved in DMSO) was determined by reverse phase HPLC (UV detection at 220 nm) HPLC (1220 Infinity LC System from Agilent) Phenomenex Luna 3 µm C18(2) 100A column (150 × 2.0 mm, 100 Å) thermostated at 40 °C. Conditions: solvent A = water (Millipore) / TFA (0.05% v/v), solvent B = MeCN (Merck, gradient grade); flow rate = 0.3 mL/min; elution with a gradient of 30% to 90% MeCN in 25 min.

Experimental Protocol and Analytical Data.

The preparation of the building blocks will be published elsewhere. Tris[(1-benzyl-1H-1,2,3-triazol-4-yl)methyl]amine) (TBTA) was synthesized according to published procedures [14].

The alkyne, the azide (1.3 eq), copper sulfate hexahydrate (0.1 eq), sodium ascorbate (0.5 eq) and (TBTA) (0.1 eq) were dissolved in dimethylformamide. The solution was stirred under nitrogen for 24 h. Dichloromethane and water were added; the organic phase was extracted with water, dried over magnesium sulfate, and concentrated. The crude product was purified by automated Flash chromatography (CH_2Cl_2: MeOH 95:5). Yield: 0.20 mmol, 54%.

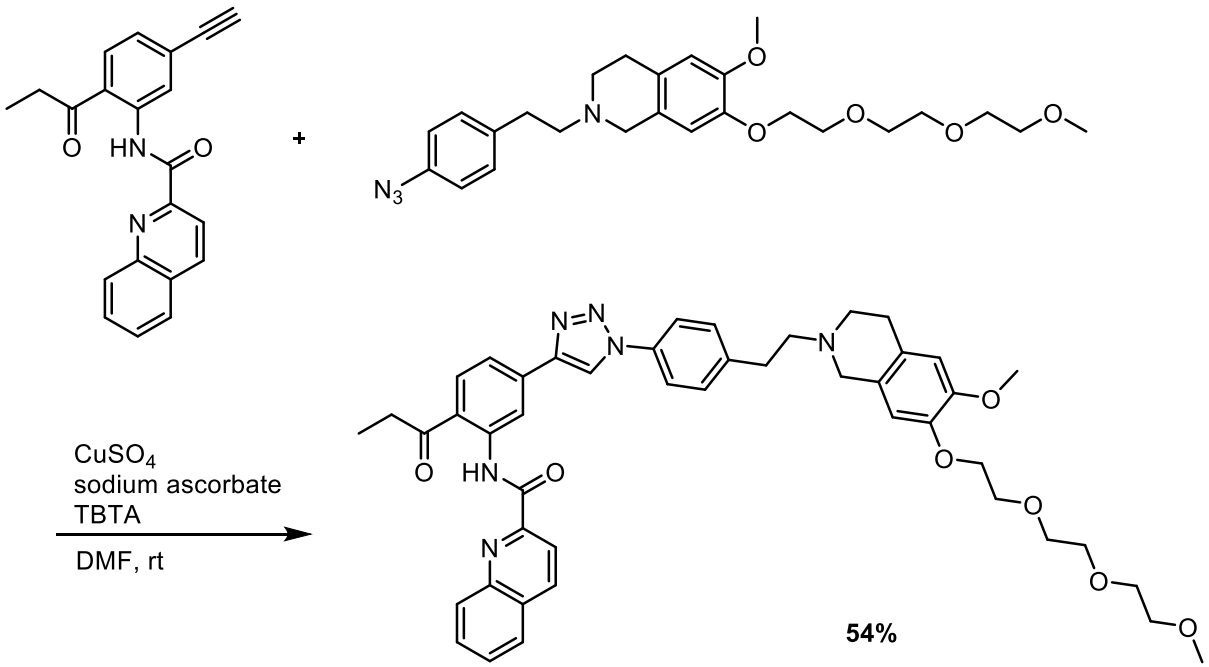

m.p.: 168 °C

RP-HPLC (220 nm): Purity 95%

^{1}H-NMR (600 MHz, $CDCl_3$): δ (ppm) = 1.34 (t, *J* = 7.2 Hz, 3H), 2.79-2.88 (m, 6H), 2.99 (t, *J* = 7.9 Hz, 2H), 3.14 (q, *J* = 7.2 Hz, 2H), 3.36 (s, 3H), 3.53-3.55 (m, 2H), 3.63-3.68 (m, 6H), 3.71-3.75 (m, 2H), 3.81 (s, 3H), 3.86 (t, *J* = 5.2 Hz, 2H), 4.14 (t, *J* = 5.2 Hz, 2H), 6.60 (s, 2H), 7.42 (d, *J* = 8.3 Hz, 2H), 7.63-7.66 (m, 1H), 7.74 (d, *J* = 8.4 Hz, 2H), 7.81-7.85 (m, 1H), 7.89 (d, *J* = 8.0 Hz, 1H), 7.98 (dd, *J* = 8.3 Hz, *J* = 1.6 Hz, 1H), 8.09 (d, *J* = 8.3 Hz, 1H), 8.32-8.36 (m, 2H), 8.41-8.44 (m, 2H), 9.44 (d, *J* = 1.6 Hz, 1H), 13.96 (s, 1H)

^{13}C-NMR (151 MHz, $CDCl_3$): δ (ppm) = 8.7, 28.6, 33.3, 33.5, 50.9, 55.5, 55.9, 59.0, 59.6, 68.7, 69.6, 70.5, 70.6, 70.7, 71.9, 111.9, 112.3, 117.6, 118.7, 119.1, 119.9, 120.5, 122.3, 126.3, 126.8, 127.5, 128.3, 129.3, 130.0, 130.2, 130.5, 131.6, 135.1, 135.9, 137.6, 140.7, 141.5, 146.5, 146.7, 147.1, 148.3, 150.0, 164.4, 203.9

HRMS (ESI): *m/z* $[M + H]^+$ calcd. for $C_{46}H_{51}N_6O_7^+$ 799.3814; found 799.3823

1. Jang, D.O., D.J. Park, and J. Kim, *A mild and efficient procedure for the preparation of acid chlorides from carboxylic acids.* Tetrahedron Letters, 1999. **40**(29): p. 5323-5326.
2. Zhou, N., et al., *Hyper-Crosslinkers Lead to Temperature- and pH-Responsive Polymeric Nanogels with Unusual Volume Change.* Angew Chem Int Ed Engl, 2017. **56**(10): p. 2623-2627.

3. Choi, J.Y., et al., *Rational development of 4-aminopyridyl-based inhibitors targeting Trypanosoma cruzi CYP51 as anti-chagas agents.* J Med Chem, 2013. **56**(19): p. 7651-68.
4. Adams, B., et al., *Stereochemistry of reactions of the inhibitor/substrates L- and D-beta-chloroalanine with beta-mercaptoethanol catalysed by L-aspartate aminotransferase and D-amino acid aminotransferase respectively.* Org Biomol Chem, 2005. **3**(18): p. 3357-64.
5. Li, Y.X., et al., *Synthesis of potent BCRP inhibitor - Ko143.* Tetrahedron Letters, 2008. **49**(9): p. 1480-1483.
6. Kawabata, E., et al., *Design and synthesis of zinc-selective chelators for extracellular applications.* J Am Chem Soc, 2005. **127**(3): p. 818-9.
7. Shendage, D.M., R. Frohlich, and G. Haufe, *Highly efficient stereoconservative amidation and deamidation of alpha-amino acids.* Org Lett, 2004. **6**(21): p. 3675-8.
8. Jiang, H., et al., *Anion-mediated phase transfer of zinc(II)-coordinated tyrosine derivatives.* Organic Letters, 2005. **7**(14): p. 3013-3016.
9. Takaoka, E., et al., *Catalytic asymmetric synthesis of arbutamine.* Heterocycles, 1997. **46**: p. 157-163.
10. Jiang, Z.Y. and Y.G. Wang, *A mild, efficient and selective deprotection of t-butyldimethylsilyl-protected phenols using cesium carbonate.* Tetrahedron Letters, 2003. **44**(19): p. 3859-3861.
11. Masjost, B., et al., *Structure-based design, synthesis, and in vitro evaluation of bisubstrate inhibitors for catechol O-methyltransferase (COMT).* Chemistry-a European Journal, 2000. **6**(6): p. 971-982.
12. Makhynya, Y., et al., *Synthesis of selectively C-13-labelled bilin compounds.* European Journal of Organic Chemistry, 2007(8): p. 1287-1293.
13. Wang, H.S., et al., *Synthesis and evaluation of tryprostatin B and demethoxyfumitremorgin C analogues.* Journal of Medicinal Chemistry, 2000. **43**(8): p. 1577-1585.
14. Chan, T.R., et al., *Polytriazoles as copper(I)-stabilizing ligands in catalysis.* Organic Letters, 2004. **6**(17): p. 2853-2855.